Analysis of multiple Coulomb scattering of muons in liquid hydrogen

PhD Thesis

by

Gavriil Chatzitheodoridis

Department of Physics, University of Strathclyde

School of Physics & Astronomy, University of Glasgow

2022

Supervisors:

Prof. Kevin Ronald

Prof. Paul Soler

Declaration

This thesis is the result of the author's original research. It has been composed by the author and has not been previously submitted for examination which has led to the award of a degree.

Signed: Gavriil Chatzitheodoridis

Date: 31 October 2022

Abstract

A comparison is made between experimental measurements of muons passing through the MICE (Muon Ionization Cooling Experiment) liquid-H_2 absorber, with a Geant4 (v9.6) Monte Carlo (MC) simulation. The aim was to assess if the accuracy of the multiple Coulomb scattering (MCS) simulation algorithm is consistent with data across two configurations; one with the vessel filled with liquid-H_2, and one with the empty vessel. MCS is one of two parallel processes in ionization cooling (IC), a novel beam cooling technique that can achieve significant emittance reduction within the short muon life-time. The analysis is motivated from previous experimental measurements indicating poor predictive performance of MCS of muons through liquid-H_2 using various models. In future muon accelerator facilities, ionization cooling channels will use the ionizing collisions during passage through a low-Z absorber to damp beam momentum while re-supplying longitudinal acceleration. MICE concluded data-taking in 2017 and has since demonstrated the performance of IC while has also gathered straight-track data specifically for measurements of MCS. In this thesis, data taken with three beam settings are analysed that delivered beam momenta in the range 143–250 MeV/c at the two absorber configurations. The resulting p-values, expressing the probability of identity between the simulated and measured plane-projected scattering angle distributions are found to be in the range 0.44–0.98, without meaningful differences between the two absorber configurations, indicating that Geant4 (v9.6) accurately predicts MCS of muons through liquid-H_2 in the analysed momentum range.

Contents

List of Figures

List of Tables

List of Tables

Chapter 1

Introduction

1.1 The research scope of muon beams

The objective of experimental particle physics is to provide measurements that challenge the predictions of the best available theoretical models and where necessary, to indicate new routes for theoretical development. High-energy muon accelerator experiments are expected to provide new evidence to guide this exploration. The standard model of particle physics (SM), has been characterized as the most successful theory in describing fundamental particles and three out of four involved interactions [1]. Although the gravitational interaction has not been integrated to the SM, it is described independently by the theory of general relativity. It is widely accepted however that the SM is not complete, beyond the omission of the gravitational interaction. This section briefly discusses the use of muon beams in existing and planned experiments that aim at expanding the current state of physics. Theories that go beyond the SM can be validated and further developed (or invalidated) by experimental measurements of rare processes that remain unobserved. This can be due to either the combination of rarity and limited detector resolution or simply because they manifest at higher energies.

A significant counter-argument to the completeness of the SM comes from

astrophysical observations, which show that the known 12 fermions, 4 bosons and their anti-particles, account only for 5% of the total mass implied by the observed gravitational forces [2]. The unknown remainder is inferred to not participate in the electromagnetic interaction, and is therefore transparent to light [3]. Another contradiction from the same field is the abundance of matter over anti-matter in the universe, although the SM does not foresee an asymmetry of that scale. This asymmetry could be a consequence of charge-parity (CP) violation of the electroweak force [4], which has been observed experimentally in exotic short-lived hadrons [5,6] and is incorporated into the SM by the Cabibbo-Kobayashi-Maskawa (CKM) matrix [7]. CP-conservation has also been excluded to the 3σ level for the most abundant lepton in the universe, the neutrino, by the T2K experiment [8]. This can be incorporated into the SM through the Pontecorvo-Maki-Nakagawa-Sakata (PMNS) matrix [9], however unambiguous confirmation and measurement of the violation rate is yet to be provided experimentally. Precise quantification requires long base-line neutrino oscillation experiments, for example from neutrino factories (NF) [10], facilities which require high-brightness muon beams to decay into intense, well-characterized neutrino beams.

The most probable channel of muon decay is $\mu^- \rightarrow \bar{\nu}_e \nu_\mu e^-$. Experiments are already utilising muon beams to search for charged lepton-flavour violation in rare muon decays. The Mu3e experiment at the Paul Scherrer Institut (PSI) aims to constrain the $\mu^+ \rightarrow e^+e^+e^-$ branching ratio to below 10^{-16} [11]. Another unobserved charged-lepton violating channel is the neutrino-less muon decay in the field of a nucleus, which will be investigated by the Mu2e experiment [12] at Fermilab and at the COMET [13] experiment at J-PARC. The most recent evidence against the SM in the lepton sector comes from the Muon g-2 experiment which measured the anomalous magnetic moment (α_μ) of the particle to an unprecedented precision, yielding a 3.3σ offset from the SM calculation. A non-zero value for α_μ is a result of interactions with virtual particles; the large offset indicates that there

are significantly more of these interactions than theorized [14]. The advantage of using muons instead of electrons for precise α_μ measurements is due to the particle's high mass.

New exotic and massive particles that are yet unaccounted by the SM can be discovered in high energy collisions. MICE forms part of a large and worldwide research effort to resolve the technical challenges involved in building a NF and a $\mu^+\mu^-$ circular collider [15]. The planned muon collider is expected to reach energies as high as 14 TeV. Muons are more suitable than electrons for such facilities once more due to their high mass, and therefore suppressed synchrotron radiation which can result to sizeable energy-efficiency enhancement in a circular lattice. Protons, which have been used extensively, are composite, and the collision energy is divided among the constituents. The muon collider initiative has determined that a 100 TeV proton collider will have similar discovery capabilities as a 14 TeV muon collider [16].

The challenge of accommodating muons in storage rings is due to the particle's short life-time – 2.2 μs at rest. Proton colliders like the LHC achieve high-brightness with methods that require time that is unavailable for muons. Significant acceleration can delay the muon decay by time-dilation through the Lorentz factor; however this still requires prior - or simultaneous - beam conditioning. Particles must be in dense bunches with predictable orbits that can be given impulse in the right direction through time-varying radio-frequency (RF) cavities.

Beam cooling is a term used in particle and accelerator physics to describe the gradual increase of the beam's density and parallelism through various methods. For muon beams, such methods will likely be intertwined with acceleration sections to prolong their life-time. Intermittent acceleration is an integral part of IC, which is discussed in section 1.2.4. MCS, the phenomenon analysed in this thesis, is a key component of IC and detailed designs of cooling cells for future accelerator facilities require precise predictive algorithms for this effect.

1.2 Charged particle beam cooling

Emittance (section 3.3) is the established figure of merit for a beam's quality, parallelism and focusability expressed as the volume occupied by the beam in phase-space dimensions i, p_i (with space-coordinates $i = x, y, z$). Similar to the MICE coordinate system, in this thesis $\widehat{y}$ is taken to point upward, with $\widehat{z}$ considered co-axial with the experimental axis (principle axis) and $\widehat{x} = \widehat{y} \times \widehat{z}$.

Emittance is therefore a metric that refers to both the angular spread and physical size of the beam, usually in units of $\pi \cdot \mathrm{mm} \cdot \mathrm{mrad}$. Accelerator facilities have a tolerable acceptance in terms of the maximum beam emittance they can accommodate; the upper limit of this acceptance sets the minimum physical size and the magnetic requirements of the beam transport elements. Particles outside this limit will have a high probability of being lost to the surrounding structure. Depending on the beam's nature, energy and density, this can result in erroneous signals in the detectors, heating and activation of the apparatus and in all cases efficiency loss.

Methodological advances in accelerator physics and a wider scope of particle physics becoming available inevitably led to energy-frontier accelerators increasing in length or circumference. Higher energies are reached by exposing the beam to localised, periodic accelerating fields, hence the issue of beam size and density becomes all the more substantive. The gradual increase in the size of a beam with non-zero emittance must also be counteracted. The long and complex accelerator lattices can also result in emittance exchange which also requires management. Furthermore, and quite fundamentally, the emittance limits the brightness of the beam; something particularly important for colliders.

Temperature (T) and emittance are interchangeable concepts in publications and books; a low-emittance beam is similarised to having a low temperature and a high-emittance beam to having high temperature. This is due to temperature

predating emittance as a conventional metric of a beam's momentum spread. The root-mean-square (rms) temperature due to the transverse momentum spread of a beam can be expressed by [17]

$$k_B T = \frac{m v_z^2}{2}\left(\left\langle\left(\frac{p_x}{p_z}\right)^2\right\rangle + \left\langle\left(\frac{p_y}{p_z}\right)^2\right\rangle\right), \tag{1.1}$$

with k_B the Boltzmann constant, v_z and p_z the component of velocity and momentum parallel to the experimental axis and p_x, p_y the transverse momentum components[1]. Temperature however does not contain information regarding the spatial extent of the beam.

The various methods used to control emittance reduce the extent of the spatial or momentum distributions by use of some damping force. The required time for any such method to achieve sufficiently low emittance is inevitably proportional to that damping force.

1.2.1 Radiative cooling

There are multiple operational synchrotrons that utilise GeV-scale electrons as light sources due to the high spectral brightness ($\mathrm{N_{ph}\,m^{-2}\,rad^{-2}\,bandwidth^{-1}}$) photon beam that can be extracted and exploited in imaging and spectroscopy. Higher particle energy facilities usually have multiple purposes, with one of them focussed on collisions between counter-propagating $\mathrm{e^-e^+}$ beams. The emittance reduction or preservation methods in these facilities have different requirements compared to hadron colliders or a muon collider. Electrons are cooled naturally to a degree, due to the damping effects of synchrotron radiation, emitted during acceleration, which also results in energy loss. By re-supplying sufficient z-acceleration, the emittance can be maintained to an equilibrium [18]. Cooling methods that rely on the beam's radiated power as a damping force are referred to as radiation cooling,

[1] Equation 1.1 is based on Newtonian kinematics and is merely illustrative of the relationship between phase space volume and a concept of temperature

and the cooling rate is proportional to the radiated power, given by [19] as

$$P_{SR} = \frac{dE}{dt} = \frac{1}{6\pi\epsilon_0}\frac{q^2a^2}{c^3}\gamma^4, \tag{1.2}$$

where q is the electric charge, a the acceleration, c the speed of light, γ the Lorentz factor and ϵ_0 the vacuum permittivity. To achieve increased beam cooling performance in higher energy synchrotrons, using PETRA-III [20] as an example, where the beam is accelerated to energies as high as 6 GeV, while the final beam emittance is $1.3{\times}0.01\,\mathrm{nm}\cdot\mathrm{mrad}$, damping wigglers [21] are used. An oscillatory motion is enforced by magnetic fields in the transverse direction, increasing the radiated power and hence the damping rate. Used as a dissipative force, synchrotron radiation emission can be efficient for light particles like the electron but as the γ^4 factor in equation 1.2 shows, the damping rate for a similar energy muon beam would be orders of magnitude less, when compared to an electron.

1.2.2 Electron cooling

Ion storage rings in CERN have mainly employed two different beam techniques to reduce emittance [22]; electron and stochastic cooling [23]. Electron cooling was proposed as a method to damp betatron oscillations in an ion storage ring by G. I. Budker [24]. The concept consists of a straight section of the storage ring (usually in an on-axis solenoid magnetic field) where the hot beam of ions is mixed with an injected cold beam of electrons that are, shortly after, extracted (Figure 1.1).

For ion beams with atomic number Z, the damping rate of electron cooling (without $\vec{B}$-field) is approximated by [25] in dimensions of Joules per second^2 as

$$\frac{dE}{dt} = \frac{Z^2e^4n_e}{4\pi\epsilon_0^2 m_e v_{rel}}\ln\left(\frac{b_{max}}{b_{min}}\right), \tag{1.3}$$

with n_e, e and m_e the electron beam density, electron charge and mass. $b_{min/max}$

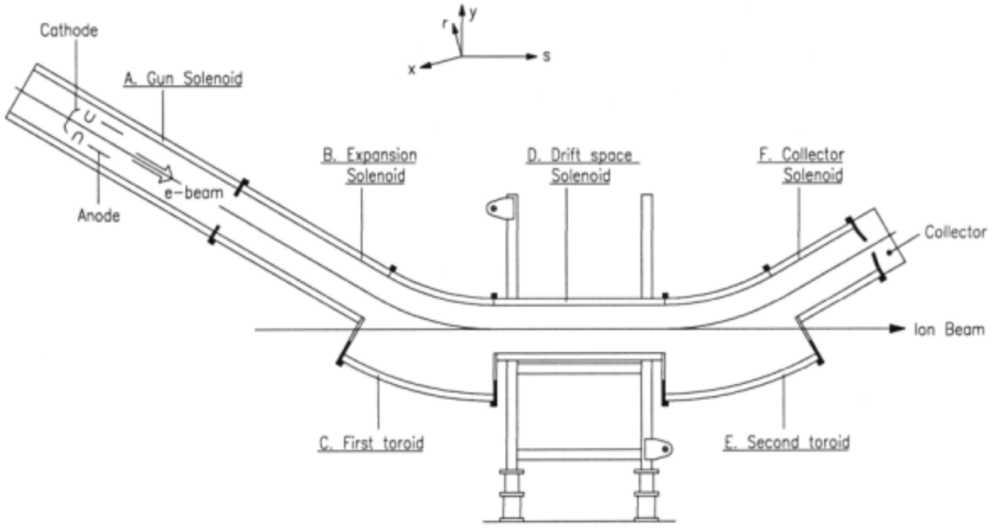

Figure 1.1: Electron cooling layout at LEIR, CERN from [24].

are the minimum and maximum impact parameters that are further discussed in section 3.5 and v_{rel} the relative velocity of the "hot" and "cold" beams[2].

The method is suitable for ions, but it requires long interaction times with the electron beam compared to the muon life-time.

1.2.3 Stochastic Cooling

Stochastic cooling was proposed by S. van der Meer, who received a Nobel prize (1984) for his contribution at CERN due to the importance of the stochastic cooling technique, used to cool colliding beams of protons and antiprotons that that lead to the discovery of the W and Z bosons [26]. A stochastic cooling system consists of two main components: a sensor, or a "pickup" that measures transverse spatial deviation of the beam in segments at a point of the orbit around a storage ring and a "kicker" magnet that receives the amplified signal and applies a correctional impulse to each segment sample (figure 1.2). The strength of the correctional kick must be dependent on the error of the sensor signal to result to

[2]Converted to SI from CGS units used in [25]

the correction being productive for more particles than those it over- or under-corrected. Assuming exponential damping $\frac{p_i(t)}{p_i(t_0)} = \exp(-(t-t_0)/\tau)$ of a transverse momentum component $p_{i=x,y}$ a minimum half-life of $\tau_{1/2} = \tau \ln 2$, where $\tau = 1/\lambda_{max}$ can be calculated. An approximation to λ_{max} is provided by [27] as equation 1.4. The mixing factor (M) is inversely proportional to the re-randomization rate of the beam. The beam sample that the pickup senses must be completely mixed with the rest of the beam between revolutions, otherwise the mixing factor rises above 1 and reduces the damping rate. The value of λ_{max} is found to be:

$$\lambda_{max} = \frac{2W}{N} \frac{1}{M+U}. \tag{1.4}$$

In the above equation, W is the spectral bandwidth of the signal, N is the number of particles, and U is the noise to signal ratio.

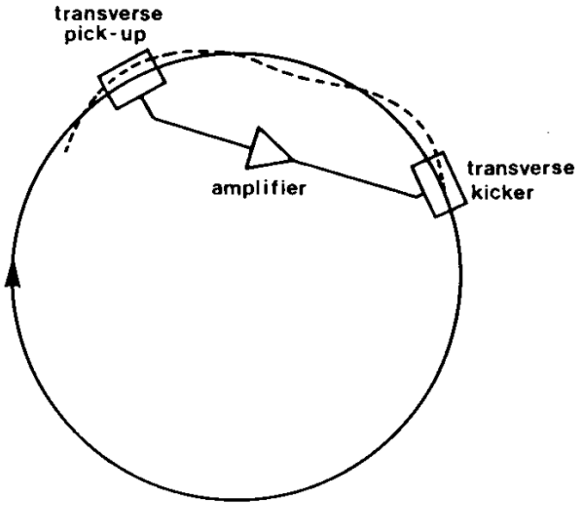

Figure 1.2: A simple sketch of a stochastic cooling system in a storage ring as illustrated by Simon van der Meer in the 1984 Nobel lecture [26].

1.2.4 Ionization Cooling

A beam cooling technique for charged particles that dissipates beam momentum when passing through a low atomic number (Z), energy absorbent material was first published in [28] and later proposed for application in muon beams [29] as ionization cooling (IC). IC relies on momentum loss due to soft ionizing collisions when a focused beam passes through matter, followed by acceleration. The longitudinal momentum lost to collisional ionization can be re-supplied, while the transverse component is damped in cycles until an equilibrium emittance is reached.

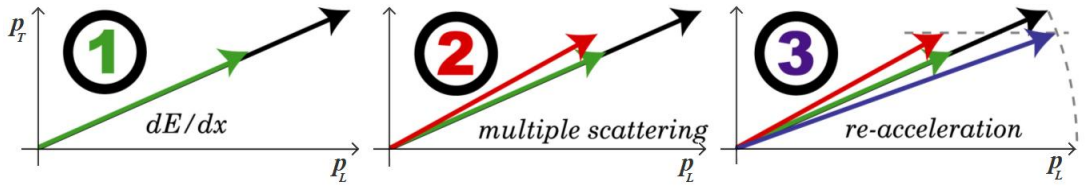

Figure 1.3: Ionization cooling process: 1) The beam's momentum magnitude is reduced through ionizing collisions accompanied by 2) MCS; a "heating" effect that must be controlled. 3) Acceleration re-supplies only the longitudinal momentum component.

The expected performance can be calculated with equation 1.5, which is derived in [29]. It expresses the muon beam's transverse normalised emittance $\varepsilon_{\perp n}$ (discussed in section 3.3) as a function of path length (z) through an absorber material with radiation length X_0:

$$\frac{d\varepsilon_{\perp n}}{dz} = -\frac{\varepsilon_{\perp n}}{\beta^2 E_\mu}\left\langle \frac{dE_\mu}{dz} \right\rangle + \frac{\beta_\perp (13.6\text{MeV/c})^2}{2m_\mu \beta^3 E_\mu X_0}, \tag{1.5}$$

where β, m_μ, E_μ are the fractional speed (v/c) mass and total muon energy. The transverse betatron function $\beta_\perp$ is proportional to the beam's spatial extent in the transverse direction (more in section 3.3).

The first RHS term expresses $\varepsilon_{\perp n}$ change due to energy loss (to ionisation) and the second expresses emittance increase due to MCS. The damping of transverse components of momentum can be increased by locally exchanging momentum

from the longitudinal component to the transverse during the interaction with the absorber using focussing beam optics. This is expressed through $\beta_\perp$, which is minimised at a focus point. The advantage of a low-Z material is seen in the relationship of the radiation length [30] with the atomic number (Z) and atomic mass number (A) in the equation below:

$$X_0 = 716.4 \mathrm{gcm}^{-2} \frac{A}{Z(Z+1)\ln\frac{287}{Z}}. \tag{1.6}$$

Radiation length is a material property that expresses the amount of matter traversed in a material before a high-energy electron loses all but 1/e of its energy by bremsstrahlung, and 7/9 of the mean free path for pair production by a photon.

Although liquid-H_2 is in theory the best performing absorber option for IC, there are many technical challenges in incorporating the material in a cooling cell design due to its volatile nature. In addition, MICE collected straight-track data (without magnetic-fields) for the absorber materials xenon, liquid-H_2 and lithium-hydride (LiH) that can be found reconstructed in [31]. Their radiation lengths are included in table 4.5.

In a repeatable IC cooling cell (damping-acceleration cycles), the RMS of the transverse momentum distribution of the beam decreases until equilibrium emittance (equation 1.7) is reached, marking the point where the heating term equals the cooling term. The absorber material properties sets this equilibrium emittance, as seen in:

$$\varepsilon_\perp = \frac{\beta_\perp (13.6\,\mathrm{MeV})^2}{2\beta m_\mu X_0} \left\langle \frac{dE_\mu}{dz} \right\rangle^{-1}. \tag{1.7}$$

To enable detailed design of IC cooling cells, validated predictions of the two counter-acting phenomena are required. Energy-loss through ionization is a well-understood phenomenon, and is predicted correctly by simulations [32]. Experimental data of MCS of muons in low-Z materials has been shown to differ from

simulations with older versions of Geant4. This is covered in section 1.3.

The spread of the longitudinal momentum component however is not treated by IC as described above. To achieve longitudinal cooling, schemes using emittance exchange have been considered as illustrated in figure 1.4.

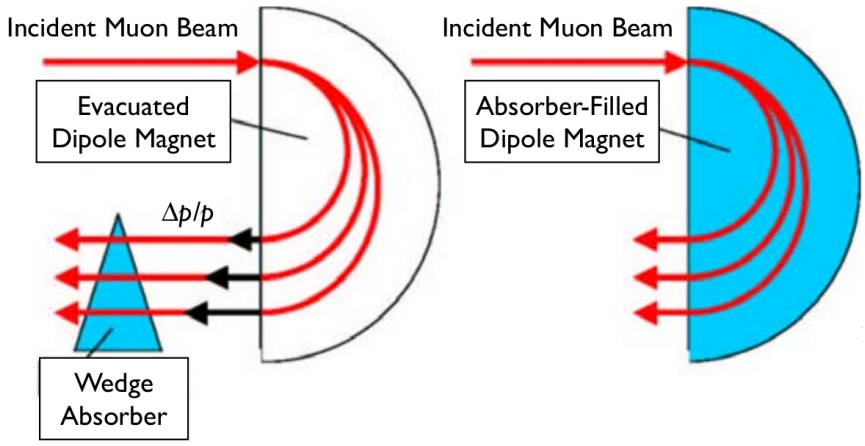

Figure 1.4: A particle ensemble with a distribution of longitudinal momentum will follow different routes through a dipole magnet. This can be exploited for 6D cooling to correlate $\Delta p_{\parallel}$ to path-length in concepts like the two illustrated [33]. On the right, the absorber material is integrated into the dipole and on the left a wedge shaped absorber is placed after the dipole.

In IC with a wedge-shaped absorber, the longitudinal momentum spread of the particles is reduced through variable path-length through the absorber material forced by a dipole magnet. In that way slower particles cross less material and therefore lose less energy, while higher-energy particles are directed to a longer section of the absorber, increasing the energy loss at the expense of increasing transverse emittance [34].

1.3 Results of muon scattering from MuScat

Due to the growing interest for muons in high energy physics and the prospect of using IC to shrink the beam's phase-space, the MuScat collaboration performed a measurement of MCS with $172 \pm 2\,\mathrm{MeV/c}$ muons though various materials [35],

including liquid-H_2 and compared the results with two versions of the Molière scattering model [36], the Energy Loss Multiple Scattering (ELMS) model [37] and a Geant4 (v7.0p1) simulation. The muon beam was sourced from the M20 TRIUMF beamline, providing a 500 MeV (kinetic energy) proton beam which collided with a graphite target, creating charged pions that decayed to muons.

The experimental setup for MCS measurements was different from MICE; it consisted of two collimators separated by a ∼1 m drift space, with a ∼2 mm vertical slit in each collimator. This allowed only for a narrow, well-defined muon beam (in one plane) to pass through, hence avoiding an upstream measurement. After the collimator system, a choice of two vessels provided either 159 mm or 109 mm path-length through liquid-H_2. After a drift-space, a scintillating-fibre tracker was used to measure the spatial distribution of the beam. The angular deflection was deduced through the correlation with the spatial distribution. The apparatus also included a time-of-flight measurement system and a calorimeter to measure momentum and separate muons, pions and electrons. Measurements were also taken without the liquid-H_2 which allowed for the deconvolution (unfolding) of the liquid-H_2 effect to be extracted from the cumulative effect of scattering through other material and compared to the models. The deconvolution process is explained in detail in section 7.2 of the publication. The MuScat results are shown in figure 1.5 in terms of the y-axis (vertical) plane-projected scattering angle.

The measurement shows a progressive overestimation of scattering above 0.03 rad by the Geant4 simulation. The original Molière model (Z^2) and the ELMS model perform similarly up to 0.07 rad and diverge at larger angles. While the Molière model as modified by Bethe, notably with the Z-dependence of the scatterer (originally Z^2) replaced by $Z(Z+1)$ overestimates the number of mid-range scattering events. It can therefore be stated that none of the models accurately predict the measured distribution.

Although liquid-H_2 is not an element commonly found in transport elements,

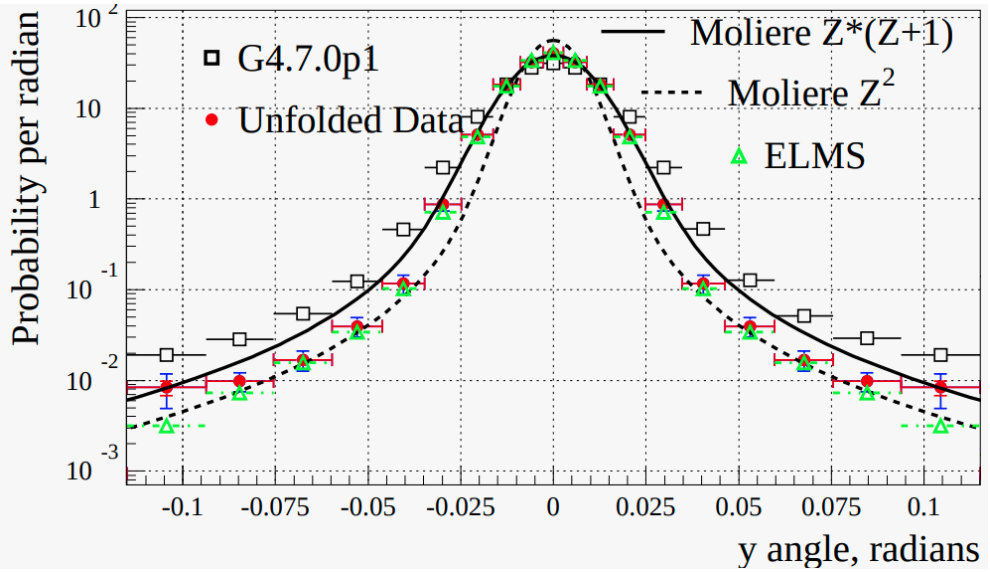

Figure 1.5: The MuScat measurement of MCS of muons through liquid-H_2 as published in [35]. The plane-projected (vertical direction) scattering angle distribution compared with the two versions of the Molière model, the ELMS model and Geant4 (v7.0p1)

given that the MuScat results are valid they can be interpreted in at least two ways; the performance of MCS models declines with reducing atomic number of target elements, or this is a problem specific to liquid-H_2. The performance of Geant4 is of interest to this study as it is the most common simulation package used for detailed lattice design in accelerator physics. The implication of this divergence could be an underestimation of the performance of ionization cooling which would lead to mismatches with the following optics that would progress with each cooling cycle.

It is therefore important to complete measurements of MCS of muons in liquid-H_2 in a wider momentum range, to compare to more recent versions of Geant4, in order to validate the MCS models used by Geant4.

Chapter 2

The Muon Ionization Cooling Experiment

The MICE collaboration submitted the proposal for the first experimental demonstration and quantification of the important parameters of IC in 2003 [38]. The experiment was conducted at the Rutherford Appleton Laboratory (RAL) in Oxfordshire, UK; utilising the ISIS [39] proton beam to produce pions through the process of spallation. The first MICE calibration data were acquired in 2008 and the final set of data was gathered in 2017, when decommissioning began.

Initially MICE was designed to be a staged experiment (figure 2.1 that would gather data during all steps for beam characterization [40] and detector calibration, leading up to a complete cooling cell with 3 absorber modules and 8 normal conducting 201 MHz RF-cavities to test IC with re-acceleration. The first step would focus on beam characterization using the two time-of-flight detectors (sub-section 2.1.4), the two Cherenkov threshold counters (sub-section 2.1.7) and the KL-calorimeter 2.1.8. Step-II would see the inclusion of the diffuser, which modifies the incoming beam emittance and a high-precision tracker-spectrometer module (sub-section 2.1.5) for detector calibration and emittance measurement. In Step-III the second tracker and the LiH absorber would be included, to be replaced in

step-IV by the liquid-H_2 absorber module, along with the addition of the focus coils. A second liquid-H_2 absorber module would be included in Step-V and 4 accelerating cavities, allowing for the complete IC cooling process to be tested. Step-VI would be able to characterize the process of IC at a scale similar to a future muon collider cooling cell, with acceleration that would fully restore the energy lost to the absorbers. Although complete realisation of these steps was not achieved, the experiment concluded in 2017, after gathering sufficient data to observe significant transverse beam amplitude distribution reduction, a particle-by-particle metric of emittance, and phase-space density increase [41] using liquid-H_2 and LiH. These results are discussed in section 2.3. The instrumentation used for the MCS measurement of this thesis and the beam cooling measurements is discussed in in the following section.

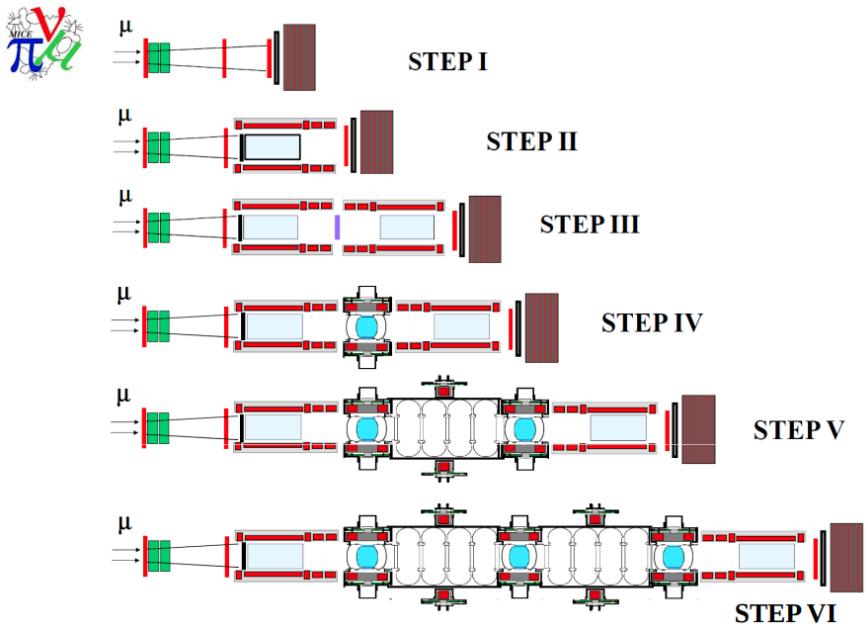

Figure 2.1: The initial step-wise development of MICE. Figure from [39].

2.1 The MICE apparatus

2.1.1 Beamline

The ISIS proton source produces $\sim 50\,\mathrm{mA}$ of H^- ions with $0.9\,\pi \cdot \mathrm{mm} \cdot \mathrm{rad}$ normalised emittance from a Penning ion source, which are bunched and accelerated by Radio Frequency Quadrupoles (RFQ) before reaching a LINAC and a $163\,\mathrm{m}$ circumference synchrotron which increases the kinetic energy to $\sim 800\,\mathrm{MeV}$ in a $200\,\mu\mathrm{A}$ beam.

MICE operated on a particle-by-particle measurement basis to achieve the required precision of measurement of MCS and emittance evolution. The collisions with the MICE titanium target occurred over about $1\,\mathrm{ms}$ at 0.8–$1\,\mathrm{Hz}$ frequency towards the end of the ISIS acceleration cycle (using only one in 50 of the ISIS cycles). One dip of the target is referred to as one "spill". A relatively low number of particles would result in each spill such that no more than one particle would be typically present in any of the MICE detectors within the measurement and recovery cycle of the detectors. The rate of double hits was adequately low that it was pragmatic to simply discard any events where ambiguity arose in the interpretation of the detector output due to double hit events. The beamline geometry is illustrated in figure 2.2.

The proton-proton collisions produced pions which were partly captured $3\,\mathrm{m}$ downstream by the first of the three quadrupole-triplet sets (Q_{123}) configured in a focus-defocus-focus setting. At $2.2\,\mathrm{m}$ from Q_3, the beam trajectory then entered one of the two dipole magnets (D_1) which selected pions of a certain momentum-range and steered them into the vacuum pipe entrance - $1.6\,\mathrm{m}$ downstream - that was placed in the decay solenoid (DS). The DS had a bore diameter of 12 cm and a length of $5.1\,\mathrm{m}$ through which a solenoidal magnetic field contained the particles, which aimed at increasing the number of muons that reached the MICE cooling channel by extending the pion trajectories to become helical. At the end of the

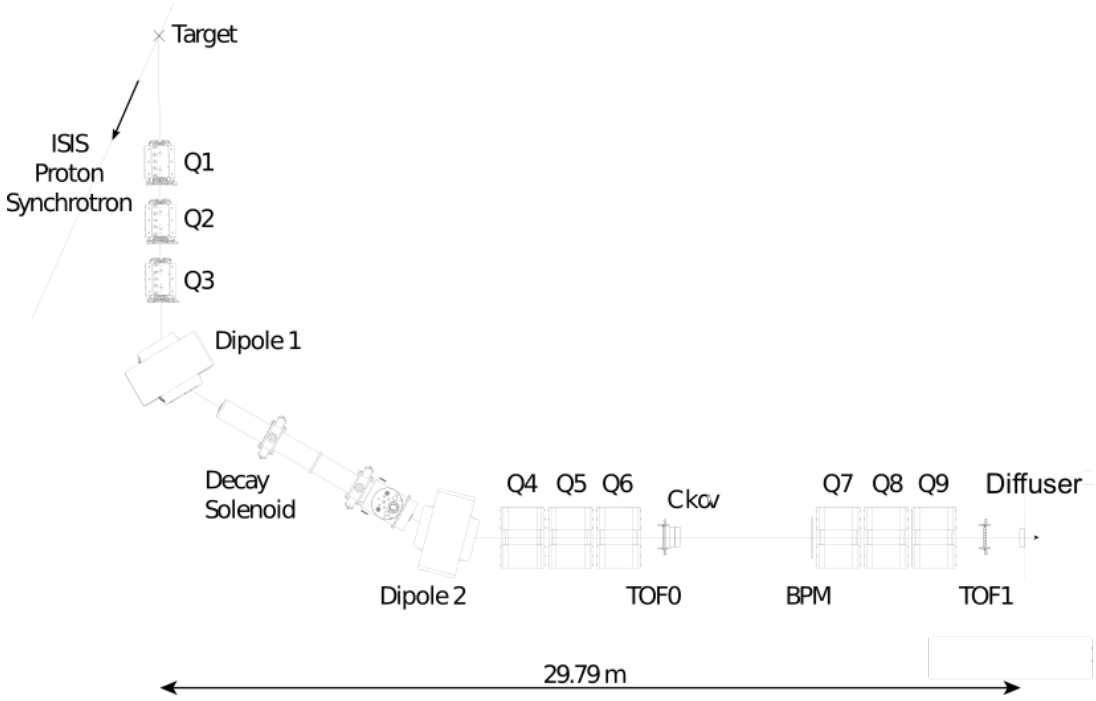

Figure 2.2: The MICE beamline on ISIS schematic from the MICE web-page [42]. Left-right: east-west.

DS, a second dipole magnet (D_2) steered either backward or forward going muons (with respect to the pion velocity) towards MICE. The selected beam drifted for 0.84 m from D_2 before passing through the Q_{456}-triplet, the first TOF hodoscope (TOF0), followed immediately after by the threshold Cherenkov counters. Finally 5.3 m from Q_6, a quadrupole triplet (Q_{789}) contained the beam in the path towards the second time-of-flight hodoscope (TOF1).

The interplay between the fields of D_1 and D_2 determined the composition of the beam. Two beam-modes were commonly used: the muonic-beam and the pionic-beam. In the first mode, backward muons (with respect to the pion rest frame) were selected. This mode favoured purity (>95% muons) but generally directed less particles to MICE. The pionic-beam mode directed a mixed beam at a high particle rate. The three sets of quadrupole triplets had an aperture radius of 10 cm and the dipoles a rectangular aperture of 50×15 cm (w×h).

The MICE target intercepted the proton beam on the north-west quadrant of the ISIS synchrotron. This interception point was used as an origin point to define a beam path through which the two dipole magnets would lead to the cooling channel aligned with the south wall of the north-west building of the ISIS Pulsed Neutron and Muon Source. The position and orientation of the beamline and cooling channel elements were surveyed multiple times with laser coordinate measurement systems (surveys) during the development and active stages of the experiment. The particle reference path turned north from the synchrotron by 30° where the spallation products were captured by Q_{123}, The first bending magnet steered the beam 60° west, and the second magnet another 29.6°.

2.1.2 Cooling channel

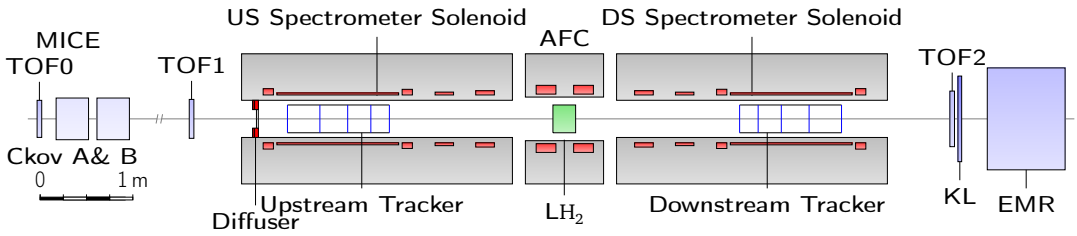

Figure 2.3: Schematic of the MICE step-IV cooling channel

The MICE cooling channel configuration (figure 2.3) that was used to gather the data for this analysis comprised of the Absorber Focus Coil (AFC)- which housed the absorber vessel. It was situated between two He filled spectrometer modules; upstream (US) and downstream (DS), each containing of a scintillating-fibre particle tracker as shown in figure 2.5 enclosed in a 4 T super-conducting solenoid magnet. The trackers were also both enclosed by aluminium windows to contain the helium gas that was used to displace the air, and reduce MCS. The tracker recorded the x-y positions of individual particles at five different scintillating-fibre (scintillating-fibre) stations with an active diameter of 30 cm. The solenoid magnets around the trackers and the focussing magnets of the AFC

were disabled during the gathering of the data analysed here. Two threshold Cherenkov counters, a pre-shower calorimeter (KL) and an Electron Muon ranger (EMR) are also situated as seen in figure 2.3 for particle identification purposes. Before the first (US) tracker a variable thickness diffuser increases the beam's emittance but for the experimental runs of interest to this analysis the diffusing material was retracted. Data from the three TOF hodoscopes are used to determine particle velocities, with TOF1 and TOF2 placed equidistantly from the AFC.

2.1.3 Particle tracking methods

Excluding the Cherenkov threshold counters, the particle detectors of MICE rely on the process of scintillation for signal generation. Scintillation is luminescence produced by ionizing events such as the passage of charged particles.

2.1.4 Time-of-flight (TOF) detectors

The three TOF detectors of MICE share a common architecture. The basis is the 2.54 cm thick fast scintillator slabs coupled with polymethyl-methacrylate light-guides that lead to photomultipliers on both ends. TOF0 has an active region of 40×40 cm with two planes of ten 4×40×2.54 cm (x-y-z) BC-420 slabs rotated 90° with respect to each other, while TOF1 consists of two planes of seven 6×42×2.54 cm slabs rotated at right angles. TOF2 (Figure 2.4) covers an area of 60×60 cm with ten slabs in each plane. For TOF1 and TOF2 the BC-404 scintillator material has been used. Each plane provides a time resolution of better than 70 ps [43, 44].

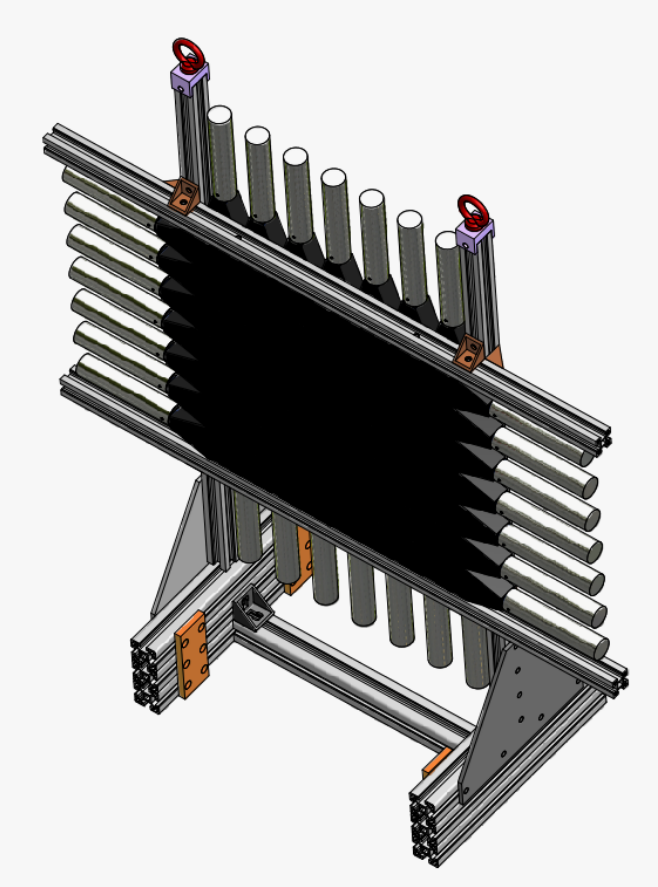

Figure 2.4: Schematic of the TOF1 hodoscope with visible slab arrangement from [45]. The hodoscope was positioned so that, together with TOF2 the momentum at the absorber centre can be measured.

2.1.5 Scintillating-fibre trackers

The two scintillating-fibre trackers provided the trace-space data used to measure MCS. They were placed upstream and downstream of the absorber vessel, each within the bore of a solenoid magnet. The fundamental component of this tracking device is the $350\,\mu\mathrm{m}$ diameter clear polystyrene fibre, which is manufactured to provide both scintillation and light guidance [46]. The tracker's active volume is defined by five stations (figure 2.5).

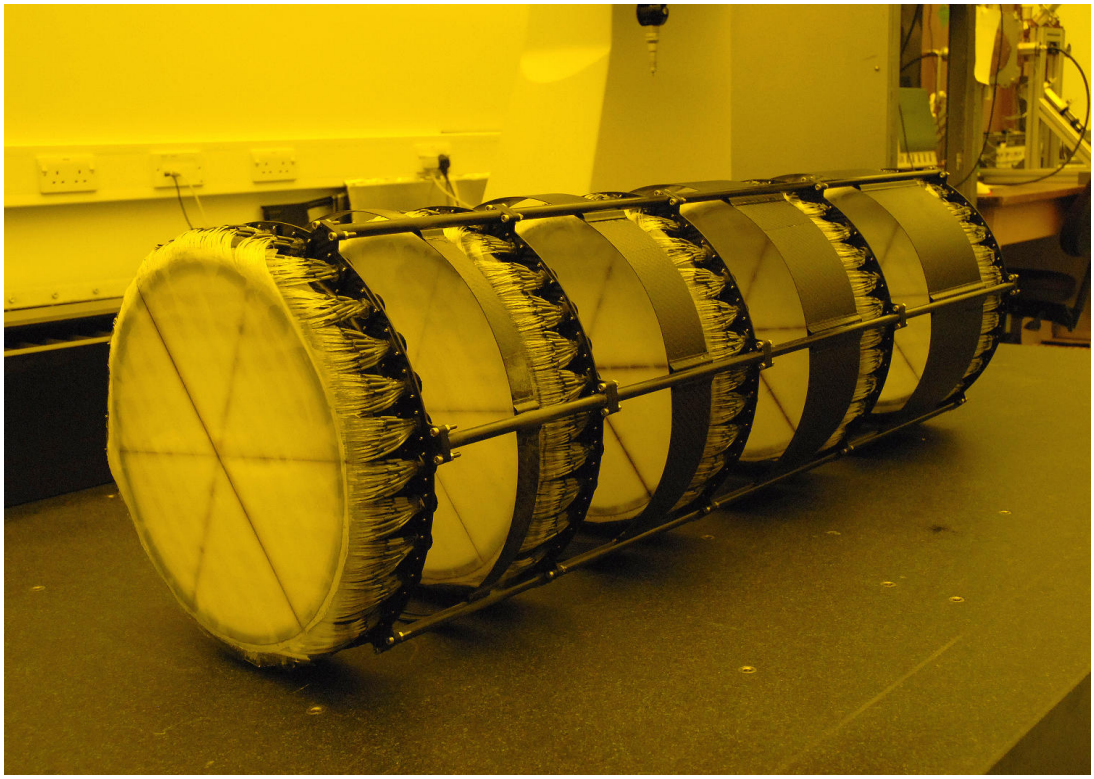

Figure 2.5: Photograph of one of one of the two scintillating-fibre trackers used in MICE, taken from the MICE web-page [42].

Each of the five stations consists of a triplet of doublet layers of fibre. Each of the triplets (labelled u-v-w in figure 2.6, b) is rotated at 120° to each other (Figure 2.6, a), providing a coupled x-y measurement of the passing particles. The amount of material in the beam path, especially those with short radiation lengths like polystyrene $\sim 43.8\,\mathrm{g}\cdot\mathrm{cm}^{-2}$, interfere with the beam and increase the beam

size through MCS, while enough material must be present to provide significant probability of producing and capturing light signals. The arrangement of the fibre layers (figure 2.6, b) was designed to minimise the associated dispersion. Each doublet was backed by a sheet of mylar plastic that formed the foundation on which the fibre-planes were arranged. The fibres were bundled together (in bunches of seven) and led to a single visible light photon counter (VLPC), corresponding to a single channel. There are 213 channels for each v and w plane, and 212 for each u plane.

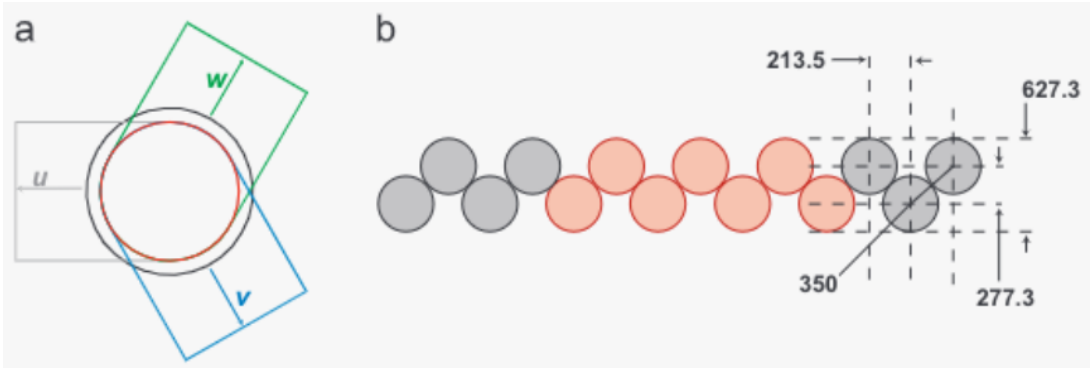

Figure 2.6: a) The outer black circle denotes the spectrometer bore limit and the inner red circle the active tracking diameter $\sim 30\text{cm}$. The three planes noted u, v and w show the direction of each of the three fibre doublets, with the u plane orientated parallel with the ground, aligning with the x experimental axis. b) The arrangement of a doublet layer. 7 fibres (colored red) merged to a single $1.05\,\text{mm}$ diameter light-guide. The units denoted are μm. Schematic from [46].

2.1.6 AFC - Absorber Focus Coil

The AFC was positioned equidistantly from the two spectrometer solenoids as seen in figure 2.3. The module was designed to house the absorber materials and provide the low-beta area using focussing magnets. Among the materials tested by MICE was a solid LiH disk and liquid-H_2. Maintaining the latter in a stable liquid state throughout the duration of the tests while satisfying all the required safety measures was a challenging and complicated engineering task. The material

is explosive when exposed to air and a temperature below 20 K at 1.0013 bar must be maintained. Another requirement that had to be taken into consideration was to minimise the number of radiation lengths of structural material in the beam path, which would lead to unwanted emittance increase. This section covers the features of the design adopted by MICE that is relevant to this study, and the state of the liquid-H_2 absorber while collecting the data analysed in study. A more detailed description is in [47].

The vessel used to hold liquid-H_2 (figure 2.7) was an aluminium cylinder aligned with the experimental axis when in-place, enclosed by two dome-shaped end windows. The inner radius of the cylinder was 150 mm and had a length of 230 mm, designed to hold 22 l of liquid-H_2. The total on-axis path through liquid-H_2 was 350 mm due to the aluminium windows extruding from the cylinder ends. The windows were machined to have a minimum on-axis thickness of 180 μm; occurring at the centre of the dome, and gradually increasing outwards to 1.5 mm, as seen in figure 2.8. Two vacuum windows of similar design but with a central thickness of 210 μm enclosed the vessel in vacuum as a safety measure in case of leak of the primary container (seen in figure 2.9). The window structure is discussed in detail in section 3.4, where the distributions of individual muon path length is calculated to account for energy loss. The focus coils are placed upstream and downstream of the absorber centre and are 210 mm in length. Both are immersed in liquid helium, which through heat exchange using cryocoolers are cooled down to 4.2 K to produce an on-axis magnetic field of ±2 T in solenoid and flip-mode.

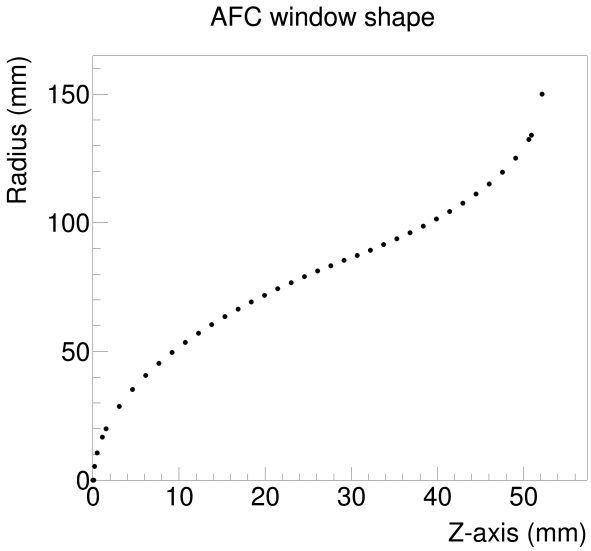

Figure 2.7: Dome radius as a function of Z for the aluminium windows of the AFC. The point z=0 is the centre of the window aligned with the beam axis.

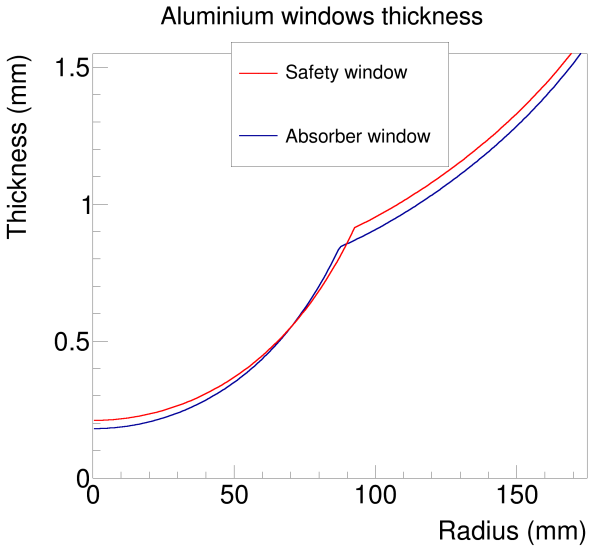

Figure 2.8: Absorber and vacuum window thickness against radius.

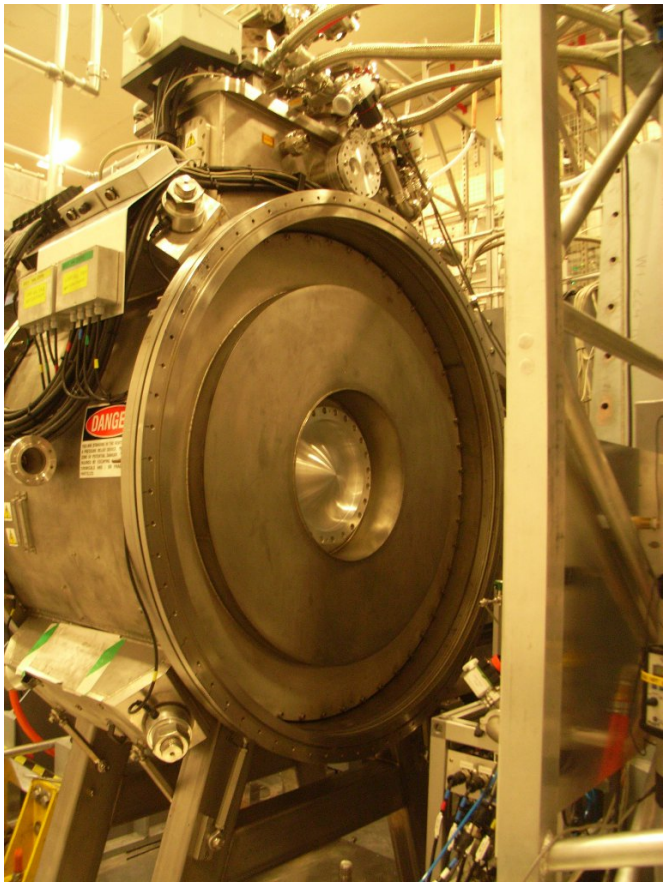

Figure 2.9: The AFC module with one of the safety windows visible. Photograph from the MICE web-page [42].

2.1.7 Cherenkov

Two threshold Cherenkov counters (CkovA, CkovB) [48] are placed just after the first TOF counter as part of the particle identification (PID) system. Both detectors are made of high-density aerogel with refractive indexes $n_A = 1.069 \pm 0.003$ and $n_B = 1.112 \pm 0.004$. Passage of charged particles with a velocity greater than the phase velocity of light in the material ($\beta_A = 0.93, \beta_B = 0.9$) produces Cherenkov radiation. Since pions, muons, protons and electrons have different mass, it allows the experiment to distinguish particles with the same momentum by the amount of Cherenkov radiation emitted (the lighter the particle, the more Cherenkov radiation is emitted).

2.1.8 KL-calorimeter

Initially the calorimeter [49] was designed for the DAΦNE experiment [50]; a 0.5 GeV kinetic energy electron-position collider that studied CP-violation in neutral kaon decays. For the purposes of MICE, it was modified to be used as a pre-shower detector for the EMR by reducing the lead volume and was renamed KLOE-light. The KL was positioned immediately downstream of the TOF2 detector and 0.7 m upstream of the EMR.

Calorimeters usually combine two functions in their design, material properties that cause particles to produce EM or hadronic-showers, depending on their nature, and detection of the deposited energy. Showers involve cascades of particles with complexity and length dependent on the available energy of interactions with the atomic nuclei or orbital electrons. Radiation produced by passing charged particles cause $\gamma \rightarrow e^- e^+$ pair-production, giving ample chances for signal generation along the cascade. As the KL was installed in MICE, it had a 4 cm on-axis path length and an area of $93 \times 93\,\mathrm{cm}^2$ of 2:1 lead to scintillating-fibre to lead volume. The lead stopped most electrons that reached it, and the fibres provided an estimate

of the deposited energy at a $70\,\mathrm{ps}/\sqrt{\mathrm{E}}$ time resolution read out by 42 channels.

2.1.9 The Electron Muon Ranger

The Electron Muon ranger (EMR) [51] was a 3D active tracking calorimeter and the final detector of the MICE lattice. Most particles that reached the EMR were stopped by 85 cm of scintillator and optical fibre, providing a measurement of the penetration range that could be used to estimate momentum. The EMRs $0.9\,\mathrm{m}^3$ volume Was occupied by triangular polystyrene bars, arranged to minimise the passive volume. Through each bar, a wavelength-shifting fibre lead captured light to 48 multiple-anode PMT's providing 2832 separate channels for readout. Due to the density of activated scintillators and the high-spatial resolution, the EMR could provide information on the decay vertex of individual particles that were used as discriminators for particle identification between particle species, in addition to momentum measurements from the stopping range.

2.1.10 Track reconstruction

Reconstruction of tracks in the two scintillating-fibre trackers was performed by MAUS (MICE Analysis User Software) [52], with detailed description of the reconstruction software in [53]. The lowest-level concept of the reconstruction was the digit: a count of photo-electrons coming from a single channel (e.g. a group of 7 fibres) that surpassed the noise-limit. In the case of simulation, digit formation was based on the energy lost by the interacting particle through the detector material and scaled by the detector's efficiency in converting this energy to voltage in the visible-light photo-counters (VLPC's). Real and simulated digits are treated in the same way by the reconstruction software. Each element (planes, stations) of the tracker initially has a local coordinate system which is transformed to the coordinate system of the trackers as the reconstruction progresses. Initially,

signal clusters of 1 or 2 proximal digits per plane are considered for space-point reconstruction. The reconstruction algorithm then searches for proximal triplet clusters (one in each 120-degree rotated plane) and then duplet signals. Due to the architecture, a duplet signal is enough to determine the x-y position of a signal-generating particle. If space-points are formed in more than one station then a straight track is fitted through a least-squares method which is then optimised through a Kalman filter [54].

2.2 MAUS and Geant4

MAUS (MICE Analysis user Software) [55] is the software that covered the computational requirements of the experiment from design to analysis. It is a collection of routines created by the collaboration and linked together with third-party packages. It served as the interface to MICE during the active data-taking periods for monitoring and diagnostics, but also contains the reconstruction routines that produce higher-level objects (e.g. particle tracks) from VLPC signals (section 2.1.10). Moreover, bound together with Geant4 (v9.6) [56] it also handles the simulation of the beam's passage through the defined geometry and the detector response. Routines that require high-performance are written in C++, and the majority of the user interaction is done through Python. Parallel-processing of data is done though the Map-Reduce programming model [57].

The input to MAUS is segmented in spills, corresponding to dips of the MICE target [58] in the ISIS proton beam. These can be real detector signals or beam instances for simulation. The latter can be human-readable text files in the JSON [59] format, or ROOT files [60] that contain a particle-by-particle beam definition. To generate those, the beam phase-space parameters can be sampled from common distributions or from an ellipse defined by the Twiss parameters (discussed in section 3.3) or through more simplistic methods e.g. pencil beam.

Alternatively, simulated spills can be generated by G4BeamLine [61], which simulates pion production in the MICE target and beam propagation in the MICE beamline up to 1 m from D_2.

The data-flow is seen in the figure 2.10 schematic. In the case of the simulation, to generate signals in the trackers MAUS uses the energy deposited by the beam in the active detector material provided by Geant4 and the modelled detector efficiency. Geant4 uses the detailed descriptions of physical volumes defined in the geometry description (Geometry Description Markup Language - GDML [62] format) to probabilistically induce perturbations to each particle's physical parameters (e.g. angular displacement, energy deposition) from probability distributions calculated using physics models. Energy loss through ionization is simulated by an implementation of the Bethe formula (section 3.4). The available models for MCS calculations in Geant4 are briefly discussed in section 3.6.1. The number of photoelectrons (NPE), simulated or real are digitized (section 2.1.10) and treated in an identical way. Reconstruction mappers then proceed detector-by-detector to associate channels with geometry positions and produce higher-level objects (e.g. scintillating-fibre tracks). The geometry of the MICE cooling channel is stored in GDML format, that can be directly used by Geant4. In the case of simulation, available particle information is also recorded in virtual planes. The information recorded in virtual planes (referred to as MC Truth) are accurate particle parameters, like position, direction vectors, energy and particle identity. The reducer then generates data-visualisations for the entire data-set, and finally, the results are written to disk or sent through the network by the output module.

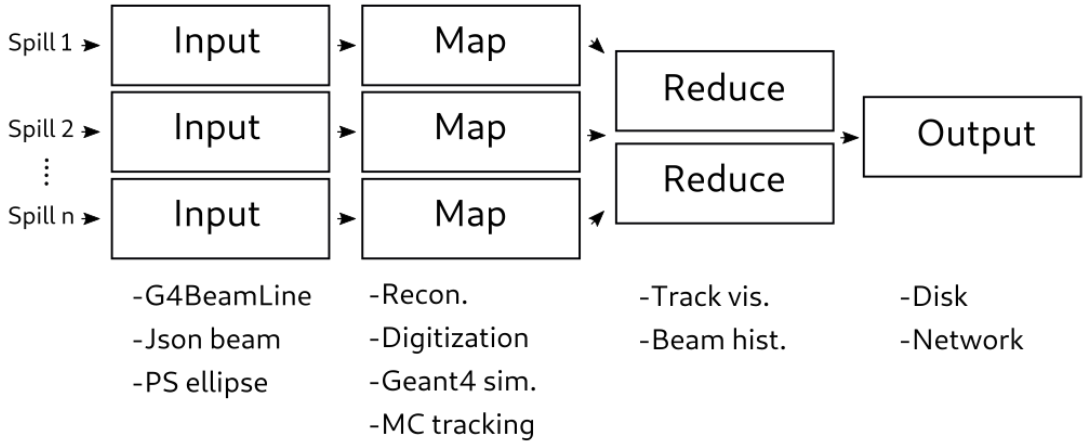

Figure 2.10: An illustration of the MICE module roles in the map-reduce framework.

2.3 Demonstration of cooling by MICE

The cooling study discussed in this section measured the performance of LiH and liquid-H_2 and made comparisons to the simulation. Data were also collected with no absorber and with the empty vessel. The MICE beamline and cooling channel configuration was the same as that used for the data analysed in the MCS measurement of this thesis and is explained in detail in section 2.1. In the cooling study however the spectrometer solenoids, matching coils and absorber focus coils were used in the reverse polarity setting (flip-mode). While for the MCS measurement the magnets were not operational. In flip-mode the magnet polarities either side of the absorber had opposite polarities. In this way the canonical angular momentum increase observed at the fringe fields of solenoid magnets have opposite direction to prevent build-up [63]. The focus coils of the absorber created the low transverse-betatron (beam waist) region by focussing the beam in the transverse direction, a condition for effective cooling in IC (eq. 1.5).

Data from three beams of 4, 6, 10 $\mathrm{mm \cdot rad}$ transverse normalised emittance ($\varepsilon_\perp$) with nominal beam momenta at the centre of the absorber of 140 MeV/c were used. The beam emittance was inflated from 4 $\mathrm{mm \cdot rad}$ — the unperturbed beam

reaching the cooling channel — with the diffuser [64], a device that inserts variable thickness high-Z material in the beam path. Muon beam purity was enhanced by a velocity cut using the TOF hodoscopes combined with precise momentum measurement from the spectrometers. The tracks included in the analysis were also previously subject to a goodness-of-fit cut. Finally, tracks were subject to fiducial selections that rejected tracks expected to have crossed extra material at the edge of the channel's acceptance (scraping) in both trackers.

The study compared the amplitude of the beam before (upstream) and after (downstream) the interaction with the absorber. The upstream sample was composed of particles that were reconstructed by the upstream tracker and passed all selection. The downstream sample was a sub-set of the upstream-sample that was contained in the active volume of the tracker. Figure 2.11 shows the amplitude distribution of the three beams across the four absorber configurations.

Each of the samples of figure 2.11 had between 30,000 and 170,000 events. In the left column, the $4\,\mathrm{mm}\cdot\mathrm{rad}$ beam shows only slight differences between the upstream and downstream sample as it is close to equilibrium emittance. The effects of LiH and liquid-H_2 become clear in the $6\,\mathrm{mm}\cdot\mathrm{rad}$ where there is significant migration of events from the boundaries of the beam to the core. The $10\,\mathrm{mm}\cdot\mathrm{rad}$ case, shows good cooling-performance for both liquid-H_2 and LiH.

Emittance was not used as a metric of phase-space volume due to a failure in one of the matching coils, whose role was to match the Twiss parameters of the beam between the optical elements of the two tracker modules. The collaboration is expecting to publish the results of a higher-order analysis that will also show the evolution of emittance though the cooling channel.

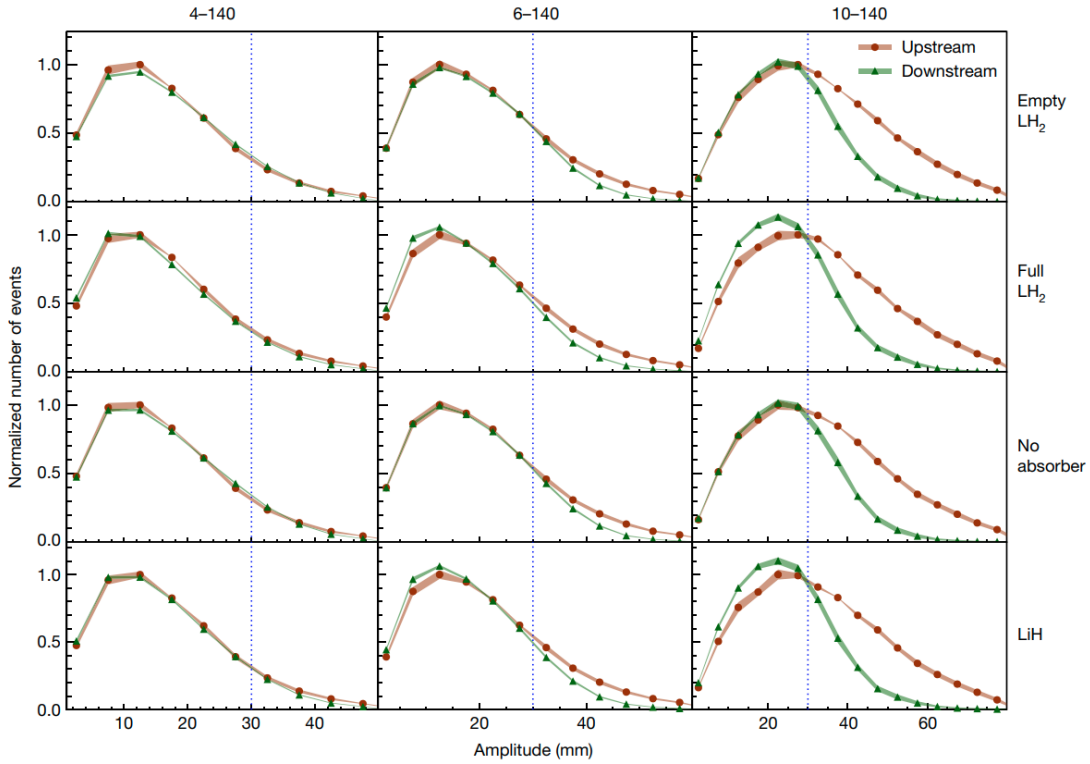

Figure 2.11: Particle amplitude distributions in 5 mm bins of the upstream (red) and downstream (green) samples for the three beams, labelled by '$\varepsilon_\perp$(mmrad)-p_z(MeV/c)' e.g. '4-140', across the four absorber configurations. The bin contents are scaled by $1/A^{US}_{max}$, with A^{US}_{max} the maximum bin content. The coloured bands show the standard error. The blue dotted line shows the approximate channel acceptance. The figure was published by MICE in [41].

Chapter 3

Theory

In this chapter a minimal theoretical basis is introduced regarding beam transport, particularly for apparatus that is present in the MICE beamline. Then, a description of beam emittance and related metrics is made before discussing energy loss and MCS of charged particles during passage through matter.

3.1 Beam description

A beam can be described by the distribution of constituent particles in a phase- or trace-space vector $\vec{A} = [\vec{i}, \vec{p}_i]$ with $i = x, y, z$. The two definitions are distinguished by dependence of $\vec{i}$ and $\vec{p}_i$ to the time coordinate, e.g. $\vec{p}_i(t)$ (phase-space) or to the z-axis, e.g. $\vec{p}_i(z)$ (trace-space). Often the terms are used interchangeably in publications. The latter vector definition is used in this text, with the z-dependence implied from here on. Dividing the momentum vector by $|\vec{p}|$, the transverse components are sufficiently described by $\vec{A}_{TS} = [x, x' = \frac{p_x}{|\vec{p}|}, y, y' = \frac{p_y}{|\vec{p}|}]$. The x and y coordinates are oriented in accordance with the MICE coordinate system with y in the vertical direction and x in the horizontal. The z-axis is usually taken to be the experimental axis however accelerator facilities are often closed loops; even when they are not, straight sections are often combined with bends. Instead of

defining trace-space coordinates with reference to an arbitrary stationary point, a coordinate system is considered that follows an ideal path. The z-axis is tangential to that path, with the positive sign aligned with the momentum vector $\vec{p}_0$ of the reference particle which has a trace-space vector $\vec{A}_0 = [0, 0, 0, 0]$. This coordinate system rotates so that x, y and z are orthogonal to each other.

3.2 Beam transport

The reference particle and the beam distributed in $\vec{A}$ with with central values $\vec{A_0}$ is kept on the ideal path through the Lorentz force:

$$\vec{F}_L = \vec{v}\frac{d\vec{p}}{dz} = q(\vec{E} + \vec{v} \times \vec{B}) \tag{3.1}$$

provided by electromagnets in varying configurations that guide and focus the beam. Longitudinal electric fields are more often used to provide acceleration, or in low particle-energy applications for beam guidance. Otherwise, the transverse static magnetic fields generated by dipoles and quadrupoles are the most likely elements in beam transport due to the strong interaction between them and fast charged particles. These are configurations of electromagnets with their bore-axis lying on the x-y plane, as shown in figure 3.1. They provide the required focussing (quadrupoles), otherwise a non-laminar beam grows continuously, and centripetal acceleration along arcs (dipoles).

A dipole magnet comprises of two coils with aligned polarities that, when considering a reference path that bends on the horizontal (x-z) plane, are positioned above and below the reference axis. In that case, the principle interaction within the dipole volume is between the B_y and p_z components of the beam which results in a curved path. The magnetic flux density required for a reference particle with momentum p_0 and charge q to complete an arc-length of bending radius ρ is obtained by equating the centrifugal force with the Lorentz force which produces

$B_y = p_0/q\rho_x$. Two typical dipole geometries, distinguished by the different angle the entrance and exit faces form with the beam path, are shown in figure 3.2. Rectangular magnets weakly focus in the vertical (y-z) plane, while sector-dipoles have a similar effect on the horizontal plane.

Quadrupole magnets (figure 3.1 right) focus in one of the transverse directions while simultaneously defocusing in the other. They comprise of coils with their bore-axes lying on the diagonals of the x-y plane, with anti-parallel polarities for each diagonal pair. The quadrupole strength k can be calculated in terms of the number of loops n, current I and aperture diameter r using $k = 2q\mu nI/p_0r^2$ (m^{-2}), with μ the permeability of space.

Approximations for the magnetic flux density ($\vec{B}$) generated by these configurations can be calculated as superpositions of fields by multiple sources (multipole expansion) [65]. By using these field configurations with expression 3.1, linearised equations describing the transverse orbit of an individual particle in the the moving reference frame (as described in 3.1) through field-free drift lengths or due to the interaction with sector dipole and quadrupole magnets are derived in multiple sources [66, 67]. A form is given in [66][1], which without a particular choice of bending plane can be rewritten as:

$$\begin{aligned} \frac{d^2x}{dz^2} + \left(\frac{1}{\rho_x^2} + k\right)x - \frac{1}{\rho_x}\frac{\Delta|p|}{|p_0|} = 0, \\ \frac{d^2y}{dz^2} + \left(\frac{1}{\rho_y^2} + k\right)y - \frac{1}{\rho_y}\frac{\Delta|p|}{|p_0|} = 0, \end{aligned} \tag{3.2}$$

with $\rho_{x,y}$ designating the bending action of dipoles in either plane, k the focussing strength associated with quadrupoles and $\Delta p = p - p_0$ the small momentum deviations from the reference particle in a quasi-monochromatic beam.

Without the presence of magnetic fields, k and $1/\rho$ are reduced to zero. The equations of motions then simply state:

[1] Expression 1.25

$$\begin{aligned} \frac{d^2x}{dz^2} = 0 &\implies \frac{dx}{dz} = \mathrm{C} = x', \\ \frac{d^2y}{dz^2} = 0 &\implies \frac{dy}{dz} = \mathrm{C} = y'. \end{aligned} \tag{3.3}$$

In the presence of a dipole magnet ρ can be either positive or negative depending on the orientation of the curvature while k is reduced to zero. In the moving reference frame and within the volume of the dipole, a monochromatic beam will simply drift; the equations of transverse motion can be approximated by 3.3. Small momentum-deviations however will give rise to a defocussing effect in the bending plane that is expressed by the final term of 3.4. These are caused by the differing centripetal acceleration off-momentum particles experience that leads to diverging exit angles.

Sector dipoles also produce the $1/\rho_{x,y}^2$ term in 3.4 that expresses a weak horizontal focussing effect caused by the increased arc-length followed by particles that are displaced outward in the bending plane. Depending on the angle of entrance to a rectangular dipole (ϕ in figure 3.2) and the shape and scale of the gradual build-up of transverse fields at the boundaries, additional vertical focusing actions are introduced [68].

During passage through a quadrupole that focusses on the x-axis ($k < 0$) and defocusses on the y-axis ($k > 0$), without bending action ($1/\rho = 0$), the equations of motion must satisfy:

$$\begin{aligned} \frac{d^2x}{dz^2} - kx = 0, \\ \frac{d^2y}{dz^2} + ky = 0. \end{aligned} \tag{3.4}$$

The transverse force due to a quadrupole of finite length (L) acting on a particle must vary linearly (ideally) with the transverse displacement. Therefore, solutions

to the equations of motion can be of the form:

$$\begin{aligned} x(z) &= x_0 \cos(\sqrt{|k|}L) + \frac{x_0'}{\sqrt{|k|}} \sin(\sqrt{|k|}L) \\ y(z) &= y_0 \cosh(\sqrt{|k|}L) + \frac{y_0'}{\sqrt{|k|}} \sinh(\sqrt{|k|}L) \end{aligned} \tag{3.5}$$

An analogy is made in textbooks between the effects of transport elements on a beam of charged particles and thin optical lenses on rays of light. In this convention, the equations of motion are used to derive linear transfer maps that act on individual trace-space vectors. A transfer map for a drift-space that propagates a trace-space vector $\vec{A}_1$ for a distance d is easily derived by the equations of motion 3.3:

$$\boldsymbol{M}_o = \begin{bmatrix} 1 & d & 0 & 0 \\ 0 & 1 & 0 & 0 \\ 0 & 0 & 1 & d \\ 0 & 0 & 0 & 1 \end{bmatrix} \Rightarrow \boldsymbol{M}_o \cdot \vec{A}_1 = \vec{A}_2 = \begin{bmatrix} x + x'd \\ x' \\ y + y'd \\ y' \end{bmatrix} \tag{3.6}$$

Using the equations of motion for a quadrupole seen in expression 3.5, a transfer map is derived for focussing on the x-axis while simultaneously defocussing on the y-plane:

$$\boldsymbol{M}_{qF} = \begin{bmatrix} \cos(\sqrt{|k|}L) & \frac{1}{\sqrt{|k|}} \sin(\sqrt{|k|}L) & 0 & 0 \\ -\sqrt{|k|} \sin(\sqrt{|k|}L) & \cos(\sqrt{|k|}L) & 0 & 0 \\ 0 & 0 & \cosh(\sqrt{|k|}L) & \frac{1}{\sqrt{|k|}} \sinh(\sqrt{|k|}L) \\ 0 & 0 & \sqrt{|k|} \sinh(\sqrt{|k|}L) & \cosh(\sqrt{|k|}L) \end{bmatrix} \tag{3.7}$$

The analogy to a thin optical lens ($\sqrt{|k|}L << 1$) with focal length $1/f$ is made when the quadrupole length L approaches zero, while $|k|L$ remains constant. This

results to the more intuitive form of 3.7:

$$\boldsymbol{M}_{qF} = \begin{bmatrix} 1 & 0 & 0 & 0 \\ -1/f & 1 & 0 & 0 \\ 0 & 0 & 1 & 0 \\ 0 & 0 & 1/f & 1 \end{bmatrix} \Rightarrow \boldsymbol{M}_{qF} \cdot \vec{A}_1 = \vec{A}_2 = \begin{bmatrix} x \\ x' - x/f \\ y \\ y' + y/f \end{bmatrix} \tag{3.8}$$

Multiple transfer maps can be combined; a triplet quadrupole configuration similar to those encountered in the MICE beamline can be expressed as a product $\boldsymbol{M}_{qF} \cdot \boldsymbol{M}_o \cdot \boldsymbol{M}_{qD} \cdot \boldsymbol{M}_o \cdot \boldsymbol{M}_{qF}$ (FODO configuration) that produces an overall focussing effect in the x-z plane. A de-focussing quadrupole $\boldsymbol{M}_{qD}$ has a transfer matrix with opposite signs to the $1/f$ terms.

On-axis thin solenoid magnets are used for focussing or matching the beam to subsequent transport elements. Ideally, they are characterized by a maximum magnetic flux density that is co-axial with the experimental axis (figure 3.3). Within the bore of the magnet, transverse components of $\vec{B}$ are considered to be zero and increase sharply near the ends of the coils. Any approaching straight particle trajectory that is not co-axial with B_z, within the volume of the solenoid, will be converted to circular (in the x-y plane), or helical in all three dimensions. Due to the $d\vec{B}/dz \neq 0$ areas while approaching, and exiting the solenoid, particles receive an azimuthal force, which results in increased angular velocity within the solenoid than expected without this effect, which in turn results in a radial force due to the primary axial field of the magnet. In cylindrical coordinates, the radial component of $\vec{B}$ is related to $d\vec{B}/dz$ through Gauss's law for magnetism by:

$$\vec{B}_r = -\left(\frac{r}{2}\frac{dB_z}{dz}\right), \tag{3.9}$$

where $r = \sqrt{x^2 + y^2}$. Another consequence of this is that the beam is focussed

simultaneously in both transverse directions with focal length derived in [69] as:

$$\frac{1}{f} = \frac{q^2}{4p_z^2} \int_L B_z^2 dz. \tag{3.10}$$

The integration is through the entrance and exit regions of length L. The transfer matrix of equation 3.8 can be used with negative focal lengths in both transverse planes.

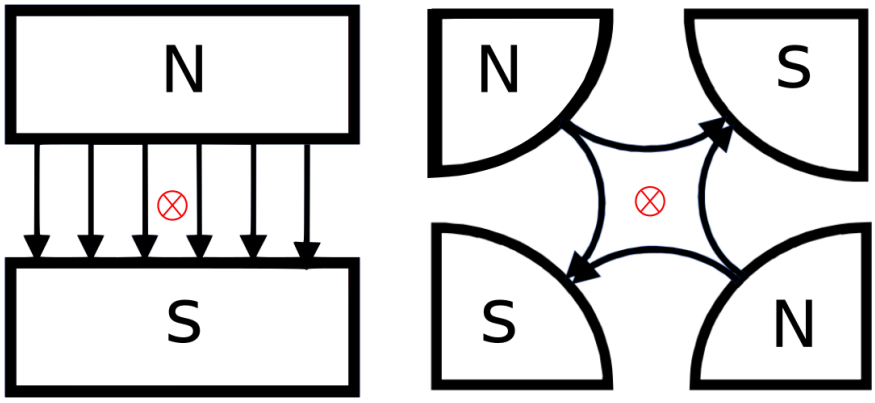

Figure 3.1: Schematics of dipole (left) and quadrupole magnets (right) in the beam path.

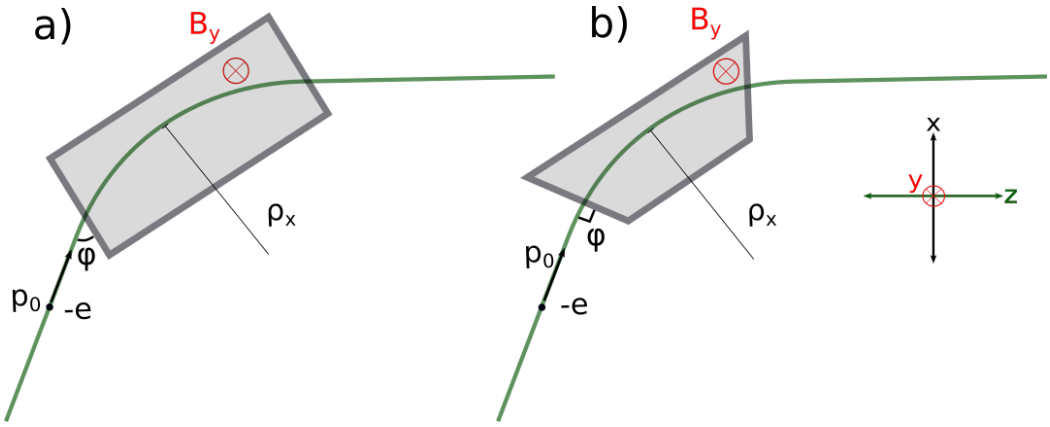

Figure 3.2: Schematic of the action of a rectangular (a) and sector (b) dipole magnet on a particle with charge $-e$ and momentum p_0. The two types are distinguished by the $\phi < 90°$ (rectangular) and $\phi = 90°$ (sector) angle the boundaries form with the reference orbit (green).

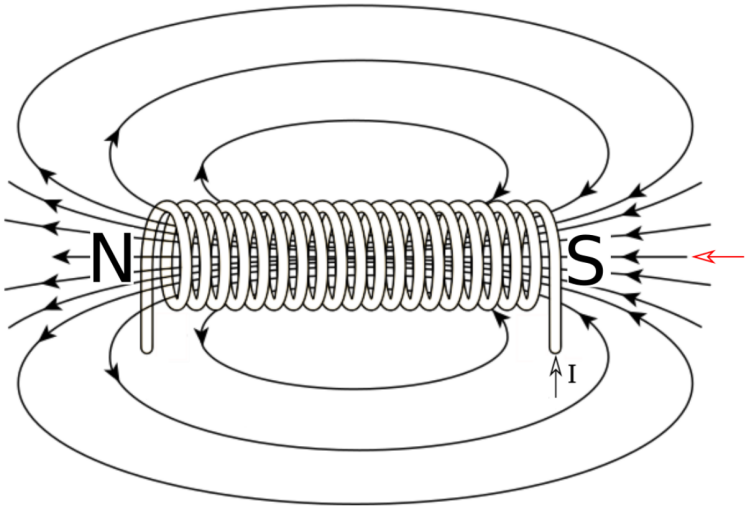

Figure 3.3: Schematic of a solenoid magnet. I shows the current direction, and the red arrow shows the experimental axis.

3.3 Beam Emittance

There are a few variations in use regarding the dimensions and calculation method of emittance which originated from the diverse research aims and measuring apparatus as particle and accelerator physics developed. In trace-space, the area of the distribution of particles such as the one illustrated in pair components $x-x'$ in figure 3.4, divided by π defines the transverse emittance ϵ_x in units of $\pi \cdot \mathrm{mm} \cdot \mathrm{rad}$. Often, the division with π is not used and this is designated in the units by omitting the symbol. Typically, emittance is measured as a holistic property of the beam with devices like the pepper-pot diagnostic [70]. In this study, and all MICE analysis emittance measurements are done in a particle-by-particle basis.

A trace-space distribution of a beam travelling through a lattice undergoes linear transformations such as the ones described in the previous section. Drift sections increase the distributions spatial axis, and periodic focussing and defocussing induce rotations. Passage through material cause the beam to spread in the angular dimension due to MCS. Moreover, for distributions with diffuse limits like the randomly sampled Gaussian distribution of figure 3.4, the area occupied

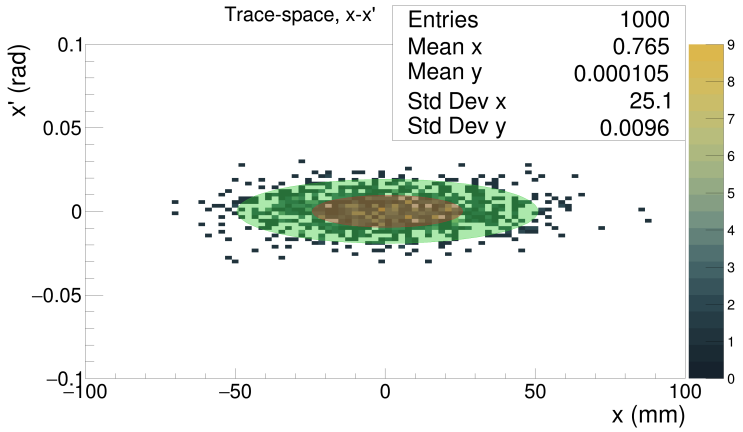

Figure 3.4: Trace-space distribution of a randomly sampled beam in a 2D histogram with bin size 2.2 mm·2.2 mrad with colour designating the number of bin entries (right axis). Ellipses cover the 2σ (brown) and (4σ) (green) areas.

by the beam is ambiguous. An ellipse is chosen to cover a central percentage of the beam. The choice is due to the dynamic shape that can respond to the transformations induced by typical transport elements, while enclosing a central percentage of the beam. For illustration, the 2σ (red) and 4σ (green) areas are enclosed in figure 3.4. The equation for an upright ellipse in $x-x'$ trace-space is expressed below:

$$\left(\frac{x}{X}\right)^2+\left(\frac{x'}{X'}\right)^2=1, \tag{3.11}$$

with X and X' the maximum extent of the ellipse along the horizontal and vertical axes. Multiplying equation 3.11 with XX' expresses the ellipse in terms of the transverse x component of a beam's emittance (with omitted π). To obtain an expression for a tilted ellipse, it is enough to rotate x and x' by an angle θ:

$$\begin{bmatrix} x \\ x' \end{bmatrix}_\theta = \begin{bmatrix} x \\ x' \end{bmatrix} \begin{bmatrix} \cos(\theta) & -\sin(\theta) \\ \sin(\theta) & \cos(\theta) \end{bmatrix} \tag{3.12}$$

By substituting the rotated trace-space coordinates in equation 3.11, equation 3.13 is obtained, with α, β and γ defined as in equation 3.14. These are the

transport, or Twiss parameters, and carry information with regards to the beam distribution and orientation in trace-space, illustrated in figure 3.5;

$$\epsilon_x = \gamma x^2 + 2\alpha x x' + \beta x'^2, \tag{3.13}$$

$$\begin{aligned} \alpha &= -\left(\frac{X'}{X}\right)\sin\theta cos\theta - \left(\frac{X}{X'}\right)\cos\theta\sin\theta, \\ \beta &= -\left(\frac{X'}{X}\right)\sin^2\theta + \left(\frac{X}{X'}\right)\cos^2\theta, \\ \gamma &= -\left(\frac{X'}{X}\right)\cos^2\theta + \left(\frac{X}{X'}\right)\sin^2\theta. \end{aligned} \tag{3.14}$$

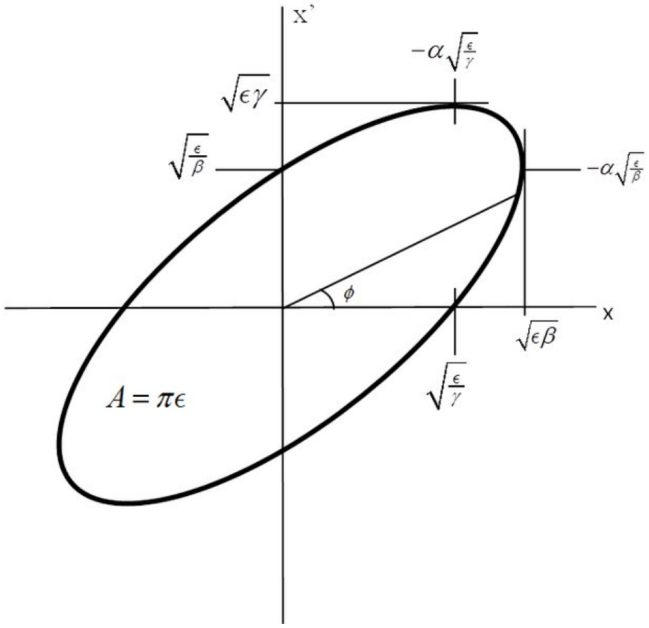

Figure 3.5: An ellipse in phase-space (x,$x' = p_x$) illustrating the relation of the Twiss parameters to the beam's shape from [71].

If $x' = p_x/p_z$, a reduction in emittance is observed during acceleration, although the transverse momentum component stays constant. Often it is useful to define a quantity that is not affected by the changes in p_z. To assess beam quality when acceleration (or deceleration) is significant, normalised emittance is used $\epsilon_{nx} = \beta\gamma\epsilon_x$, with $\beta\gamma$ designating the usual kinematic parameters rather than the

Twiss parameters. Beam cooling techniques are based on momentum damping; in ionization cooling, there is alternation between momentum damping and re-acceleration. In such cases normalised emittance is preferred.

In section 2.3, the transverse beam amplitude appears which is often used as a "single-particle" metric of transverse emittance. It describes the distance, in terms of the trace-space vector, from the beam centre $\langle\vec{A}\rangle$ to the trace-space vector of a particle $\vec{A}$. It is related to emittance and given as:

$$A_{\perp} = \varepsilon_{\perp}(\vec{A} - \langle\vec{A}\rangle)^T \boldsymbol{\Sigma}^{-1}(\vec{A} - \langle\vec{A}\rangle) \tag{3.15}$$

where $\boldsymbol{\Sigma}$ is the covariance matrix of the distribution's trace-space vector:

$$\boldsymbol{\Sigma} = \begin{bmatrix} \sigma_{xx} & \sigma_{xx'} & \sigma_{xy} & \sigma_{xy'} \\ \sigma_{x'x} & \sigma_{x'x'} & \sigma_{x'y} & \sigma_{x'y'} \\ \sigma_{yx} & \sigma_{yx'} & \sigma_{yy} & \sigma_{yy'} \\ \sigma_{y'x} & \sigma_{y'x'} & \sigma_{y'y} & \sigma_{y'y'} \end{bmatrix} \tag{3.16}$$

with σ_{ij} denoting the covariance between variables i and j.

Another important relationship is that of emittance and beam brightness. The metric was adopted from optics where it is used as a metric of quality of a light source. It is related with normalised emittance by:

$$B_n = \frac{I}{\pi^2 \epsilon_n}. \tag{3.17}$$

The above equation expresses normalised brightness in accordance with normalised emittance, with I being the beam current measured in amperes, making the dimensions of brightness $\mathrm{A/m^2rad^2}$. In a collider, the number of interactions is proportional to the brightness of the colliding beams.

3.4 Energy loss

During passage of a beam of fast charged particles through matter energy loss occurs due to interactions with the atomic nuclei and electron orbitals. Depending on the kinetic energy and identity of the incoming particle and the atomic properties of the material, the interactions between them can result in significant reduction to the beam's energy. Although muons and electrons participate in the same interactions through which energy can be lost with electrons, muons are much less susceptible due to their mass difference ($m_\mu/m_e \sim 206$). The different sources of energy loss when a muon passes through liquid-H_2 are shown in figure 3.6 as a function of muon momentum.

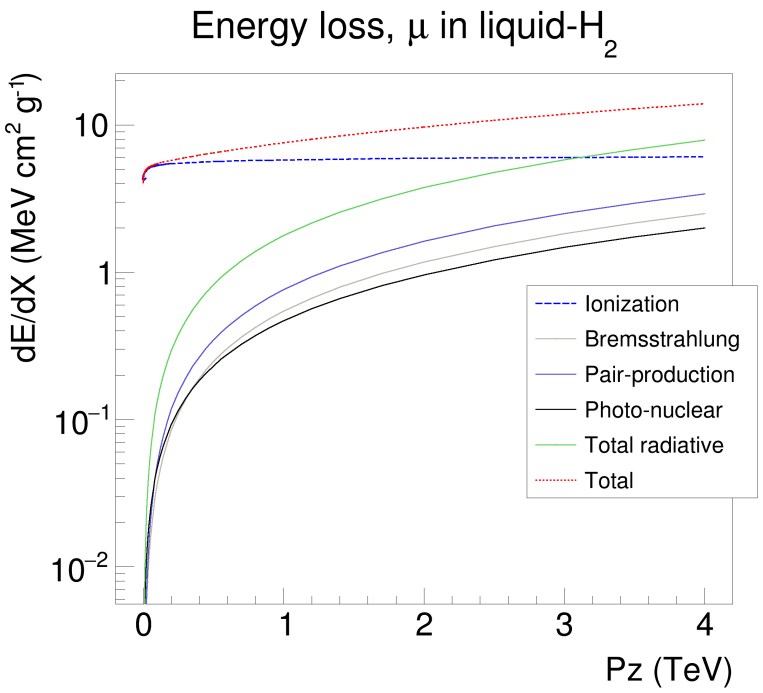

Figure 3.6: Energy loss of muons through liquid-H_2 in $\mathrm{MeVg^{-1}cm^2}$ tabulated calculations from [72].

Radiative phenomena become an important factor at extremely high energies. The muon critical energy, or the point where ionization and radiative losses con-

tribute equally in liquid-H_2 is at 3.1 TeV while for electrons it is $\sim 200\,\mathrm{MeV}$. For the requirements of this study, which looks at 143–250 MeV muons it is enough to only account for collisional ionisation which is described by the Bethe formula:

$$\left\langle -\frac{dE}{dx} \right\rangle = Kz^2 \frac{Z}{A} \frac{1}{\beta^2} \left[\frac{1}{2} \ln \frac{2m_e c^2 \beta^2 \gamma^2 W_{max}}{I^2} - \beta^2 - \frac{\delta(\beta\gamma)}{2} \right]. \tag{3.18}$$

The formula calculates mass stopping power ($\mathrm{MeV\,g^{-}1\,cm^2}$) due to collisional ionisation for passage of a muon (it can be used for any charged particle) with momentum $\beta\gamma m_\mu$ and charge number z, through a material with Z, A atomic number and atomic mass ($\mathrm{g\,mol^{-1}}$), and I the mean excitation energy in eV. The constant K is $4\pi N_A r_e^2 m_e c^2 = 0.307\,\mathrm{MeV\,cm^2\,mol^{-1}}$, where r_e is the classical electron radius, and N_A denotes Avogadro's number. W_{max} is the maximum energy transfer to a single electron and is calculated with

$$W_{max} = \frac{2m_e c^2 \beta^2 \gamma^2}{1 + 2\gamma m_e/m_\mu + (m_e/m_\mu)^2}. \tag{3.19}$$

The term $\delta(\beta\gamma)$ represents the density effect correction in terms of the Sternheimer parameters [73]. Due to the screening of distant charges from polarised proximal orbital electrons, their effect on the incoming particle is reduced. The strength of this effect increases as momentum is reduced and material density increases.

$$\delta(\beta\gamma) = \begin{cases} 2\ln(10)x - \overline{C} & x \geq x_1 \\ 2\ln(10)x - \overline{C} + \alpha(x_1 - x)^k & x_0 \leq x \leq x_1 \\ 0 & x < x_0 \quad \mathrm{non-conductors} \\ \delta_0 10^{2(x-x_0)} & x < x_0 \quad \mathrm{conductors} \end{cases} \tag{3.20}$$

The momentum dependence is seen through $x = \log_{10}(\beta\gamma)$. The derivation of parameters $x_0, x_1, \alpha, \overline{C}$ and δ_0 can be found in [73, 74]. Tabulated calculations of

these parameters are provided by the PDG [72]. For materials that where featured significantly in the MICE apparatus the atomic parameters are provided in table 4.5. In section 4.4 the formula is used to predict energy loss between the midpoints of TOF0-TOF1 and TOF1-TOF2 in the MICE cooling channel. The energy loss in 10 cm of the materials used for this study is shown in figure 3.7. In figures 4.13-4.16 the calculations are compared to momentum measurements for the analysed samples in a 140–250 MeV/c range.

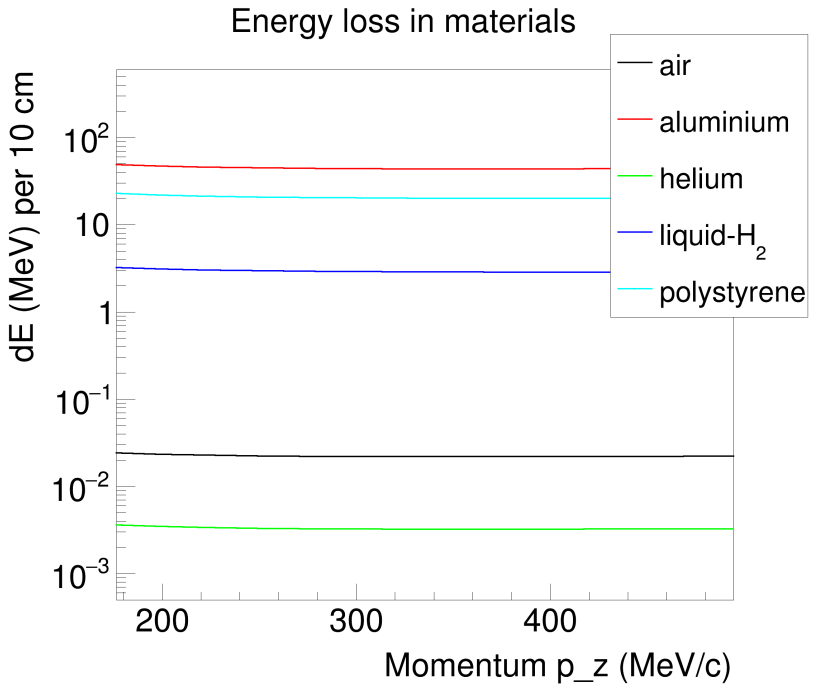

Figure 3.7: Energy loss for muons calculated by equation 3.18 through 10 cm of some of the materials crossed by the MICE beam.

3.5 Rutherford scattering

An early theory for scattering of sub-atomic particles through material was published by Rutherford [75], based on the results of the Geiger and Marsden [76] experiment, which observed the scattering behaviour of α and β particles through

gold. The results, especially the detection of frequent back-scatters was a significant step in the progression of particle physics since it implied higher concentration of electric charge and mass than expected in the target's atomic structure.

The controlling parameters and metrics used to study scattering are introduced in this section, through the scope of Rutherford's analysis, before extending to MCS. An elastic collision of a low-mass incident particle with a stationary and more massive target is considered, in a scenario as illustrated in figure 3.8.

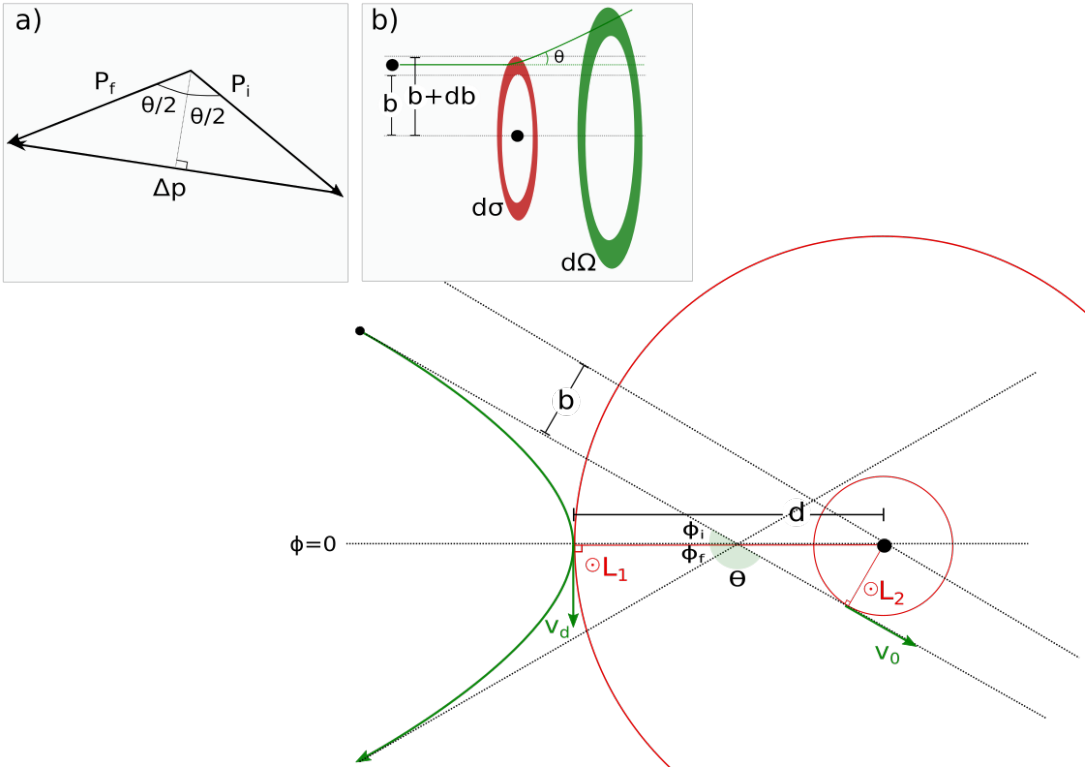

Figure 3.8: A trajectory (green arrow) of a charged ($+q$) particle deflected by the potential of a stationary target with charge (Ze). The deflection is considered around an axis of symmetry ($\phi = 0$) between the incident (ϕ_i) and final directions (ϕ_f). Sub-figure a) shows the difference of the initial and final momenta. Sub-figure b) shows the relationship between the annular cross-section $d\sigma$ (red) and the solid angle interval $d\Omega$ (green).

The interaction between the colliding particles is mediated by the Lorentz force (equation 3.1). The $v \times B$ term expresses the effect of the velocity component

of the incident particle that is perpendicular to $\vec{B}$, which contributes negligible impulse compared to the $\vec{E}$ at low velocities. In this example, as in Rutherford's analysis, only the Coulomb force is considered as expressed below. The equation describes the deflection of a particle approaching from a distance $|\vec{r}|$;

$$\begin{aligned} \Delta\vec{p} &= \int_{t=0}^{t=\infty} \vec{F}_L dt = \frac{Zeq}{k_e} \int_{t=0}^{t=\infty} \frac{\hat{r}}{|\vec{r}|^2} dt \\ \therefore |\Delta\vec{p}| &= \frac{Zeq}{k_e} \int_{t=0}^{t=\infty} \frac{\cos(\phi)}{|\vec{r}|^2} dt. \end{aligned} \tag{3.21}$$

The target has a total charge of Ze, with e the electron charge, and q, the incident particle charge and k_e the Coulomb constant. The condition of elastic scattering implies that the target will not dissipate energy in recoil, but will convert it to electrostatic potential. The incoming particle will not lose momentum $|\vec{p}_i| = |\vec{p}_f|$, but will be redirected ($|\Delta\vec{p}| > 0$). The scattered trajectory will be a parabola, during which angular momentum ($\vec{L}$) must be conserved. At any point in the trajectory, $|\vec{L}| = m|\vec{r}|d\phi/dt$. Rutherford also noted[2] that $|\vec{L_1}| = |\vec{L_2}|$ (as seen in the figure), which gives:

$$m|\vec{v}_d|d = m|\vec{v}_0|b = m|\vec{r}|^2 \frac{d\phi}{dt}, \tag{3.22}$$

that is used to change the expression in the integral from $dt/|\vec{r}|^2$ to $d\phi/|\vec{v}_0|b$. To change the integral limits, the symmetry between the initial and final $\vec{r}$ around the axis $\phi = 0$ is used in combination with $|\phi_i| + |\phi_f| + |\theta| = \pi$, resulting in $\phi_i = (\theta - \pi)/2$ and $\phi_f = (\pi - \theta)/2$. Changing the integration limits and integrating results in

$$|\Delta\vec{p}| = \frac{Zeq}{k_e|\vec{v}_0|b} \cos(\theta/2). \tag{3.23}$$

Also, from the geometry of sub-figure a) $|\Delta\vec{p}| = 2|p_i| \sin(\theta/2)$, producing a

[2] First equation of page 673 in the 1911 paper

relationship between the impact parameter b and the scattering angle:

$$b = \frac{Zeq}{2k_e m|\vec{v}_0|^2} \frac{1}{\tan(\theta/2)}. \tag{3.24}$$

Collisions are typically studied in terms of the differential cross section (DCS) $d\sigma/d\Omega$ measured in barns — a unit of area equal to $100\,\mathrm{fm}^2$ — per solid angle interval $d\Omega$, illustrated in sub-figure b). The area is defined as $d\sigma = 2\pi b db$ and the solid angle by $2\pi \sin(\theta) d(\theta)$, combining with expression 3.24 the Rutherford's scattering DCS is obtained

$$\frac{d\sigma}{d\Omega} = \left(\frac{Zeq}{2k_e m|\vec{v}_0|^2}\right)^2 \frac{1}{\sin^4(\theta/2)}. \tag{3.25}$$

This treatment overestimates scattering due to the screening of the nuclear potential of the target by the orbital electrons. Since the Rutherford cross section analysis there have been many revisions. Geant4 uses the Wentzel cross-section [77, 78]:

$$\frac{d\sigma}{d\Omega} = \left(\frac{Zeq}{2k_e m|\vec{v}_0|^2}\right)^2 \left(\sin^2\frac{\theta}{2} + \frac{1}{4k^2R^2}\right)^{-2} \tag{3.26}$$

where k is the incoming particle's wave-number. Wentzel used an electric potential that reduces at an exponential rate outside a certain radius (R):

$$V(|\vec{r}|) = \frac{Zeq}{\vec{r}} \exp(-|\vec{r}|/R), \tag{3.27}$$

with R estimated from the Thomas-Fermi model as $R = 0.885Z^{(-1/3)}\alpha_0$. Most descriptions of MCS, being multiple successions of the above interaction, adopt a certain family of DCS models.

3.6 Multiple Coulomb scattering

After multiple scattering events, the mean scattering angle is expected to be zero as it is a symmetric process. The width of the angular distribution however is expected to grow. The central 98% of the distribution of angles can be approximated to be Gaussian, with non-Gaussian long tails due to the much less frequent hard-scattering events. An approximation for the width of the Gaussian has been adopted by the Particle Data Group [32] as:

$$\sigma_\theta = \frac{13.6\,\mathrm{MeV/c}}{\beta p}\sqrt{\frac{s}{X_0}}\left(1 + 0.038\ln\frac{s}{(X_0\beta^2)}\right). \tag{3.28}$$

In the above equation s/X_0 is the path length in terms of the radiation length of the material. The formula originates from [79, 80].

Several authors have contributed methods to model the process of MCS precisely. Specifically, to solve the transport equation (Boltzmann equation) for the probability density function $f(\vec{r}(s), \widehat{p}(s))$ given below:

$$\frac{\partial f}{\partial s} - \widehat{p}(s)\nabla f = N\int [f(\vec{r}(s), \widehat{p}(s)) - f(\vec{r}(s), \widehat{p'}(s))]\sigma(\theta_S)d\Omega \tag{3.29}$$

where $\vec{r}(s)$ and $\widehat{p}(s)$ are the position vector and momentum unit vectors of the incident particle as functions of length s through the material and $\widehat{p'}(s)$ is the deflected momentum vector. $N = N_A\rho/A$ is the number of scattering centres per unit volume, with ρ the mass density and A the atomic weight. The above states that the total rate of change of the multi-variate probability density function (p.d.f.) minus the diffusion term (which describes the free propagation of the beam) equals the collisional term (RHS). The integral in the collisional term is across the solid angle Ω. $\sigma(\theta_S)$ expresses the cross section of scattering to the 3D scattering angle $\theta_S = \arccos(\widehat{p}\cdot\widehat{p'})$.

The first publications in 1940 by Williams [81] and [82] and later the Lewis [83] and Molière (revised by Bethe [36]) MCS theories define the problem and start the derivation using the above transport equation and solve for the angular distribution, while Lewis also solves for the spatial distribution. One of the most recent models is the ELMS (Energy Loss Multiple Coulomb Scattering) model that as the name implies accounts for energy loss and is assessed along with the Molière model in the experiment described in section 1.3. Another notable mention is the Carlisle-Cobb [84] model that originated from members of the MICE collaboration.

3.6.1 MCS in Geant4

Geant4 tracks the parameters of the simulated particles in steps of length dependent on the mean free path (λ_{Tot}) of all the involved processes, which is inversely proportional to the total cross-section ($\lambda_{Tot} \sim 1/\sigma$). The tracked parameters include the geometrical position, physical variables such as energy and momentum and particle properties such as mean life-time, decay channels and mass. In every step of propagation the particle can interact with the mapped ambient EM-fields. The propagation path length that the simulation will proceed for each particle is affected by the materials in the geometry and the nature and energy of the particles. In a scenario where the MCS mean free path-length when traversing a material is less than its stopping range, or if there are other geometrical limitations, the step length reduces. Each of these parameters (or distributions) are computed from physical models that are often updated and can be tracked from [85].

By default, MAUS directs Geant4 to use the "QGSP_BERT" [86] reference physics list. In that configuration small-angle EM-scattering is simulated by the "WentzelVI" MCS model [87], while hard-scattering (>0.2 rad) is handled by a single scattering model "CoulombScattering".

3.7 Projected angles

The principal results of this analysis are the plane projected angles θ_x and θ_y. Conventionally these would be defined as:

$$\theta_y = \arctan\left(\frac{dx}{dz}\right)_{DS} - \arctan\left(\frac{dx}{dz}\right)_{US} \tag{3.30}$$

$$\theta_x = \arctan\left(\frac{dy}{dz}\right)_{DS} - \arctan\left(\frac{dy}{dz}\right)_{US} \tag{3.31}$$

expressing the difference of the angles of $\vec{P}_{DS}$ and $\vec{P}_{US}$ when projected onto the x-z (θ_x) and y-z plane (θ_x). It is worth clarifying that the angle subscript denotes the axis around which the angle is measured. The above definitions however could introduce a systematic bias to the measurement if the definition of these planes is inexact. The internal coordinate system of each scintillating-fibre tracker is dependent on the placement of the individual planes within its station and on the precision on which these were measured. The scintillating-fibre trackers however were mostly unavailable for surveying; they were placed within the bore of the spectrometer solenoids and enclosed by aluminium windows to contain the helium. Moreover, each station provides a coupled x-y measurement due to the arrangement of each plane (as discussed in section 2.1.5). To negate this possible systematic bias, $\vec{P}_{US}$ is used to define a principal axis ($\hat{u}$) instead of the z-axis along with the y-axis ($\hat{y}$) of the downstream tracker for each particle. The cross-product $\vec{s} = \hat{u} \times \hat{y}$ defines a mutually orthogonal axis, and $\vec{k} = \hat{u} \times \hat{s}$ defines a third axis. For a particle that is travelling co-axially with the z-axis of the upstream tracker, the s-axis would be the same as the x-axis and the k-axis would coincide with the y-axis. Analytically the projected angles are defined as:

$$\theta_Y = \arctan\left(\frac{\hat{d} \cdot \hat{s}}{\hat{d} \cdot \hat{u}}\right) \tag{3.32}$$

$$\theta_X = \arctan\left(\frac{\widehat{d}\cdot\widehat{k}}{\widehat{d}\cdot\widehat{u}}\right) \tag{3.33}$$

where the $\widehat{\ }$ symbol denotes a unit vector and $\widehat{d}$ corresponds to $\vec{P}_{DS}/|\vec{P}_{DS}|$. Due to the arbitrariness of the choice of the y-axis, these definitions are included as a source of systematic uncertainty to the projected angle distributions. In section 4.5, the distributions are re-calculated with 6 different rotations to the above $\widehat{y}$-vector around the z-axis.

Additionally, the distribution of the three-dimensional (or polar) scattering angle θ_S is used to compare the scattering angle between the particle tracks reconstructed by the upstream tracker ($\vec{P}_{US}$) and the downstream tracker ($\vec{P}_{DS}$) by their dot product:

$$\theta_S = \arccos\left(\frac{\vec{P}_{US}\cdot\vec{P}_{DS}}{|\vec{P}_{US}||\vec{P}_{DS}|}\right) \tag{3.34}$$

Chapter 4

Methods

4.1 MICE data

The MICE data are divided in run-numbers that each can contain data from a few hundred to up to around 5,000 dips of the target (spills) in the ISIS proton beam path, and duration that ranges from minutes to a couple of hours. The data used in this study were gathered with the vessel filled with liquid-H_2 during the period 28/9/2017–11/10/17, (ISIS user cycle 2017/02) and with the vessel evacuated in the ISIS user cycles 2017/03–04 – during the period 24/10/2017–22/11/2017 – a month before decommissioning of the experiment began. For each of the two vessel configurations, three different momentum-settings were used that will be referred to as "low-p", "mid-p" and "high-p" in this analysis, with the explicit calculation of momenta covered in sub-section 4.4. Identical momentum-settings were used with the evacuated and full absorber vessel. All beams were $3\,\pi\,\mathrm{mm\,rad}$ pionic-beams, with a $29\,\mathrm{mm}$-thick proton absorber in place downstream of the DS. All magnets downstream of the final quadrupole were not operational during data-taking for these run-numbers (included in table 4.1), producing straight tracks through the cooling channel. Appendix A shows the data selected in the $x-x'$ and $y-y'$ trace-space, for the full liquid-H_2 vessel and an empty vessel configurations,

low-p		mid-p		high-p	
liquid-H_2	Empty abs.	liquid-H_2	Empty abs.	liquid-H_2	Empty abs.
9772	10092	9773	10156	9935	10159
9774	10153	9776	10157	9936	10162
9775	10154	9779	10158	9938	10169
9777	10155	9855	10164	9939	10175
9778	10165	9857	10168	9940	10180
9854	10167	9858	10182	9942	10181
9859	10173	9860	10183	9943	10189
9861	10186		10203	9944	10199
	10202		10207	9945	10200
					10201
					10208
					10209
					10210

Table 4.1: MICE run-numbers used in this study across the three momentum-settings and absorber configurations.

compared to the same variables plotted for MC in appendix B.

4.2 Measurement of MCS

In total, twelve data-sets were considered; six of which were MC simulations generated by MAUS coupled with Geant4 as described in section 2.2. The aim of the analysis was to assess if the accuracy of the simulation in predicting MCS declines with the liquid-H_2 in the beam path. The analysis method expanded on analytical methods from the LiH (LiH) MCS analysis [88]. The differences in the beam-mode (muonic-beam for LiH, pionic beam for liquid-H_2) and a complex vessel structure [47], necessitated by the volatile nature of liquid-H_2 meant that this analysis required to account for additional features and systematic uncertainties.

The simulation through the MICE cooling channel was performed with primary particles generated by G4Beamline, which simulated the three composite beams captured by the MICE beamline. The primary particles were propagated by MAUS from $1\,\mathrm{m}$ downstream of D_2 to the end of the MICE cooling channel. The next

subsection discusses the criteria used to select the measurement sample, a process that is nearly identical for both data and simulation. The only difference being that the simulated beam was weighted to match the experimentally measured momentum distribution calculated from the TOF0-1 time-of-flight as described in section 4.2.3.

4.2.1 Selection criteria

The aim of the reduction of the data was to control the systematic uncertainties. A set of criteria selected particles for MCS measurement based on information taken upstream of the interaction point. Event selection was based on the following philosophy: The sub-sample should have passed through a region of nearly homogeneous reconstruction efficiency with optimum detector performance; only events reasonably expected to have generated a downstream track should be considered; the trajectories should be well-reconstructed and the momentum spread adequately low to present a useful measurement. Analytically, the selection criteria were applied in the following order:

- Only particles with a single space-point (SP) in each of the TOF0 and TOF1 hodoscopes
- and a single reconstructed track in the US scintillating-fibre tracker were taken into consideration.
- The trajectory was estimated to have less than 90 mm radius at the diffuser.
- The track was assessed to be a good fit to the signal clusters formed at the trackers ($\chi^2/\mathrm{NDF} < 4$).
- The expected position at the DS tracker was expected to be within 100 mm of the beam axis

- and finally have a transit time from TOF0 to TOF1 within a selected range (table 4.3).

The survival rates for each cut is shown in table 4.2. The first requirement pertained to the time-of-flight measurement which is important for particle identification and in controlling the momentum spread of the final sample. The singular SP criterion was required to avoid any ambiguity in the calculated velocity. TOF1 was placed 7.64 m downstream of TOF0 with their midpoint at 7.84 m from the centre of the absorber, which was approximately the point where the particle's instantaneous velocity corresponded to.

If an upstream track was available, the trajectory was backwards-propagated by the distance from the tracker's down-stream-most reconstruction station to the diffuser's position using equation 3.6. The distance of each particle at that z-point was calculated with $R = \sqrt{x^2 + y^2}$. The distributions of R for all data-sets are shown in figure-block 4.1. When the diffuser was retracted, an annular region of $\sim 100\,\mathrm{mm}$ radius was left open. Particles that originated from close-to or further out of that limit are expected to have crossed the high-Z material of the diffuser's structure. The core of the beam however is expected to have passed clear. Allowing for the outliers that passed through the excess material to be included in the analysis would result in an asymmetric particle momentum distribution and increased uncertainties in the final results, and were therefore rejected.

After the χ^2/NDF cut (figure-block 4.2), which had a relatively small impact to the sample numbers, the upstream tracks were extended to the final station of the downstream tracker and the distance from the reference axis was calculated for each particle. If that was found in the central $\pi \cdot 100^2\,\mathrm{mm}^2$ area it was included in the final sample (figure-block 4.3). Because particles had drifted field-free for several meters from the final set of quadrupoles, the beam occupied a large volume compared to the active volume of the trackers. The trackers were also expected to have slightly reduced (and potentially an-isotropic) reconstruction performance

P_z (MeV/c), abs.	Data (MC) percentage passing each criterion					
	TOF01 SP	Single UST	Diffuser cut	χ^2/NDF Cut	Radial cut	TOF range
Empty, low-p	72.8 (83.1)	43.9 (52.3)	37.5 (46.5)	37.1 (46.2)	1.19 (1.73)	0.38 (0.44)
LH_2, low-p	78.5 (83.1)	47.5 (52.3)	40.3 (46.4)	39.9 (46.1)	1.29 (1.69)	0.411 (0.434)
Empty, mid-p	65.1 (82.4)	18 (23.5)	11.8 (14.5)	11.7 (14.4)	0.925 (1.19)	0.323 (0.299)
LH_2, mid-p	71.7 (82.5)	20 (23.5)	13.2 (14.6)	13 (14.4)	1.02 (1.19)	0.363 (0.3)
Empty, high-p	63.3 (82.9)	16.6 (25.2)	12.8 (19.5)	12.7 (19.3)	0.337 (0.859)	0.137 (0.28)
LH_2, high-p	70.2 (82.9)	18.6 (25.2)	14.3 (19.5)	14.2 (19.3)	0.384 (0.844)	0.171 (0.279)

Table 4.2: Table showing the percentage of events passing each cut, compared to all triggers.

in the outer edges. In addition, only particles for which a downstream track was available could meaningfully contribute to the measurement. The ratio of tracks that drifted outside the channel before reaching the downstream tracker could not contribute meaningfully to the results. This selection reduced that number to $\sim 10\,\%$ of the total number of reconstructed upstream tracks that had passed all other selection.

Finally, the measured upstream velocity was assessed, coming from the TOF1-TOF0 traversal time (distributions in figure-block 4.4). The pionic beam-mode was used to collect the data analysed in this study. This meant that a composite beam of positive electrons, pions and muons reached the cooling channel. These particles were products of the proton-proton collisions at the target and still carried most of that momentum. Due to their mass difference, and different energy-loss rate, they were well separated in velocity and hence time-of-flight. Electrons were the fastest species in the MICE beamline, and travelled at approximately the speed of light, followed by muons and pions. Section 4.4 describes how the electron traversal time was used to approximate the speed-of-light to calculate momentum for the particles that had a flight-time within the ranges defined in table 4.3. Those ranges are defined as the $\pm 2\sigma$ widths of a Gaussian fitted to the the muon time-of-flight distribution around the middle peak.

The projected radii at the diffuser (figure-block 4.1) show a mean-offset between simulation and experimental data in the order of 10 mm. The mid-p MC beam of sub-figure c) and d) also show a secondary peak at 170 mm that appears

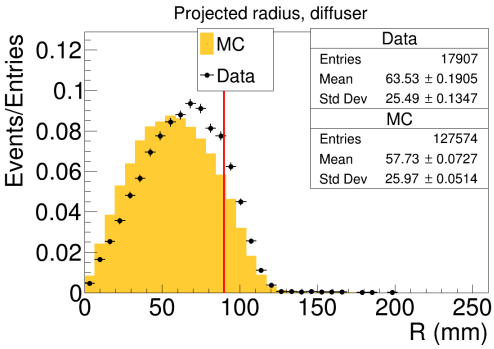

(a) Absorber Empty, low-p beam

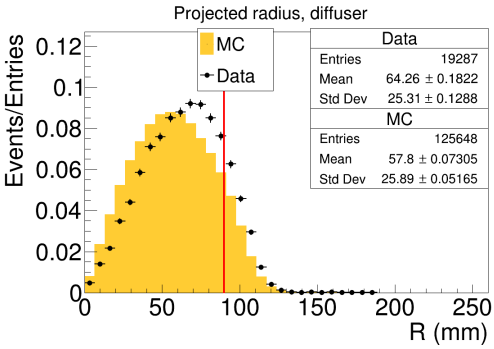

(b) Liquid-H_2, low-p beam

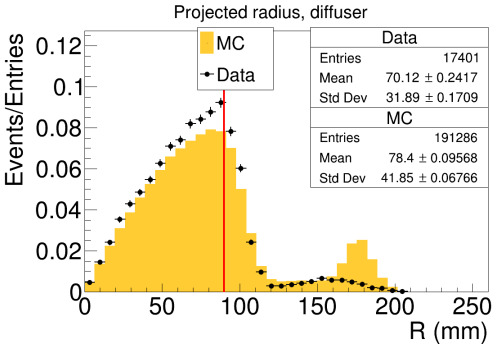

(c) Absorber Empty, mid-p beam

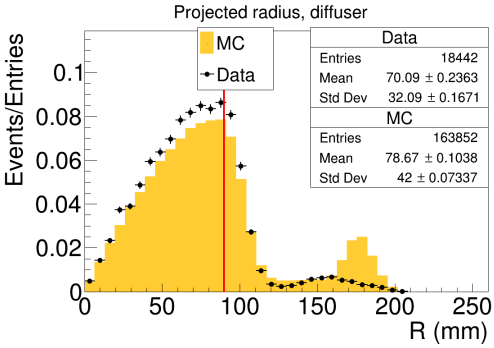

(d) Liquid-H_2, mid-p beam

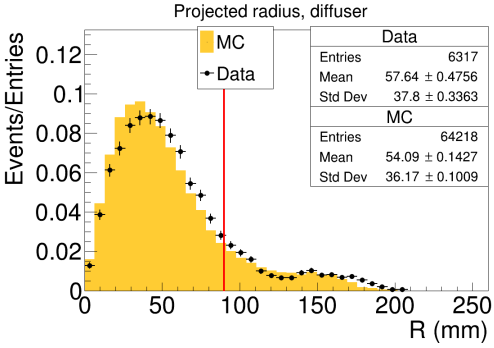

(e) Absorber Empty, high-p beam

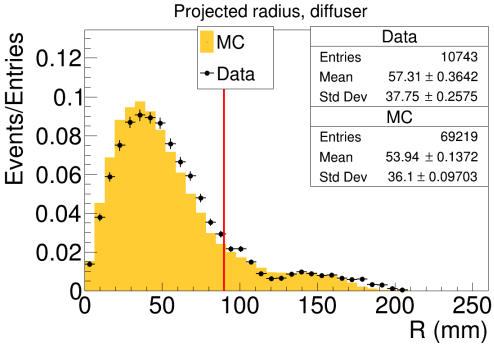

(f) Liquid-H_2, high-p beam

Figure 4.1: Projected radius of particles at the diffuser. Those found above 90 mm from the experimental axis are rejected.

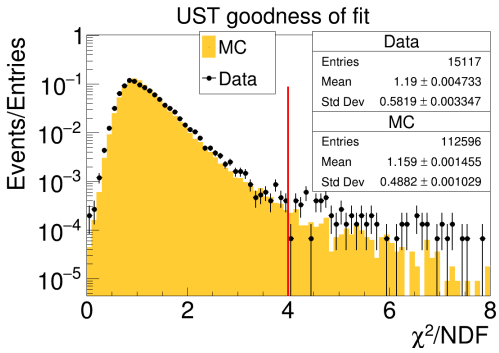

(a) Absorber Empty, low-p beam

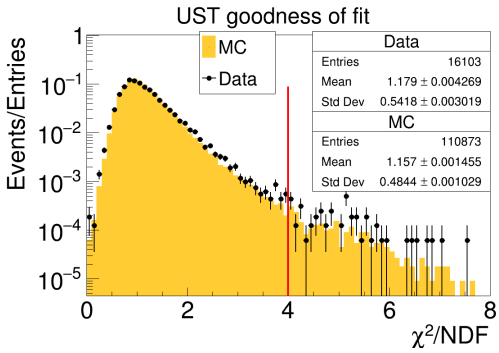

(b) Liquid-H_2, low-p beam

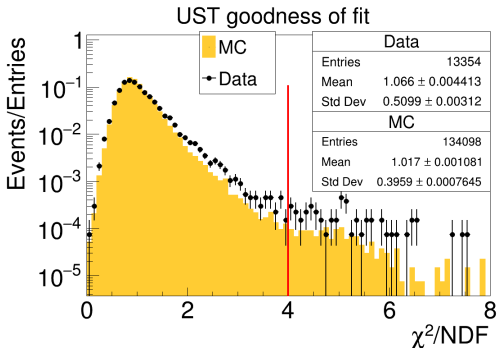

(c) Absorber Empty, mid-p beam

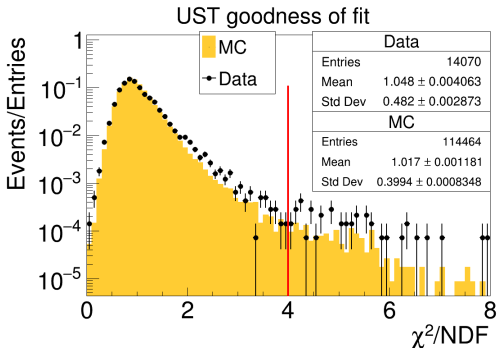

(d) Liquid-H_2, mid-p beam

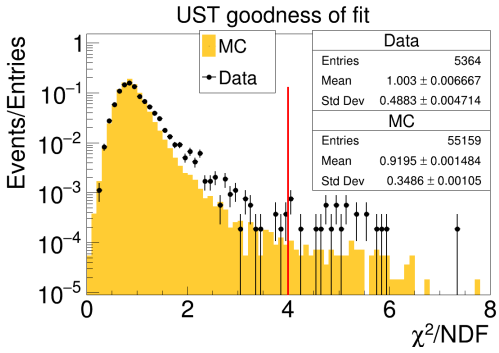

(e) Absorber Empty, high-p beam

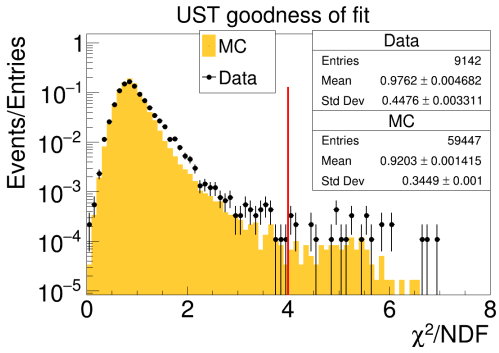

(f) Liquid-H_2, high-p beam

Figure 4.2: χ^2/NDF distribution of particles at the UST. Tracks with a χ^2/NDF for the straight-track fit at the scintillating-fibre stations found to be over 4 were rejected.

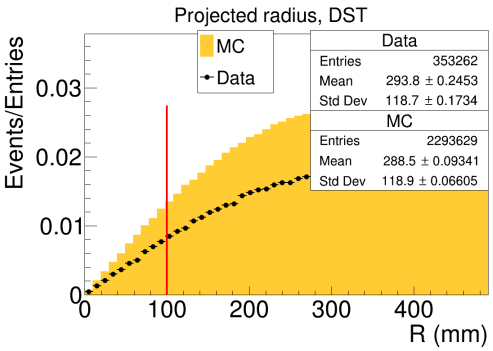

(a) Absorber Empty, low-p beam

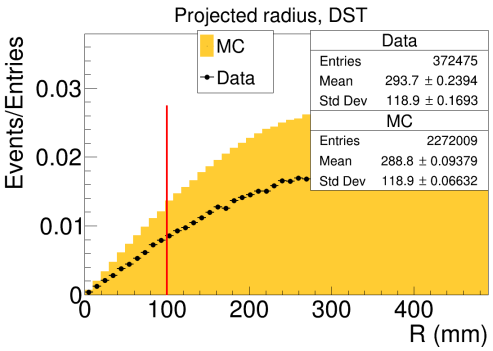

(b) Liquid-H_2, low-p beam

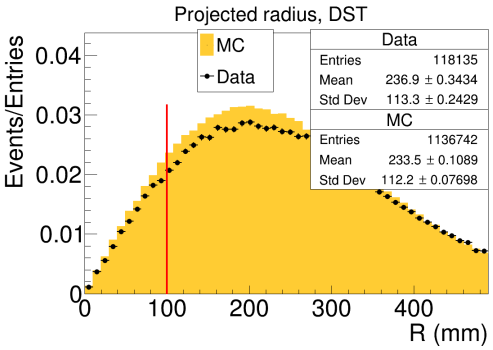

(c) Absorber Empty, mid-p beam

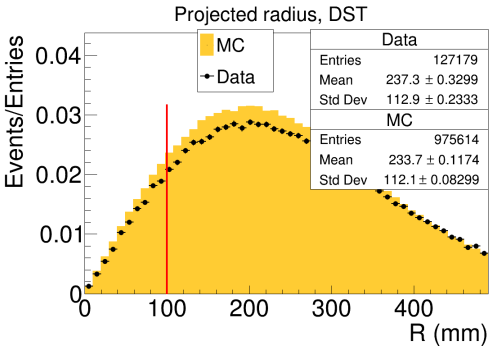

(d) Liquid-H_2, mid-p beam

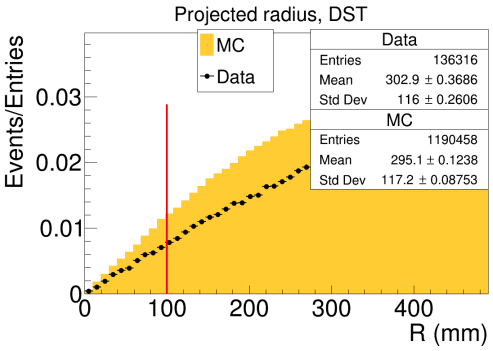

(e) Absorber Empty, high-p beam

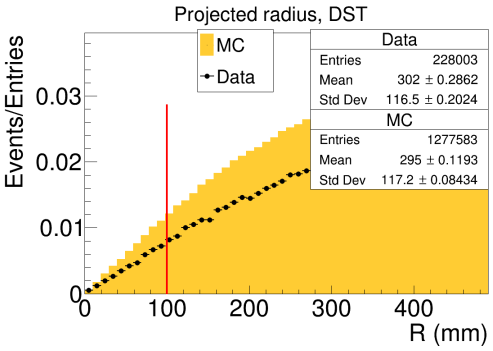

(f) Liquid-H_2, high-p beam

Figure 4.3: Distributions of projected radius at the final station of the DST. Tracks that extended to over 100 mm were rejected.

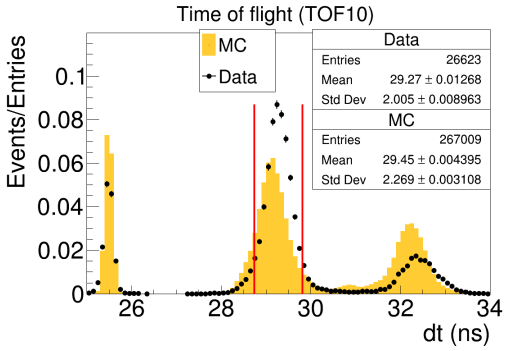

(a) Absorber Empty, low-p beam

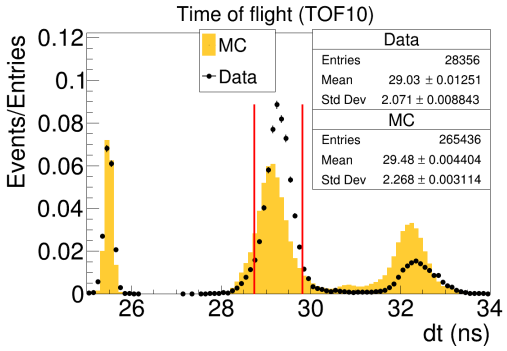

(b) Liquid-H_2, low-p beam

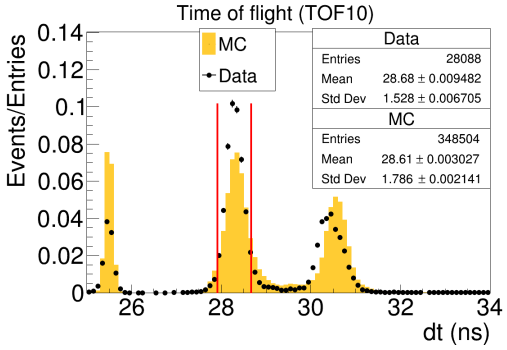

(c) Absorber Empty, mid-p beam

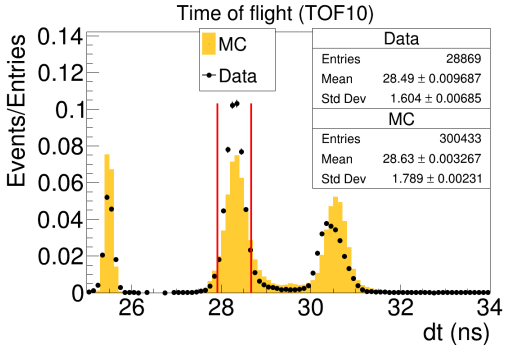

(d) Liquid-H_2, mid-p beam

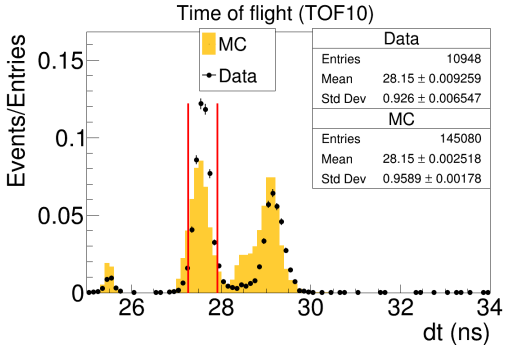

(e) Absorber Empty, high-p beam

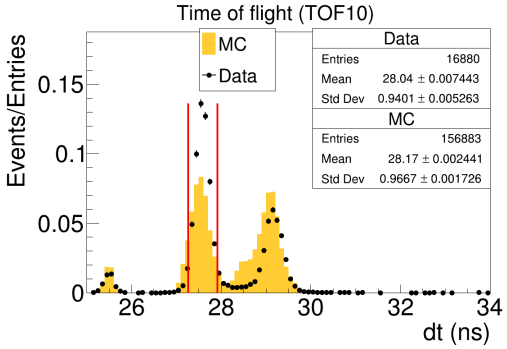

(f) Liquid-H_2, high-p beam

Figure 4.4: TOF distribution for all particles that passed the radial selection. Particles with time-of-flight outside the illustrated ranges were rejected. The selected ranges are shown in table 4.3.

Nominal momentum	TOF range (ns)	P_z-range (MeV/c)
low-p	28.0–30.0	232.5–170.2
mid-p	27.5–29.0	261.1–194.8
high-p	27.0–28.1	302.7–227.8

Table 4.3: Table showing the TOF selection range. The same limits are applied for MC, data and liquid-H_2 and the empty vessel case for each nominal beam momentum.

to be suppressed in the experimental distributions. The quality of fit (χ^2/NDF) distributions of figure-block 4.2 are populated by events that passed the diffuser cut and show adequate agreement, confirming that the performance of the trackers is predicted correctly. The simulated beam also shows discrepancies in figure-block 4.3, where the distributions of projected radii at the final station of the DS tracker are compared with the experiment.

The radial selections at the diffuser and the final station of the DS tracker removed most of the particles that were over-represented by the simulation thus reducing the discrepancy. This can be confirmed through the figures in Appendix A and B, where the trace-space distributions of the final sample at the US tracker (left columns) are plotted for the experimental data (figure-blocks A.3, A.4, A.1, A.2) and MC (figure-blocks B.3, B.4, B.1, B.2), where good agreement is observed.

Finally, the time-of-flight distributions of figure-block 4.4 shows that the presence of electrons, pions and muons in the surviving sample were not represented accurately by the simulation. The time-of-flight selection however removed most pions and electrons. The slight offset of the remaining muonic peak was mitigated by statistically weighting the MC events as discussed in section 4.2.3.

The observed discrepancies were likely caused by small-scale offsets between the actual placement of the transport elements in the experimental hall and those documented in the simulation configuration or due to variations in the ISIS proton-beam that were not included in the configuration of G4BeamLine.

4.2.2 Path-length through liquid-H_2

The path-length through liquid-H_2 was calculated by projecting individual upstream and downstream tracks to the point of intersection with the upstream and downstream absorber windows and calculating the distance between the two intersection points. The shape of the absorber vessel windows, seen in figure 2.7, was fitted with a 9th order polynomial that calculated the window radius from the z-position. The resulting path-length distributions are shown in figures 4.5–4.7.

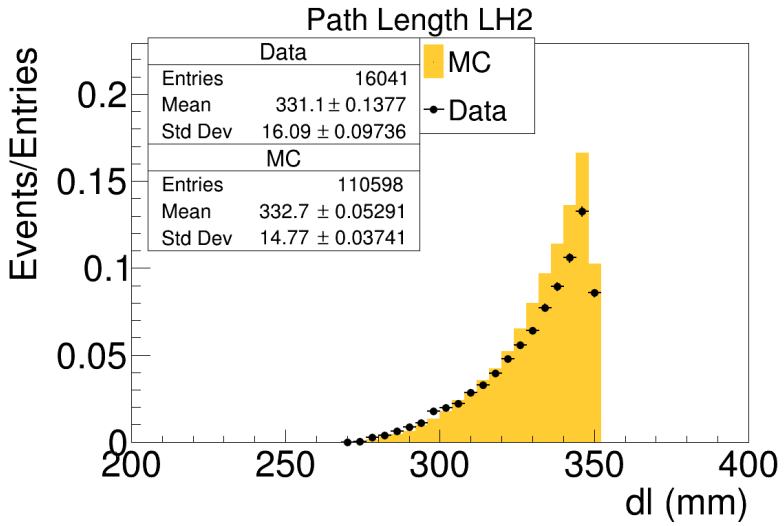

Figure 4.5: Projected path-length through liquid-H_2, low-p beam.

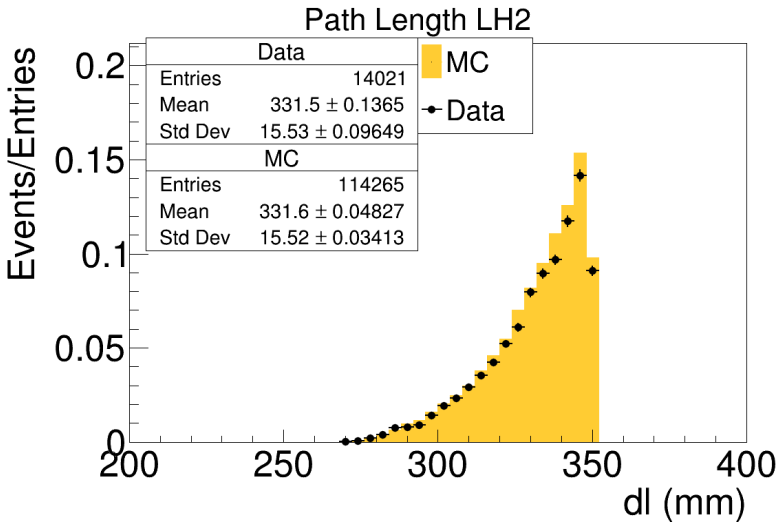

Figure 4.6: Projected path-length through liquid-H_2, mid-p beam.

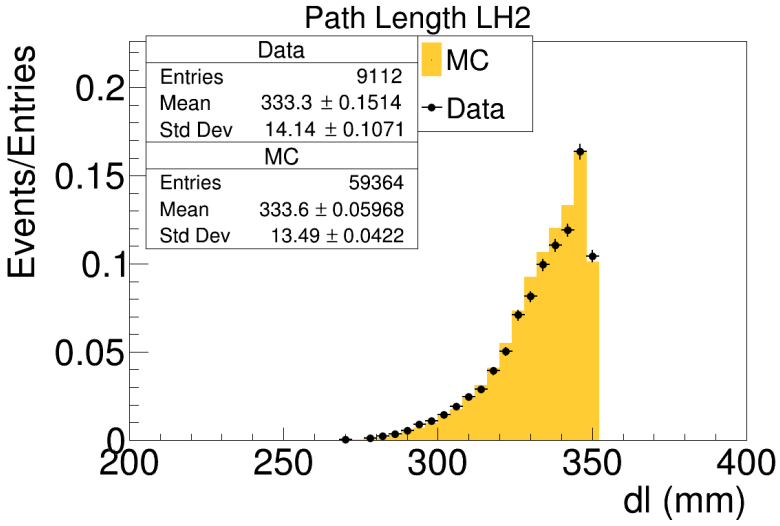

Figure 4.7: Projected path-length through liquid-H_2, high-p beam.

4.2.3 Statistical weighting of MC based on momentum

Momentum is inversely proportional to the width of the Gaussian approximation of the scattering angle (expression 3.28). To be able to compare MCS in simulation and experimental data, it is important to have beam momenta that are similar, if not identical. The energy of the secondary particles reaching MICE was dependent on the energy of the proton beam striking the target, the physics processes that took place within the target and finally the configurations of the beamline magnets in terms of the generated magnetic fields and physical placement. These could also affect the ratios of particle species that reached the MICE lattice. The initial MC beam was generated by G4Beamline, which was configured to provide beams similar to those of the experimental runs. However, differences were observed between simulation and experiment in the beam composition and the measured momentum. An attempt was made to assess the issue by gradually altering the currents of the dipole magnets D_1 and D_2 in multiple steps, in a range within ±10% of the values recorded for the experimental run-numbers used in this analysis. Additionally, the decay solenoid was offset by ±10 mm in each vertical direction and rotated within 1° in each vertical plane in multiple steps. The aim of this was to deduce if one of the G4Beamline parameters was different from the value recorded during data-taking, however the study was inconclusive. For this analysis however, only the particles within the TOF selection range were of interest, hence simulated events generated during this process that were within the selected TOF-range were statistically weighted to match the momenta distributions of the reconstructed data. Initially, the TOF bins (0.1 ns width) were converted to momentum through the process described in section 4.4. Then the distributions were normalised to unity and the weights were calculated with $w_i = n_i(\mathrm{Data})/n_i(\mathrm{MC})$ where i is the bin number and n is the bin content. The resulting weights can be seen overlaid on the Data and MC distributions in figure-block 4.8. They were applied on an event-by-event level to all MC distributions of the selected sample.

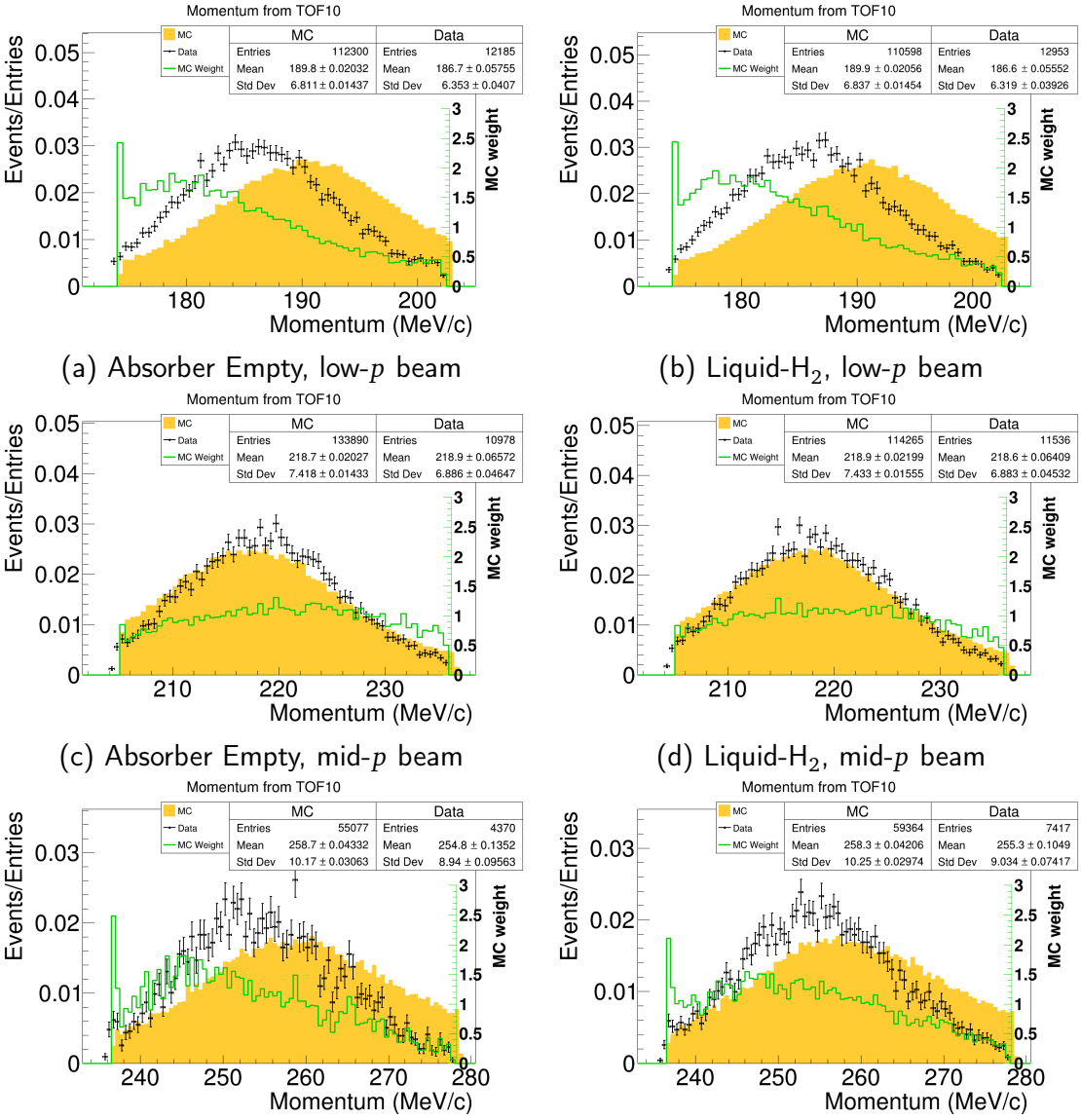

(a) Absorber Empty, low-p beam

(b) Liquid-H_2, low-p beam

(c) Absorber Empty, mid-p beam

(d) Liquid-H_2, mid-p beam

(e) Absorber Empty, high-p beam

(f) Liquid-H_2, high-p beam

Figure 4.8: TOF distribution of MC and data after selection. The ratio of bin contents (data/MC) are used to calculate the statistical weights, shown by the green distribution, that are applied in an event-by-event basis to all MC distributions after TOF selection.

4.3 Tracker alignment

This section describes the method used to correct for the alignment of the trackers within the scope of this analysis. The two scintillating-fibre trackers were positioned within the bore of the superconducting solenoid magnets with a 4 T magnetic-field, which although were not operational for the run-numbers analysed in this study, they were used for data-taking in the solenoid and flip-mode intermittently during the same periods. In solenoid-mode the two (US and DS) spectrometer solenoid magnets had aligned polarities and in flip-mode, reverse polarities. The magnets were placed within meters of each other, and also close to a large iron magnetic yoke, where significant forces could be exerted on even weakly magnetic elements, or non-magnetic elements through their mountings. These had the potential to cause small-scale changes to the relative tracker alignment throughout the running period. These variations may have not been precisely caught by the surveys — partly because the trackers were always within the solenoids, and only 'seen' indirectly.

Without significant macroscopic electromagnetic fields, it is clear that MCS is a symmetric phenomenon. To allow for comparison of the simulated and experimental scattering distributions, and to account for the alignment of the trackers, it was made a requirement that the mean scattering angle (in both planes) should be zero, within the uncertainties of the measurement. This meant that the mean residuals dx/dz and dy/dz of the US and DS tracks should also be consistent with zero. This principle was used to find the two rotation angles (around the x and y-axis) for the US tracks that satisfied this symmetry.

Tracks reconstructed by the US tracker were rotated around the x and y-axis between -7 and 7 mrad in 2 mrad steps using the Euler-Rodrigues formula. The (normalised) unit vector

Data-set	dx/dz (mrad)	dy/dz (mrad)
Empty, low-p	3.86±0.08	-1.89±0.06
LH_2, low-p	4.29±0.001	-2.59±0.1
Empty, mid-p	3.08±0.06	-1.14±0.05
LH_2, mid-p	3.5±0.08	-1.79±0.07
Empty, high-p	3.54±0.07	-1.67±0.06
LH_2, high-p	3.27±0.07	-1.60±0.06

Table 4.4: The rotation angles used to account for the relative tracker-alignment.

$$\widehat{a} = \frac{[dx/dz, dy/dz, 1]}{\sqrt{(dx/dz)^2 + (dy/dz))^2 + 1}} \tag{4.1}$$

was rotated around the $\vec{x} = [1,0,0]$ or $\vec{y} = [0,1,0]$ experimental axis by an angle θ using the four Euler parameters a, b, c and d in the rotation matrix: $\vec{a'} = R\vec{a}$, with the rotation matrix described below:

$$R = \begin{bmatrix} a^2+b^2-c^2-d^2 & 2(bc-ad) & 2(bd+ac) \\ 2(bc+ad) & a^2+c^2-b^2-d^2 & 2(cd-ab) \\ 2(bd-ac) & 2(cd+ab) & a^2+d^2-b^2-c^2 \end{bmatrix} \tag{4.2}$$

such that $a^2+b^2+c^2+d^2 = 1$. The mean residual $\left\langle \frac{dx}{dz}_{US} - \frac{dx}{dz}_{DS} \right\rangle$ enhanced by a factor of 100 for each rotated beam that passed the selection criteria are plotted in figure-blocks 4.9-4.12 as a function of the rotation angle. In the same graphs, the RMS enhanced by a factor of 10 and skewness of the scattering distributions are plotted and examined for any possible systematic effects that modify the scattering distribution, related to the alignment procedure. To obtain the required angle of rotation, the mean residuals were fitted with a straight line and evaluated at the zero residual point. The results are shown in table 4.4.

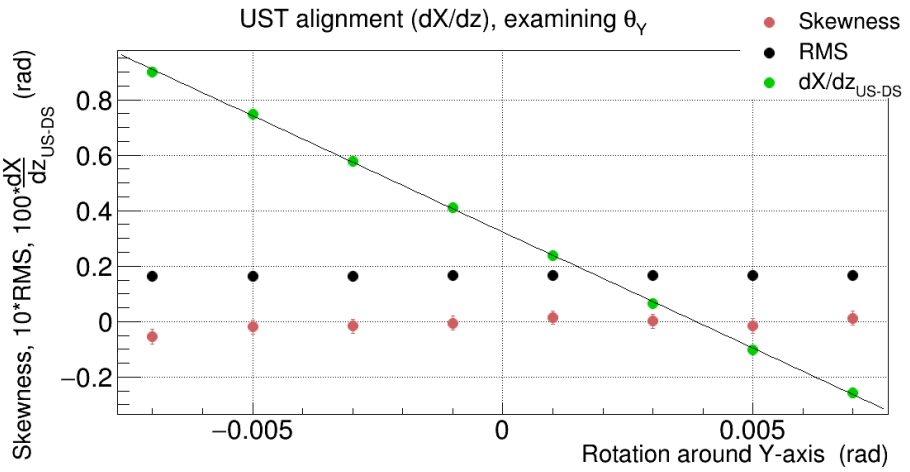

(a) Absorber Empty, low-p beam

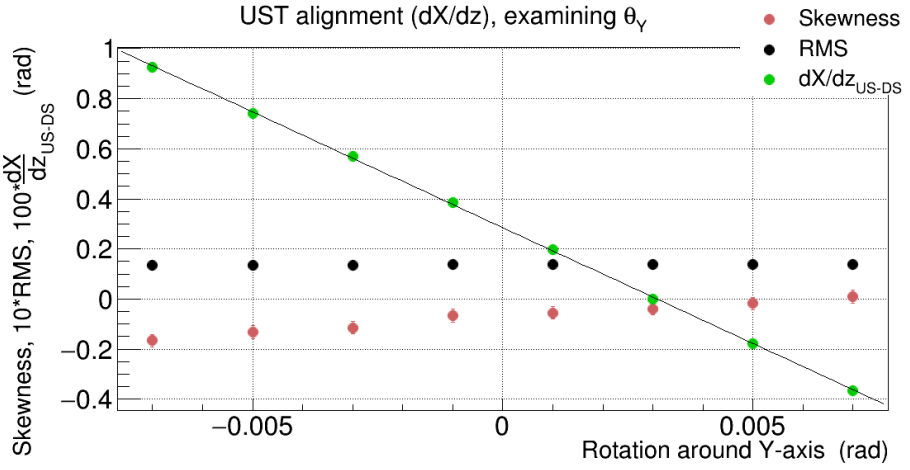

(b) Absorber Empty, mid-p beam

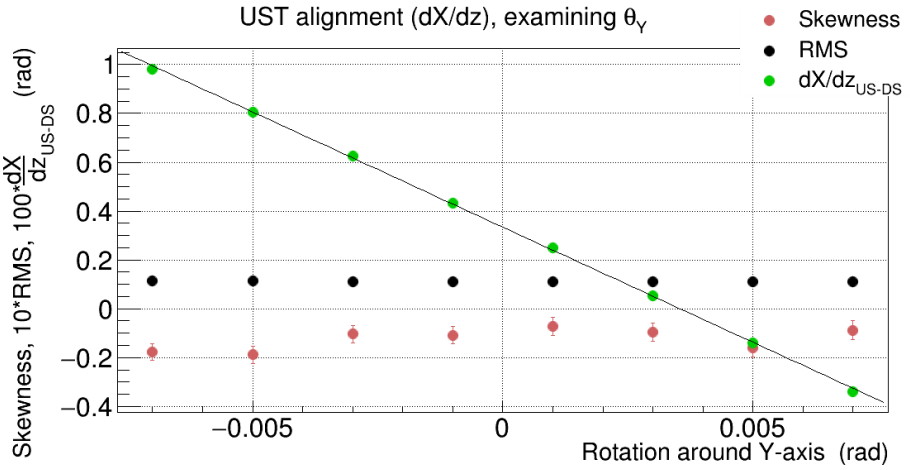

(c) Absorber Empty, high-p beam

Figure 4.9: Tracker alignment for empty-vessel data. Rotations around the y-axis.

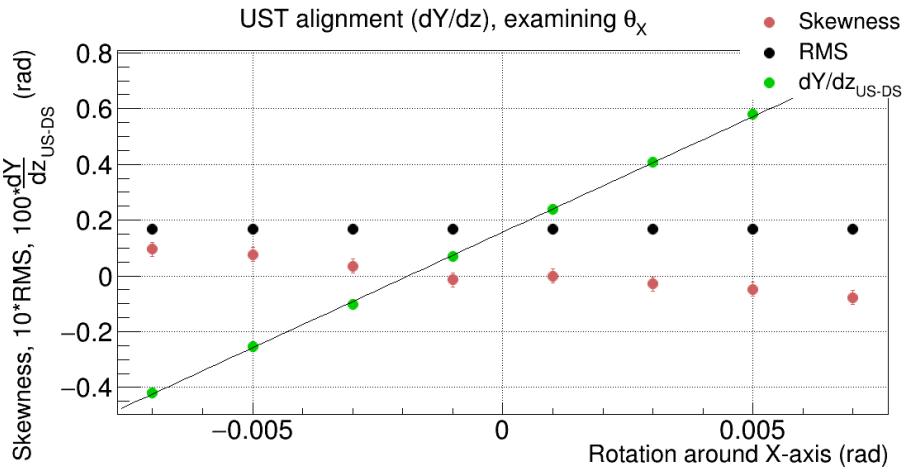

(a) Absorber Empty, low-p beam

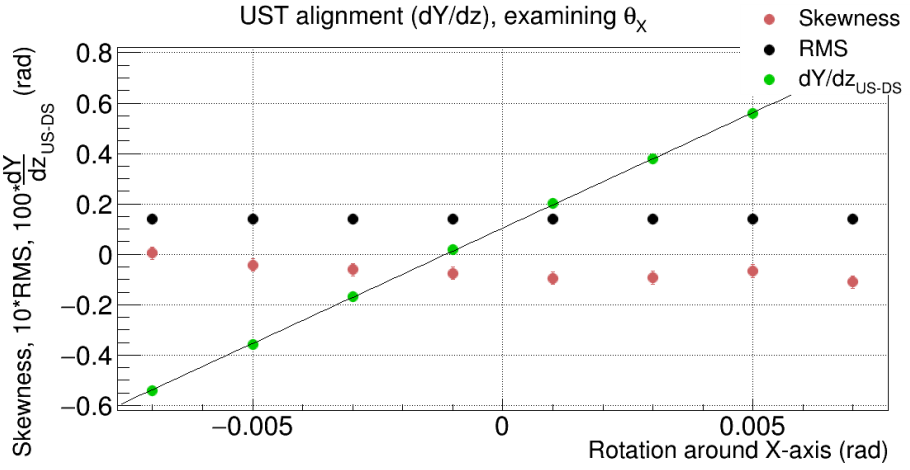

(b) Absorber Empty, mid-p beam

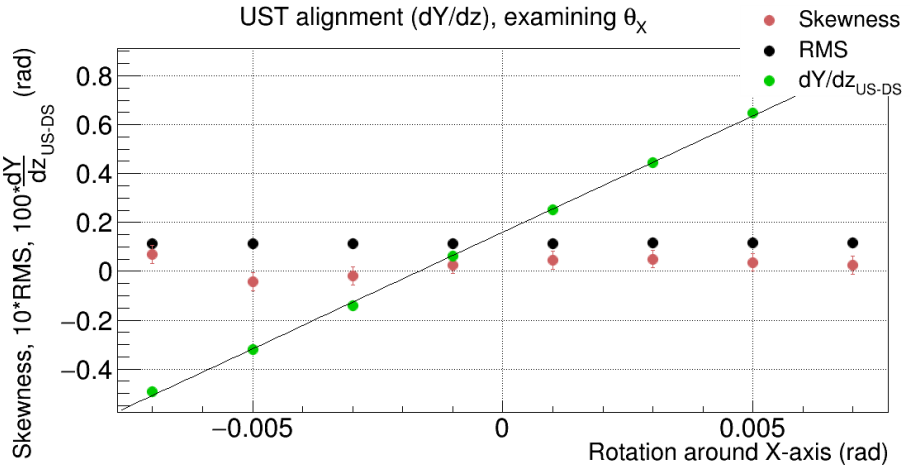

(c) Absorber Empty, high-p beam

Figure 4.10: Tracker alignment for empty-vessel data. Rotations around the x-axis.

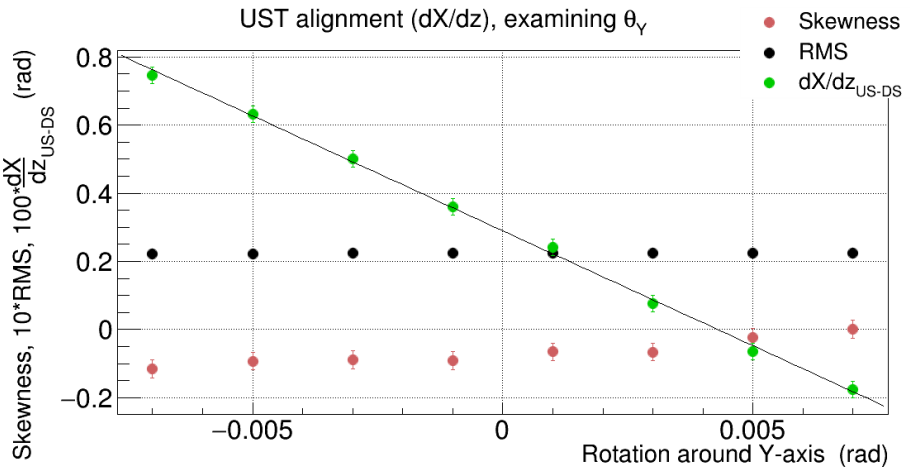

(a) Liquid-H_2, low-p beam

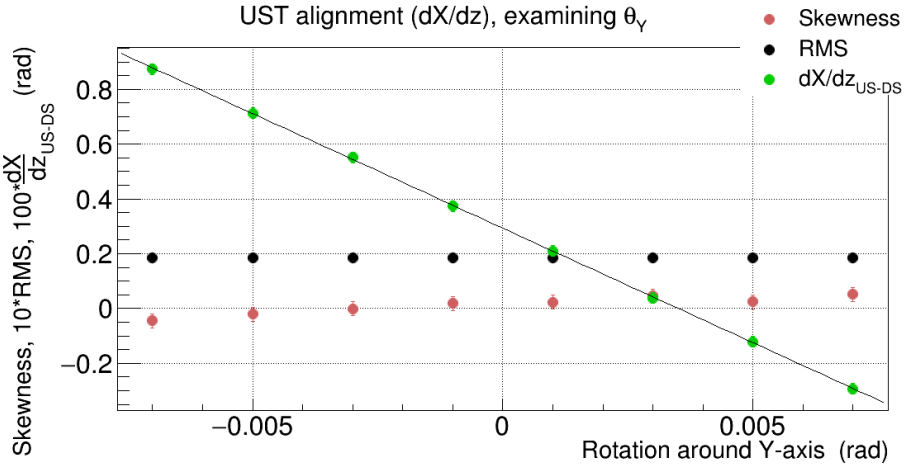

(b) Liquid-H_2, mid-p beam

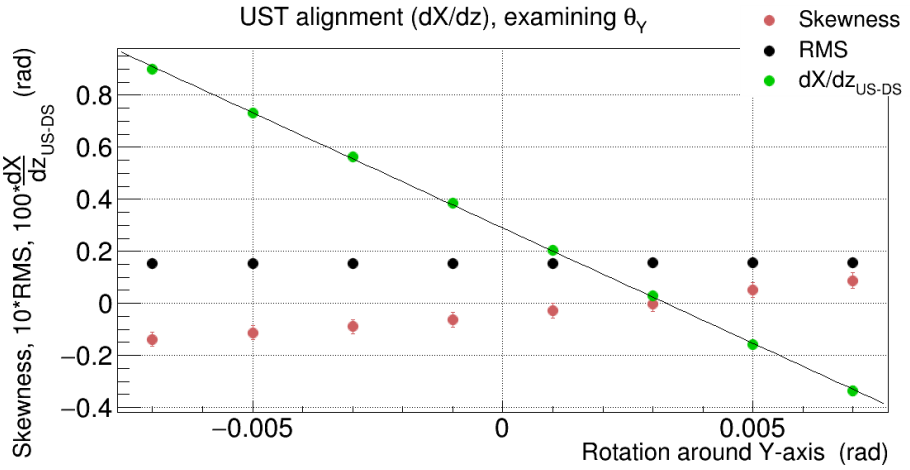

(c) Liquid-H_2, high-p beam

Figure 4.11: Tracker alignment for full-vessel data. Rotations around the y-axis.

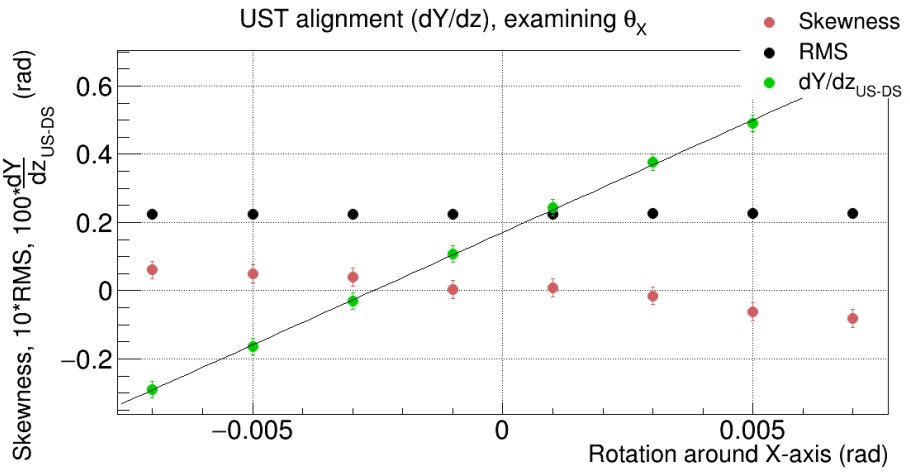

(a) Liquid-H_2, low-p beam

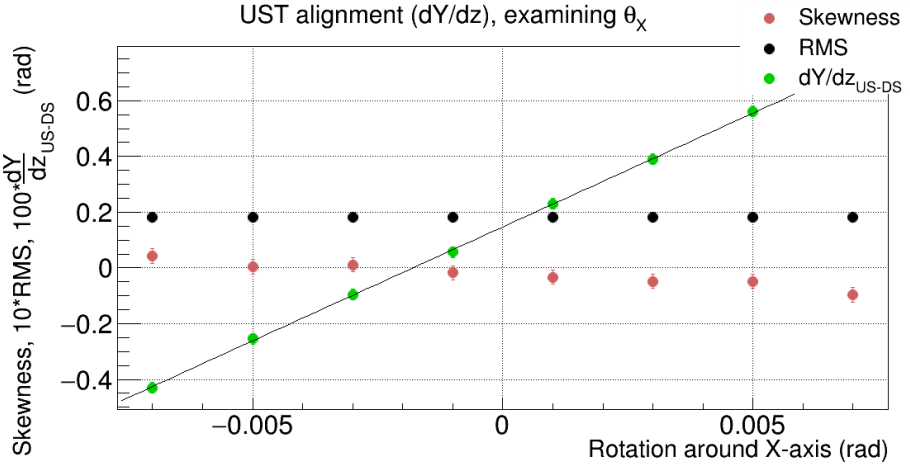

(b) Liquid-H_2, mid-p beam

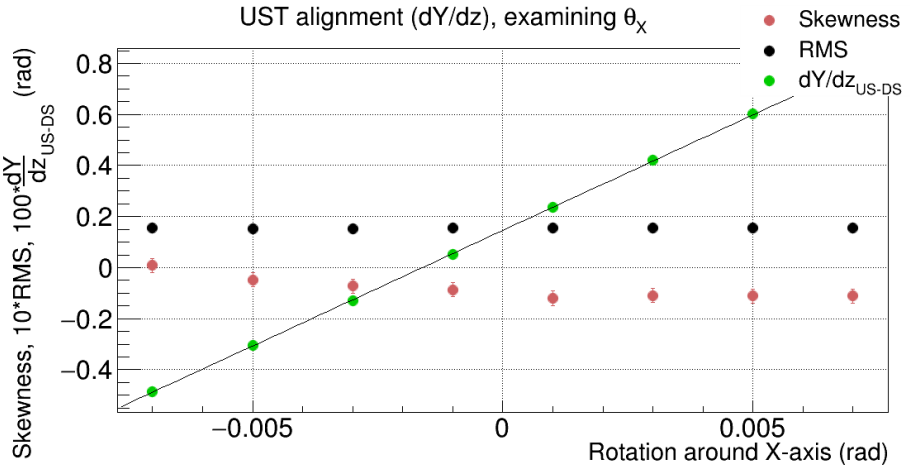

(c) Liquid-H_2, high-p beam

Figure 4.12: Tracker alignment for full-vessel data. Rotations around the x-axis.

4.4 Final sample - Calculation of momentum

MCS is a momentum dependent phenomenon and the assessment of the accuracy of the simulation would be incomplete without having precise knowledge of the measured particle momenta at the point of interaction with the absorber. In MICE, the momentum measurement for cooling studies was measured precisely in the spectrometer solenoids when the active areas were immersed in magnetic fields. The reconstructed particle gyroradius used with the TOF1-TOF0 velocity measurement could both provide particle identity and accurate momentum measurement. For the field-off, straight-track runs studied for MCS, a particle species hypothesis[1] and a velocity measurement from the TOFs were used to calculate particle momentum.

TOF0 was placed directly upstream of the Cherenkov threshold counters and TOF1 was placed 7.64 m downstream. TOF2 was placed so that TOF1 and TOF2 are (nearly) equidistant from the absorber. Therefore, the most relevant velocity measurement was performed using TOF1 and TOF2. The ratio of particles that generated a time-stamp on all three detectors against those that missed TOF2 ranged between 0.81 for the lowest momentum, full-absorber case and 0.93 for the highest momentum, empty absorber case. Limiting the measurement only to those particles that reached and generated a signal at TOF2 would exclude particles for which the scattering angle was too extreme to cross TOF2. Consequently, the TOF0-TOF1 traversal time (figure-block 4.4) was used to calculate velocity, and hence momentum several meters upstream of the absorber, at the TOF1-TOF0 midpoint that was then extrapolated to the centre of the absorber.

The average momentum across this distance was equal to the instantaneous momentum of the particle (p_i) at a point close to the midpoint of the measurement distance. This is calculated with the expression:

[1] The contamination of the selected muon sample by pions and decay electrons was assessed to be less than 0.1% by the simulation.

$$p_i = \gamma_i \beta_i m_\mu = \frac{\beta_i m_\mu}{\sqrt{1-\beta_i^2}} \tag{4.3}$$

where $\beta_i = t_e/t_i$, with t_i the particle time-of-flight and m_μ the muon mass. The average (per run-number) electron time-of-flight (t_e) registered by the relevant pair of TOF detectors was used to approximate the time-of-flight for the speed of light. With that method, the effect of any differing signal latencies in simulation and experimental data was negated.

For particles that registered a TOF2 hit, the momentum was calculated using the above method and the available TOF1-TOF2 transit time. For those that did not register a TOF2 hit, the expected momentum loss across the traversed materials (with properties included in table 4.5) between the midpoint of TOF0-TOF1 and the centre of the absorber was calculated using equation 3.18. The calculation included the path-length through liquid-H_2 from the upstream point-of-intersection with the absorber window to the vessel centre and the aluminium of the upstream vacuum and absorber windows. The latter was calculated by associating the radius of intersection with each window to the aluminium thickness seen in figure 2.8 through fitted parametric equations.

Figures 4.13, 4.14, 4.15 and 4.16 show a momentum comparison of muons that have passed all selection criteria and have also registered space-points in all TOF detectors, allowing for validation of the method. Figure-block 4.17 includes both direct and indirect measurements of momentum. The mean of the momentum distributions of data and simulation agree to within 1,8 MeV/c, with the simulation being consistently higher than the experiment. A likely cause of this is the uncertainty of the amount of glue present within the scintillating-fibre stations of the two trackers. The largest offset is seen in the highest momentum setting (sub-figures 4.17e, 4.17f) for which the least amount of data was available, therefore this is can be attributed to the increased statistical uncertainty. The effect of momentum divergence between the simulated and measured samples to the

Material	Air	Pol.	Al	He	LH_2
I (eV)	85.7e-6	64.7e-6	166e-6	41.6e-6	21.8e-6
Z	0.49	0.54141	13	2	1
A ($\mathrm{g\,mol^{-1}}$)	1	1	26.981	4.002	1.008
R ($\mathrm{g\,mol^{-3}}$)	1.205e-3	1.032	2.7	1.663e-4	0.0708
$\hbar\omega_p$ (eV)	0.71e-6	21.54e-6	32.86e-6	0.26e-6	7.64e-6
x_0	1.7418	0.1647	0.170	2.201	0.44
x_1	4.275	2.503	3.012	3.61	1.885
$\overline{C}$	10.596	3.299	4.239	11.139	3.097
α	0.109	0.164	0.08	0.134	0.134
k	3.399	3.222	3.634	5.834	5.624
X_0 ($\mathrm{g\,cm^{-2}}$)	36.62	43.9	24.01	65.19	63.014

Table 4.5: Table showing the lattice element properties used to calculate energy loss. I is the mean excitation energy, Z the atomic number, A the atomic mass, X_0 the radiation length, R the density, $\hbar\omega_p$ the plasma energy. x_0, x_1, k, $\overline{C}$ and α are the dimensionless Sternheimer parameters [73], referenced from [72].

scattering distributions are assessed in section 4.5.

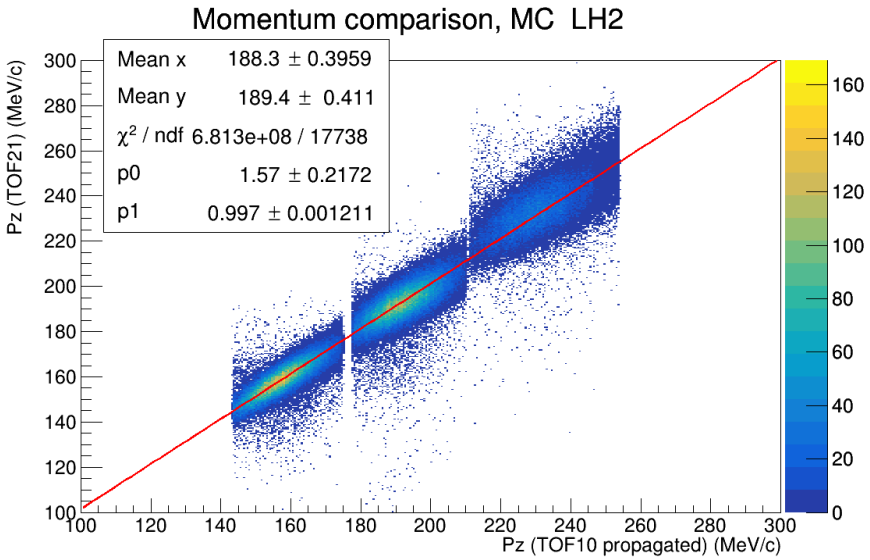

Figure 4.13: MC simulation of the full-absorber configuration, comparison of propagated and measured momentum. The x-axis corresponds to momenta calculated from the TOF1-TOF0 velocity and propagated to the centre of the absorber. The y-axis corresponds to momenta calculated with measurements of TOF2-TOF1 velocity. The fit parameters p0 and p1 are the constant and gradient parameters of the straight line fit.

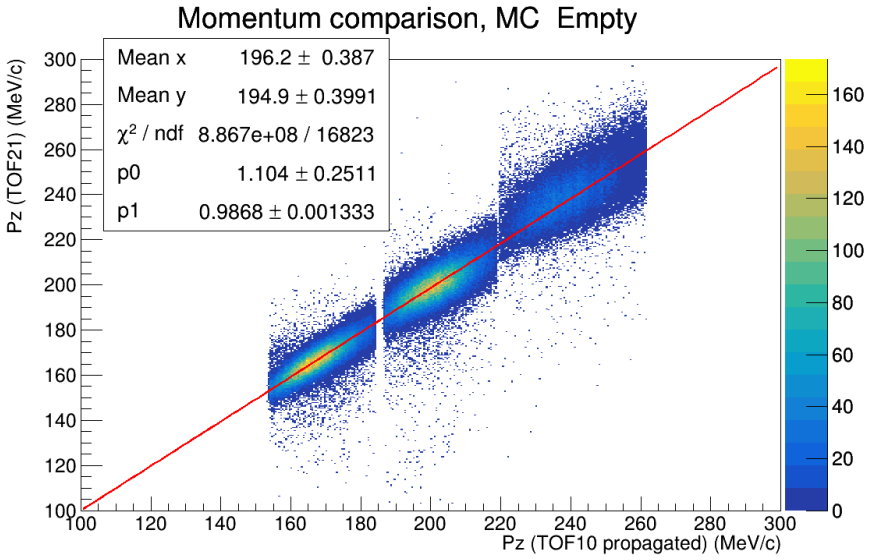

Figure 4.14: As figure 4.13 MC simulation of the empty absorber configuration.

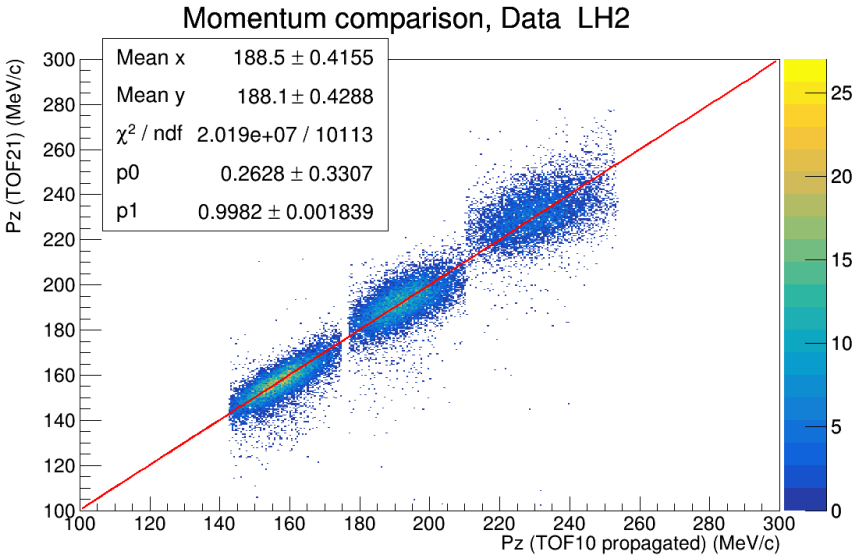

Figure 4.15: As figure 4.13 experimental data from the full-absorber configuration.

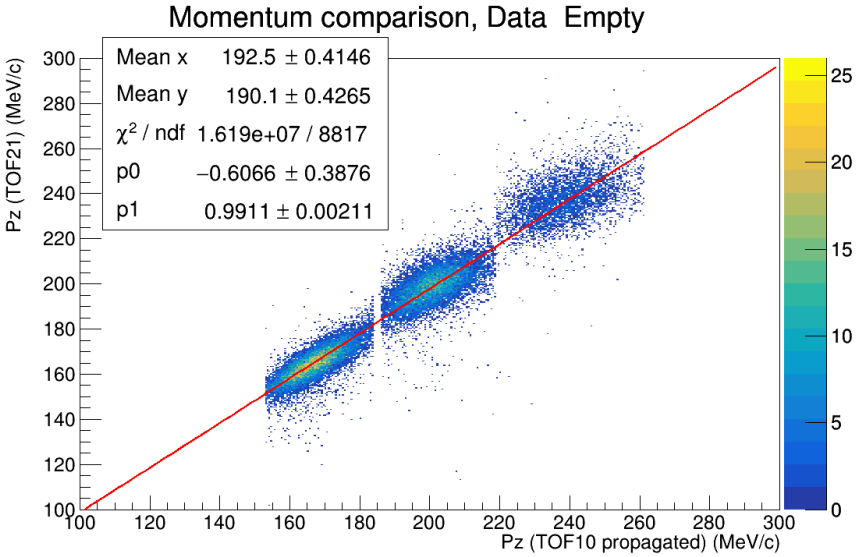

Figure 4.16: As figure 4.13 experimental data from the empty absorber configuration.

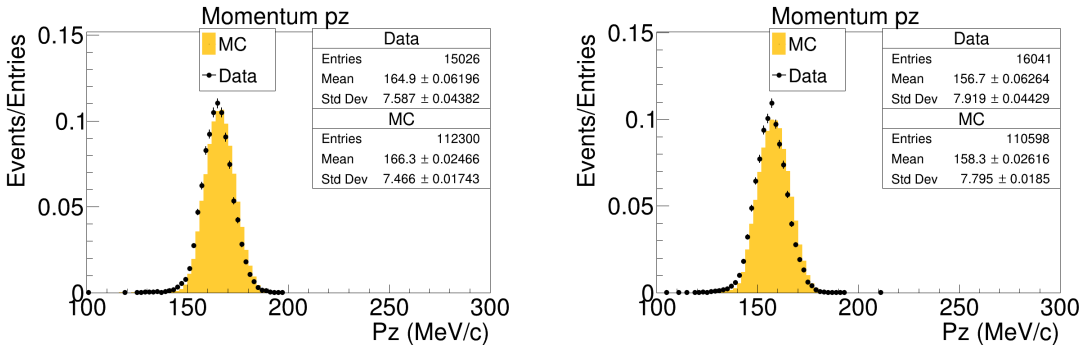

(a) Absorber Empty, low-p beam

(b) Liquid-H_2, low-p beam

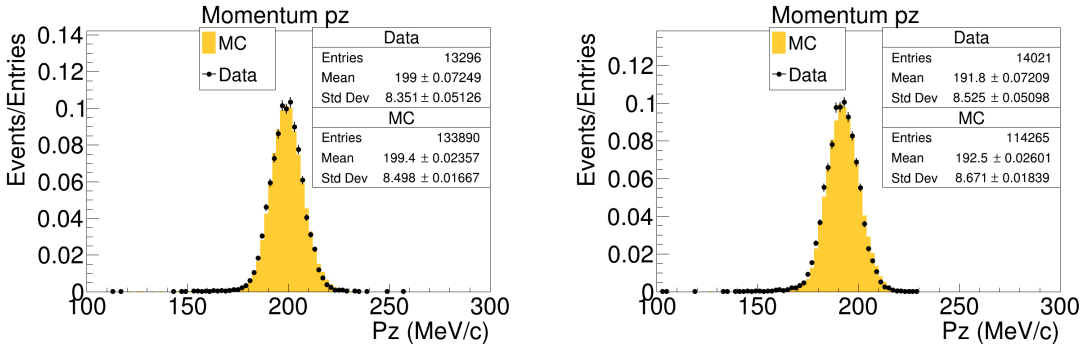

(c) Absorber Empty, mid-p beam

(d) Liquid-H_2, mid-p beam

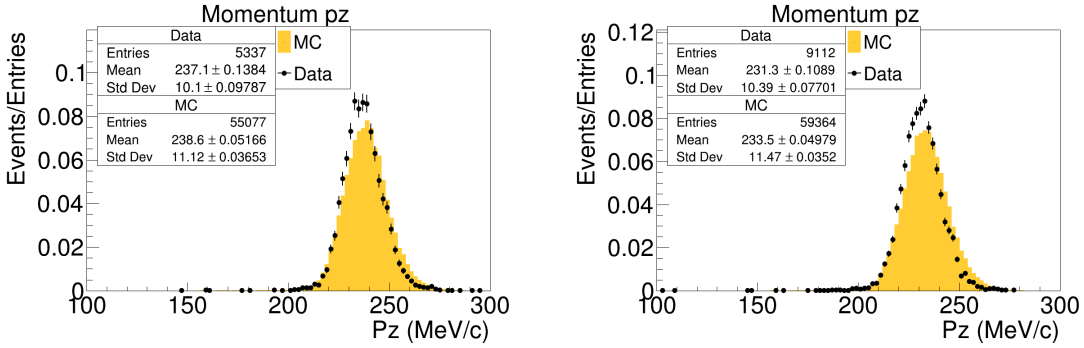

(e) Absorber Empty, high-p beam

(f) Liquid-H_2, high-p beam

Figure 4.17: Calculated momenta for particles that have passed all selection criteria.

4.4.1 Z-position of reconstructed momentum

Particle velocity between any pair of TOFs was non-symmetric with respect to the point of equal distance. This was due to energy loss occurring within all non-vacuum volumes of the lattice. A consequence of this was that particle velocity in the first half of the distance was higher than the second half. As a result, the measured velocity corresponded to instantaneous particle velocity at a point offset from the geometrical centre. In this analysis however the particle momenta at the centre of the absorber were required. Figures 4.18-4.20 show the p_z true momentum (black markers) as a function of z-position in the vicinity of the absorber for the three MC momenta settings. The true parameters of the particles were not tracked continuously by MAUS but only in pre-defined positions. The z-position of the reconstructed momentum (red marker) was deduced from a straight line fit to the true momentum within the absorber windows. The figures also show the position of the four aluminium windows of the vessel, the point of equal distance between TOF1 and TOF2 and the centre of the absorber.

Given the large momentum-spread of the measured sample and the 0.085 ps uncertainty of the TOF hodoscopes, it was decided that a shift of the measured momentum is unnecessary, since the z-position of the reconstructed momentum already appeared sufficiently close to the centre of the absorber.

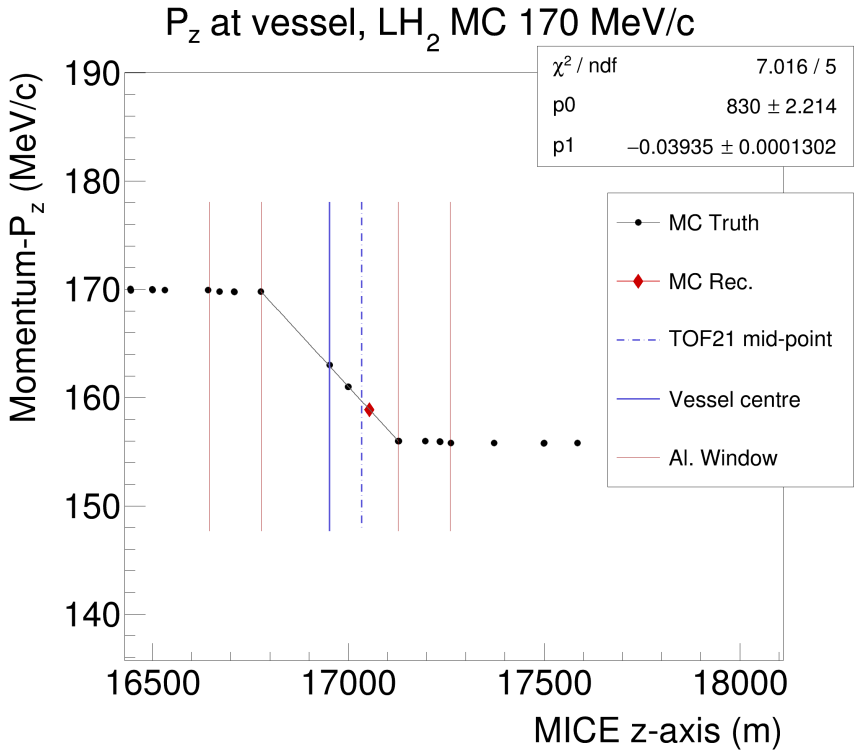

Figure 4.18: True and reconstructed momentum of muons as a function of position in the vicinity of the absorber for the low-p beam, full-absorber.

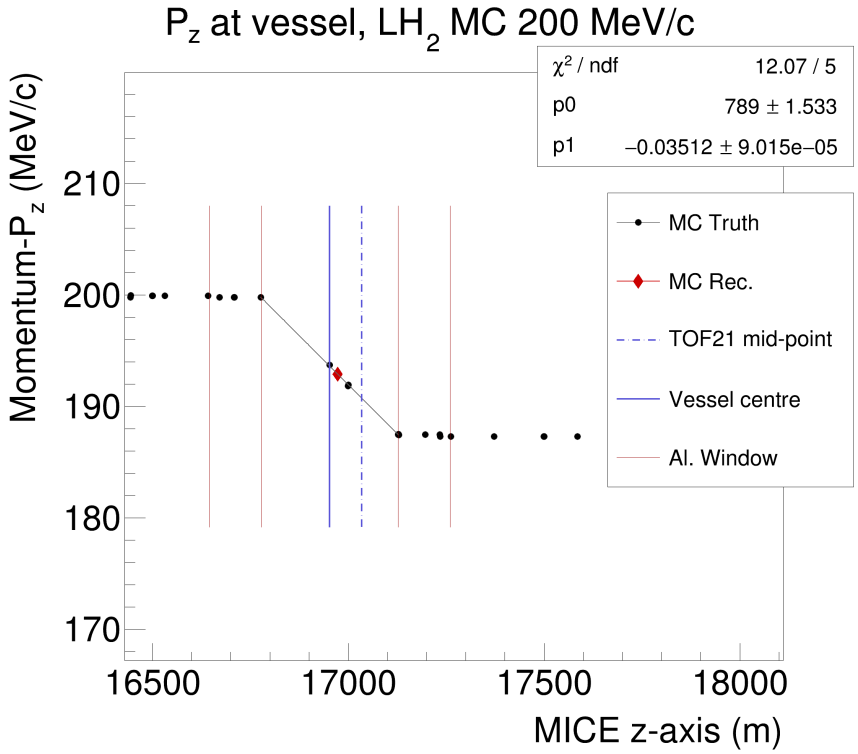

Figure 4.19: True and reconstructed momentum of muons as a function of position in the vicinity of the absorber for the mid-p beam, full-absorber.

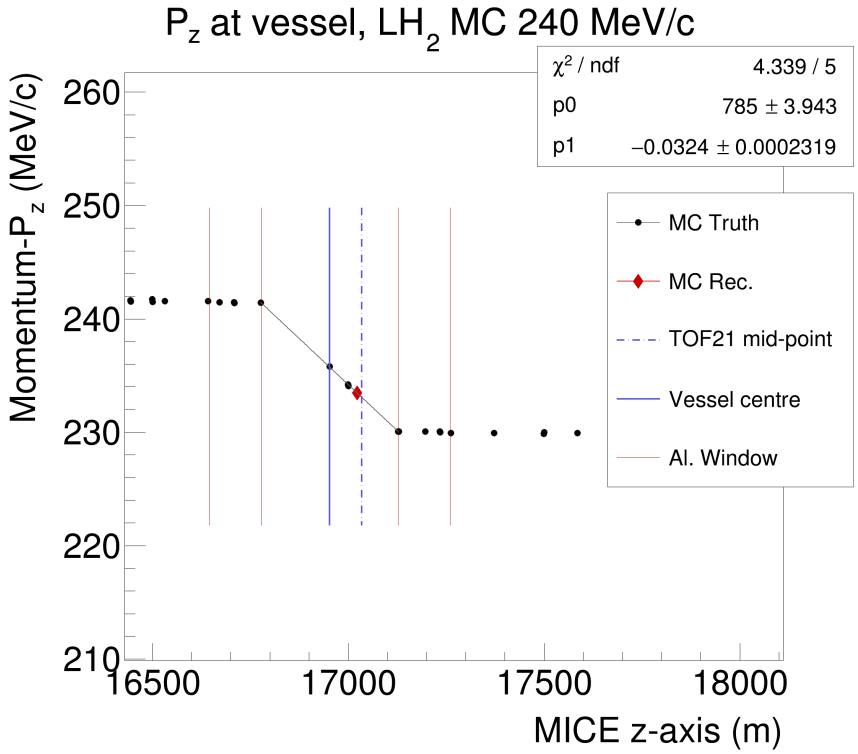

Figure 4.20: True and reconstructed momentum of muons as a function of position in the vicinity of the absorber for the high-p beam, full-absorber.

4.5 Systematic uncertainties

Bin-by-bin systematic uncertainties were calculated for the distributions of projected angles defined by equations 3.32, 3.33 and the 3D scattering angle defined by 3.34. Additionally, the systematic uncertainty to the width of these distributions was calculated. The sources of uncertainty that were considered are listed below:

- TOF resolution;
- Downstream radial selection, at the position of the downstream-most scintillating-fibre station of the final tracker;
- Upstream radial selection, at the position of the diffuser;
- The corrective rotation required for the trackers relative alignment;
- The definitions of θ_x and θ_y.

The MC simulation was used to calculate the uncertainty to the final results due to the momentum resolution. The time-of-flight reconstructed by the TOF1-TOF0 hodoscopes for each particle was shifted in 0.0029 ns steps in a range of -0.09 to +0.09 ns from the measured value. The particular time-envelope was chosen as it was the standard deviation of the residual between true time-of-flight and reconstructed time-of-flight, extracted from the simulation. The statistical weights of subsection 4.2.3 were then applied to the shifted time-of-flight, which resulted in events weighted at different bins than in the unperturbed distribution, mimicking a momentum shift. The analysis was re-run for each step, and the distribution of angles was re-calculated. Correlation of the sources of systematic uncertainty was not expected to have a significant effect to the total uncertainty and was therefore not considered.

The aim of the two radial selections described in subsection 4.2.1 was to reject particles that have crossed diffuser material, which therefore reached the absorber at a lower momentum than those that had passed clear, and to constrain the tracker volume being used in the MCS measurement. The reconstruction efficiency of the trackers was expected to radially vary near the tracker's outer edge. In terms of the scattering distributions, efficiency is the ratio of events reconstructed in an angle interval (bin) over the true number, which is known only in the case of simulation. This was expected to be a very slow variation in the central volume of the trackers, where this analysis was focussed. To account for this effect, the two projected radii used to reject particles were changed in steps of 10 mm in a range of -30 to 30 mm from the central values, the analysis was re-run and the scattering distributions re-calculated for each step.

The alignment correction, described in section 4.3 was applied only to the experimental data. All tracks reconstructed by the upstream tracker were rotated by an angle around the x and an angle around the y-axis to achieve relative angular alignment between the two trackers in both planes. This had a direct impact on the scattering distribution; misaligned trackers would result in a non-zero mean to the scattering distributions. However, the shape of the distribution remained largely unchanged by these rotations, as demonstrated by the small variations of skewness and RMS-width, illustrated by the red and black markers in figure-blocks 4.9-4.12. The rotation angles were deduced by fitting a straight line to the mean upstream-downstream residuals, and evaluating the angle for which these are zero. Each point represents a re-run of the analysis that also contained the scattering distributions for each case, providing the opportunity to calculate the effect of non-perfect alignment to the final result.

The definition of projected angles θ_x and θ_y required a choice of vector. The unit vector $\widehat{y}$ was chosen which is aligned with the y-axis of the MICE coordinates. In principle this could be any other vector lying on the plane perpendicular to the

z-axis. To investigate this choice for systematic effects, $\widehat{y}$ was rotated in 60° steps around the z-axis, completing a full circle. For each of these steps the scattering distributions were re-calculated. For each of these steps the scattering distributions were re-calculated. This resulted in a 0.1-0.07 mrad uncertainty to the scattering widths of the projected angle distributions. The 3D scattering angle was unaffected by this since it is measured in the plane containing both incident and scattered tracks, without an arbitrary choice.

The error of the ith bin of any of the three angle distributions caused by each source of uncertainty was approximated by the formula:

$$\sigma_i = \left| \frac{\Delta n_i}{\Delta r} \right| \sigma_r, \tag{4.4}$$

where r is the parameter being varied. For each bin, the difference in bin content across the r parameter range was linearly approximated by $\frac{\Delta n_i}{\Delta r}$. Table 4.6 summarises the ranges of r and the σ_r's used for these calculations. The σ_r used for the time-of flight is the standard deviation of the residual $dt_{Rec.} - dt_{Truth}$ provided by the MC simulation. For the angle definition, $\pi/2$ was chosen, reflecting the angle between the x or the y-axis, which both could have been valid choices to define the projection planes. For the radial selection, the estimated $\sigma_r = 10$ mm was considered because that is the radial distance between the maximum accepted particle radius (90 mm) at the diffuser and the diffuser annulus, at 100 mm. For the alignment, σ_{fit} was provided by the confidence interval of the straight-line fit. These were calculated per data-set and are in the order of 10^{-2} mrad.

A similar method was used to calculate the systematic uncertainty to the 68% scattering width (one standard deviation) of the three defined scattering angles. The width of the scattering distributions was calculated for each analysis instance with a perturbed analysis parameter r. The reported widths of projected angle distributions, θ_x and θ_y, are the σ parameters of Gaussian fits performed by ROOT, in order to have compatible widths with those provided by the Gaussian MCS ap-

Source of unc.	r range	σ_r
$\widehat{y}$ rotation (rad)	0–2π	$\pi/2$
Alignment (rad)	-0.007–0.007	σ_{fit}
DS radial (mm)	70–130	10
TOF10 (ns)	dt-0.09–dt+0.09	0.085
US radial (mm)	60–120	10

Table 4.6: Table of considered sources of uncertainty. Each is investigated by varying a parameter r across a range given range of the second column. The σ_r for each is the effective range used in equation 4.4.

proximation of equation 3.28. For the 3D scattering angle θ_s, the calculated width corresponds to the square root of the second moment of the binned distribution around the mean (variance). The resulting uncertainty, similar to the bin-by-bin calculation is

$$\sigma_\theta = \left| \frac{\Delta\sigma_\theta}{\Delta r} \right| \sigma_r. \tag{4.5}$$

The total calculated systematic uncertainty for all scattering angles, and both bin error and scattering widths is the square root of the square sum of each systematic contribution. These are reported in table 4.7 for the empty-absorber data-sets and in table 4.8 for the full vessel.

Source of unc.	θ_x (mrad)	θ_y (mrad)	θ_s (mrad)
164.9±7.58 MeV/c muon momentum			
$\widehat{y}$-rotation	0.07	0.03	0.0
Alignment	<0.01	<0.01	<0.01
DS radial	0.08	0.11	0.02
TOF	0.11	0.07	0.06
US radial	0.07	0.14	0.05
Total sys.	0.17	0.19	0.08
199±8.35 MeV/c muon momentum			
$\widehat{y}$-rotation	0.07	0.08	0.0
Alignment	<0.01	<0.01	<0.01
DS radial	0.14	0.14	0.05
TOF	0.06	0.08	0.04
US radial	0.11	0.08	0.08
Total sys.	0.2	0.19	0.1
237.1±10.1 MeV/c muon momentum			
$\widehat{y}$-rotation	0.1	0.07	0.0
Alignment	<0.01	<0.01	0.01
DS radial	0.16	0.19	0.1
TOF	0.19	0.11	0.07
US radial	0.09	0.07	0.08
Total sys.	0.28	0.25	0.14

Table 4.7: Calculated systematic uncertainties to the scattering widths of θ_x, θ_y and θ_s for the empty-vessel data-set. The total is the quadratic sum of each contribution.

Source of unc.	θ_x (mrad)	θ_y (mrad)	θ_s (mrad)
156.7±7.91 MeV/c muon momentum			
$\widehat{y}$ rotation	0.04	0.06	0.0
Alignment	<0.01	<0.01	<0.01
DS radial	0.03	0.04	0.02
TOF	0.18	0.11	0.05
US radial	0.08	0.08	0.02
Total sys.	0.2	0.15	0.06
191.8±8.52 MeV/c muon momentum			
$\widehat{y}$ rotation	0.07	0.04	0.0
Alignment	<0.01	<0.01	<0.01
DS radial	0.05	0.03	0.01
TOF	0.11	0.1	0.04
US radial	0.08	0.06	0.03
Total sys.	0.16	0.13	0.05
231.3±10.4 MeV/c muon momentum			
$\widehat{y}$ rotation	0.07	0.08	0.0
Alignment	<0.01	<0.01	<0.01
DS radial	0.06	0.06	0.02
TOF	0.13	0.27	0.11
US radial	0.09	0.05	0.05
Total sys.	0.18	0.29	0.12

Table 4.8: Calculated systematic uncertainties to the scattering widths of θ_x, θ_y and θ_s for the liquid-H_2. The total is the quadratic sum of each contribution.

Chapter 5

Results

The principal results of this analysis are the distributions of scattering angles. The aim was to assess if the experimental measurement is closely matched by the Geant4 MCS algorithm with the presence of liquid-H_2 in the beam-path. To benchmark the process, each of the three momentum settings has also been measured and simulated through a lattice that does not contain liquid-H_2 and is otherwise identical. This is assessed on bin-by-bin basis and by comparison of the resulting one-standard-deviation widths of the distributions in section 5.1. Additionally, an expression of the form of equation 3.28 is fitted to the scattering widths in section 5.2, which allows for a momentum-dependent comparison of the scattering widths of the experimental data and MC. The calculated systematic uncertainties have been used in the scattering width tables 5.2 and 5.3, the χ^2/NDF and p-value calculations of table 5.1, and in figures 5.19 and 5.20.

5.1 Scattering angle distributions

Figures 5.1-5.18 show the projected angles for all data-sets, normalised to the number of upstream tracks. This is the number appearing in the statistics box of each histogram. The scattering angle for particles that did not make it to

the downstream tracker was set to a value outside the histogram limits. Consequently, these only affect the number of entries and no other statistical metric. The plots appearing underneath each angle distribution are the residuals of the normalised bin contents. Only statistical errors are shown in the histograms and residuals, reflecting the uncertainty due to the finite sampling of the underlying phenomenon. This is calculated from the variance of the sum of weights (w_i) of a given bin, $\sigma_{bin} = \sqrt{\sum_i w_i^2}$, around zero. Pearson's χ^2-test is used to determine if the differences between same-bin contents between data and simulation are due to chance, the calculation is done with ROOT's internal routines described in [89][1]. The embedded χ^2/NDF and p-values in each plot do not include the influence of systematic uncertainties.

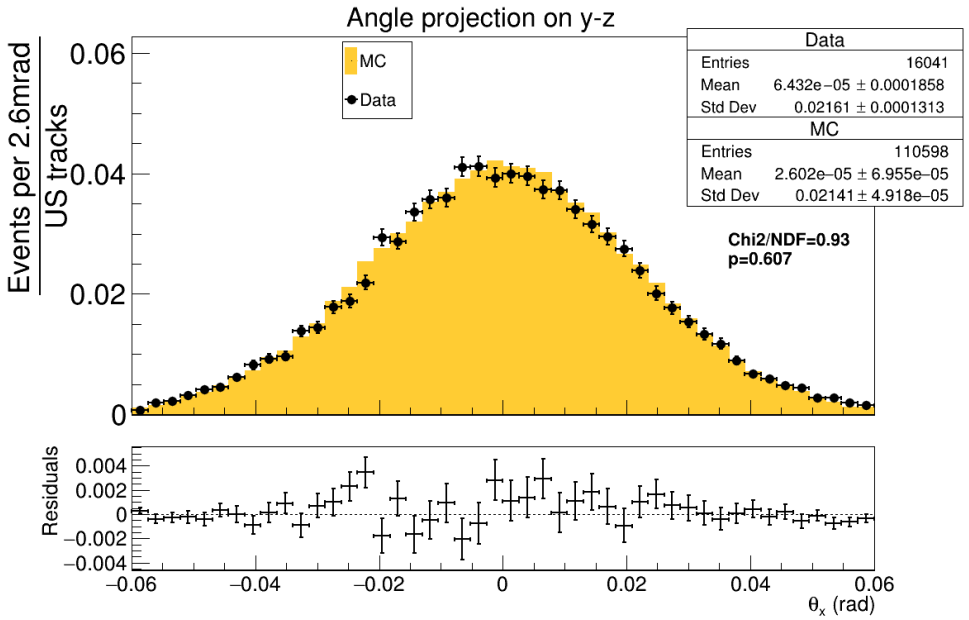

Figure 5.1: θ_x scattering distribution of the low-p muon beam through liquid-H_2 for experimental data and MC simulation.

Table 5.1 shows the χ^2/NDF and p-value calculations including the influence of the systematic uncertainties discussed in section 4.5.

[1] Section 3 of [89]

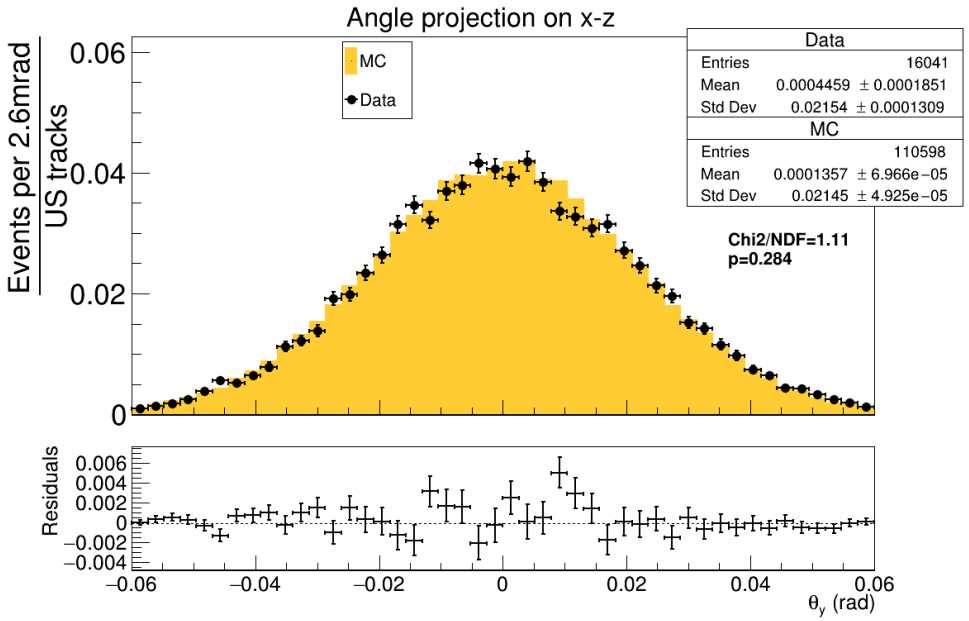

Figure 5.2: θ_y scattering distribution of the low-p muon beam through liquid-H_2 for experimental data and MC simulation.

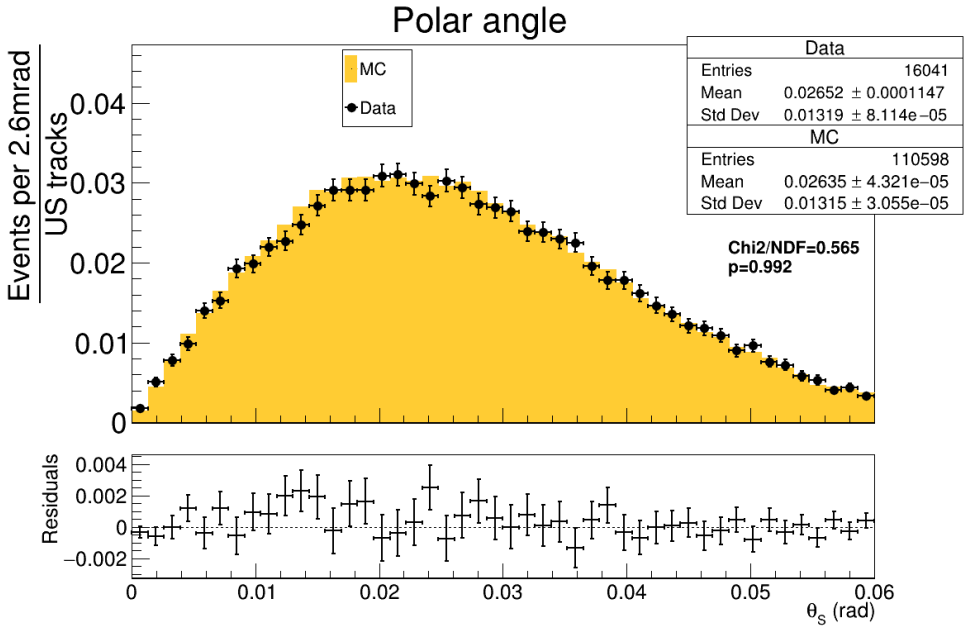

Figure 5.3: 3D scattering angle distribution of the low-p muon beam through liquid-H_2 for experimental data and MC simulation.

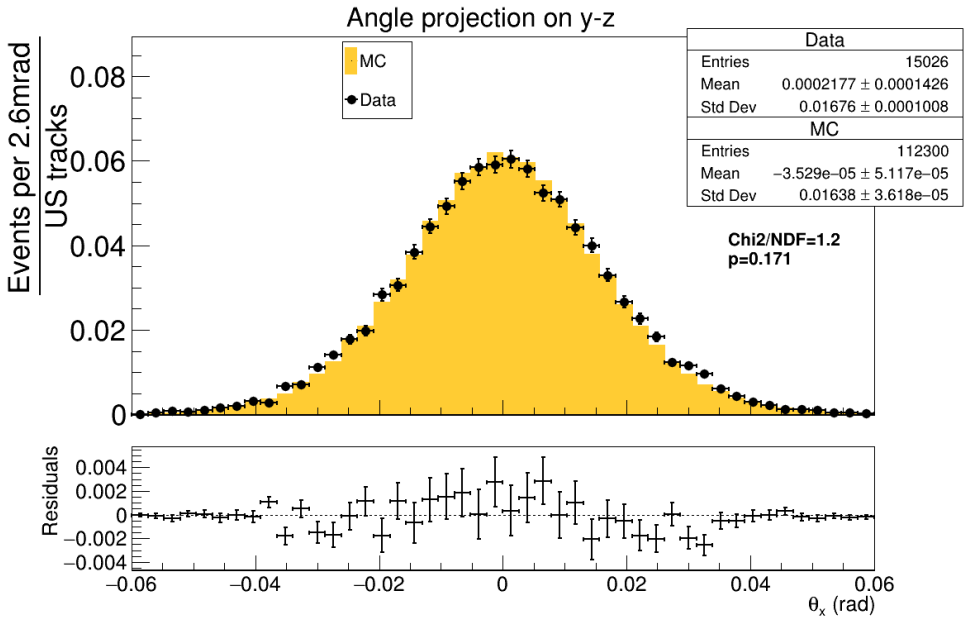

Figure 5.4: θ_x scattering distribution of the low-p muon beam through the empty vessel for experimental data and MC simulation.

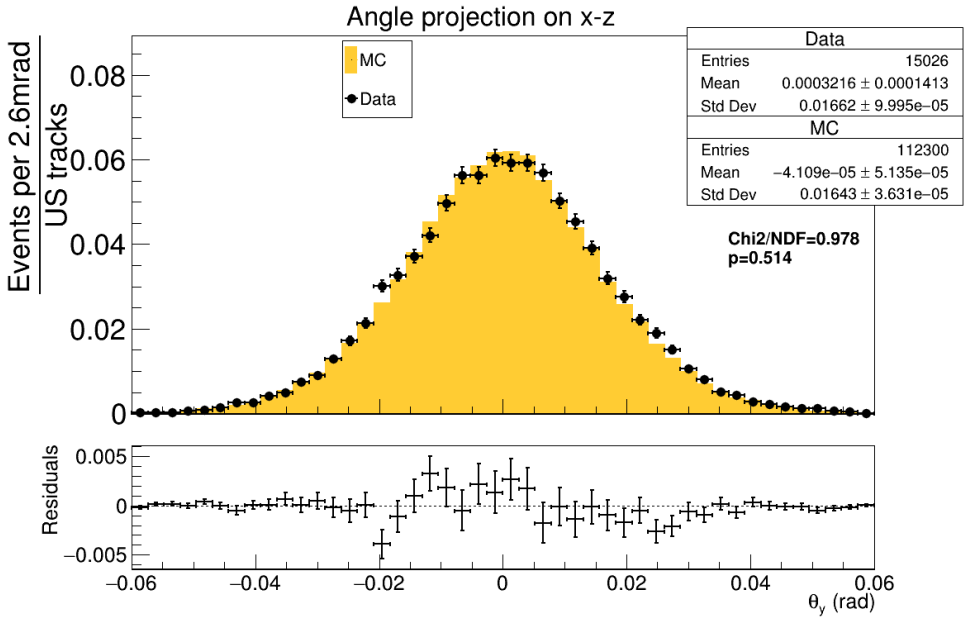

Figure 5.5: θ_y scattering distribution of the low-p muon beam through the empty vessel for experimental data and MC simulation.

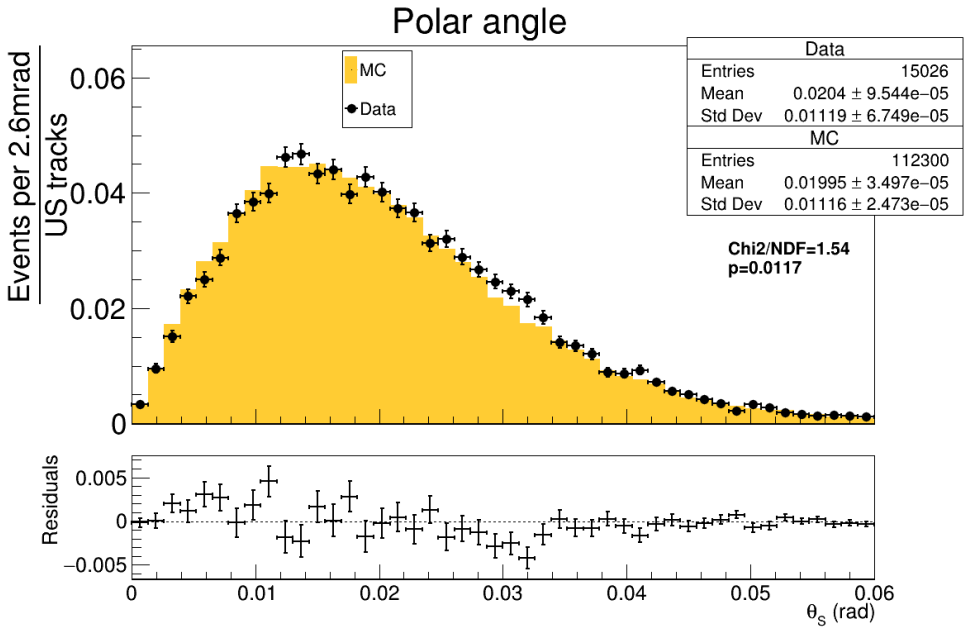

Figure 5.6: 3D scattering angle distribution of the low-p muon beam through the empty vessel for experimental data and MC simulation.

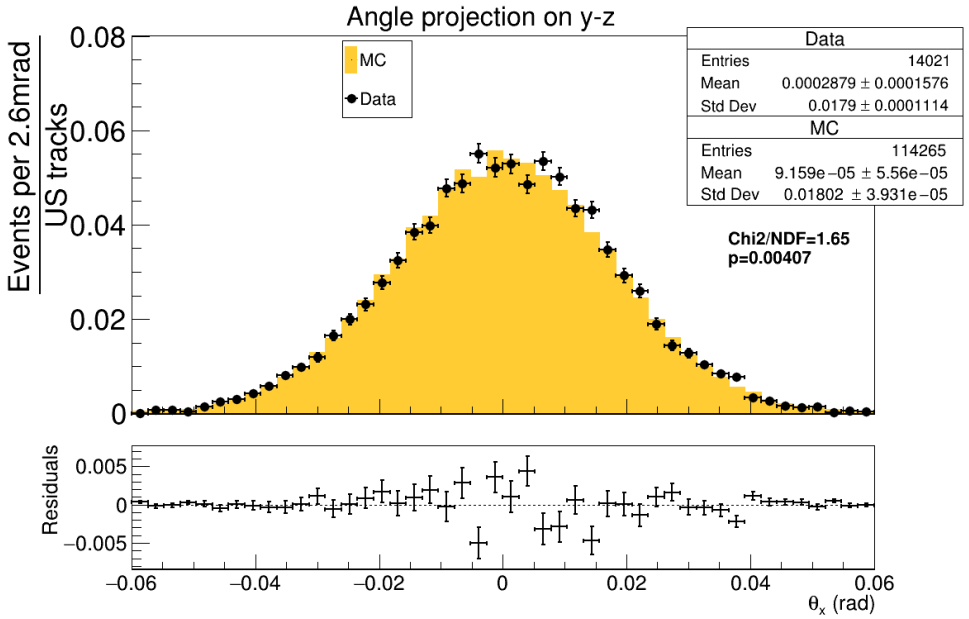

Figure 5.7: θ_x scattering distribution of the mid-p muon beam through liquid-H_2 for experimental data and MC simulation.

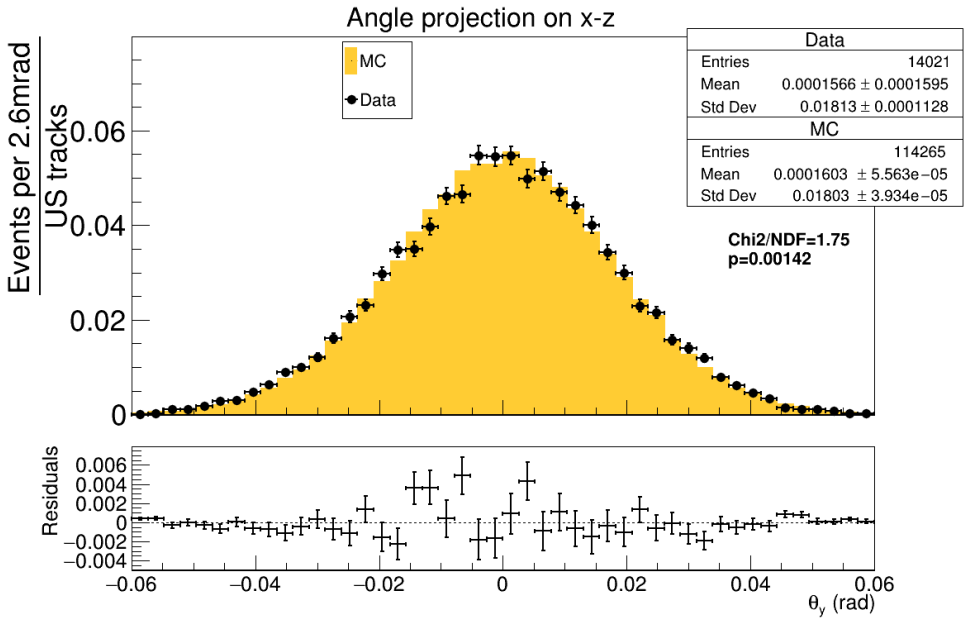

Figure 5.8: θ_y scattering distribution of the mid-p muon beam through liquid-H_2 for experimental data and MC simulation.

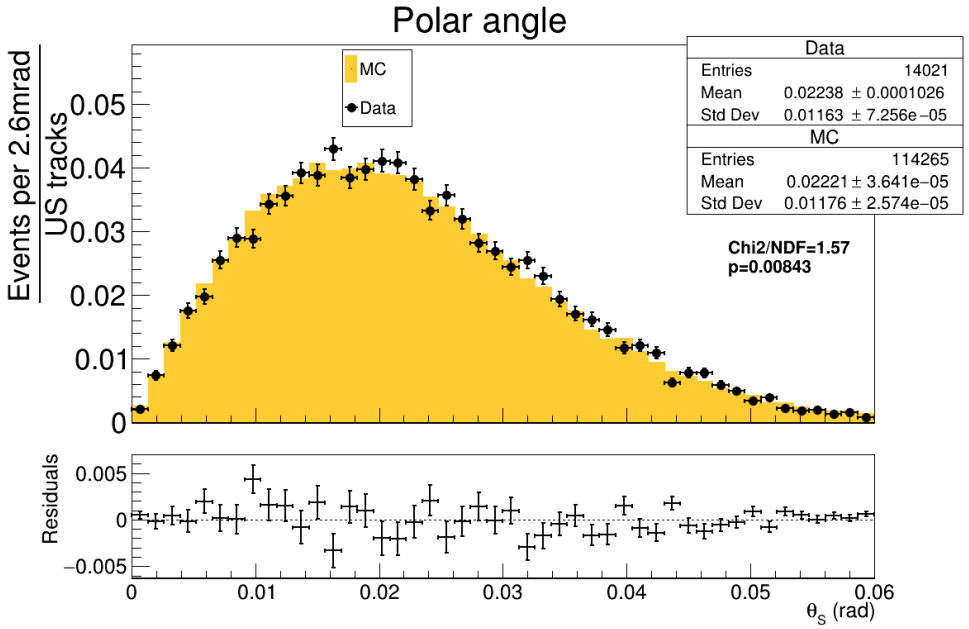

Figure 5.9: 3D scattering angle distribution of the mid-p muon beam through liquid-H_2 for experimental data and MC simulation.

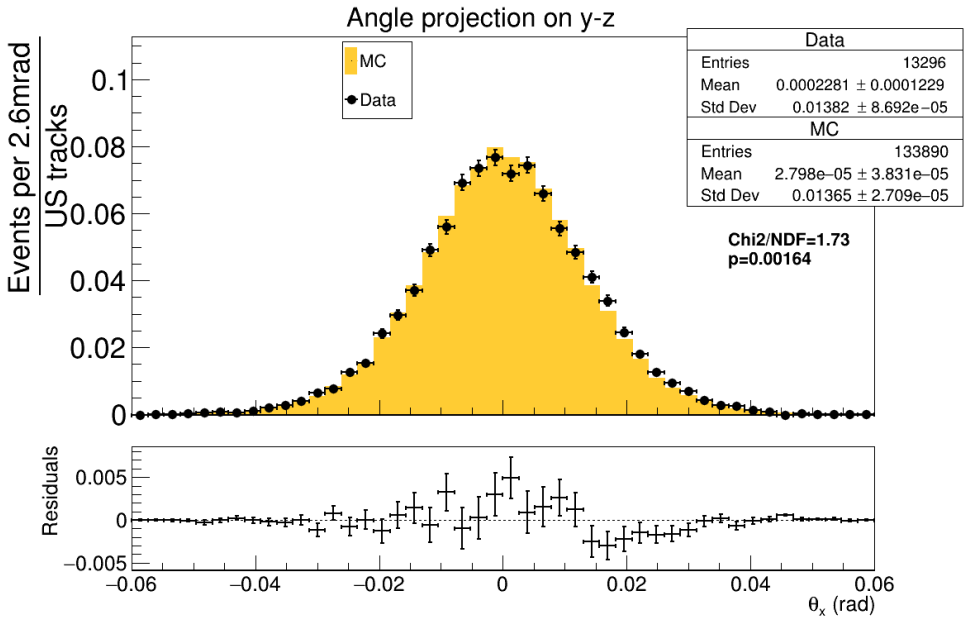

Figure 5.10: θ_x scattering distribution of the mid-p muon beam through the empty vessel for experimental data and MC simulation.

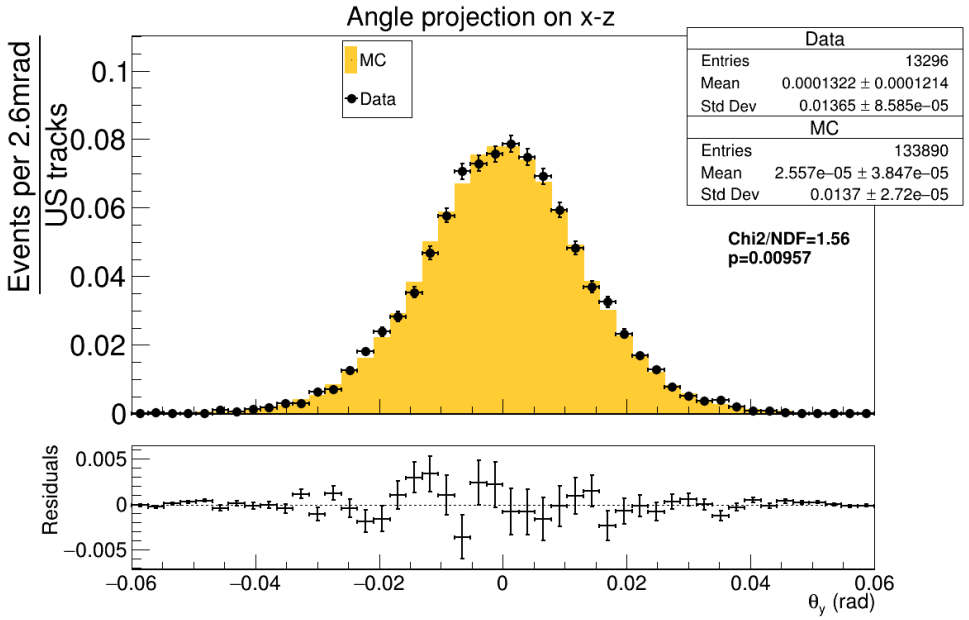

Figure 5.11: θ_y scattering distribution of the mid-p muon beam through the empty vessel for experimental data and MC simulation.

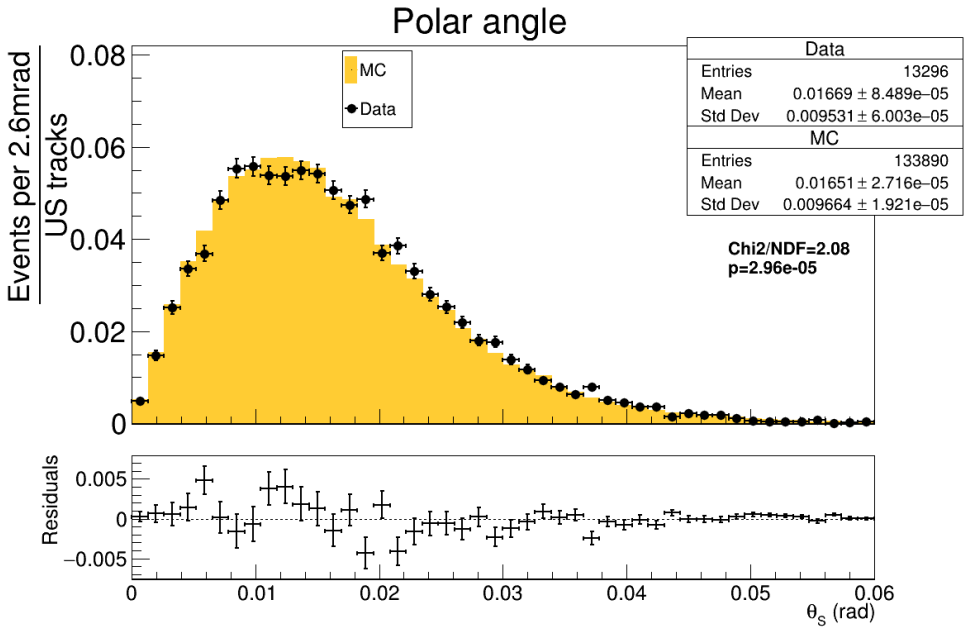

Figure 5.12: 3D scattering angle distribution of the mid-p muon beam through the empty vessel for experimental data and MC simulation.

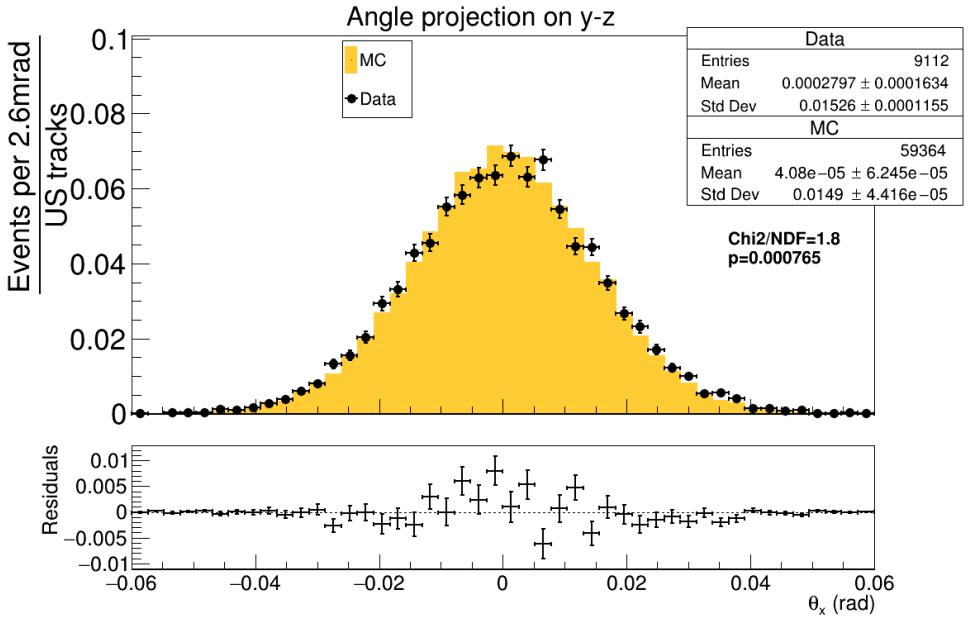

Figure 5.13: θ_x scattering distribution of the high-p muon beam through liquid-H_2 for experimental data and MC simulation.

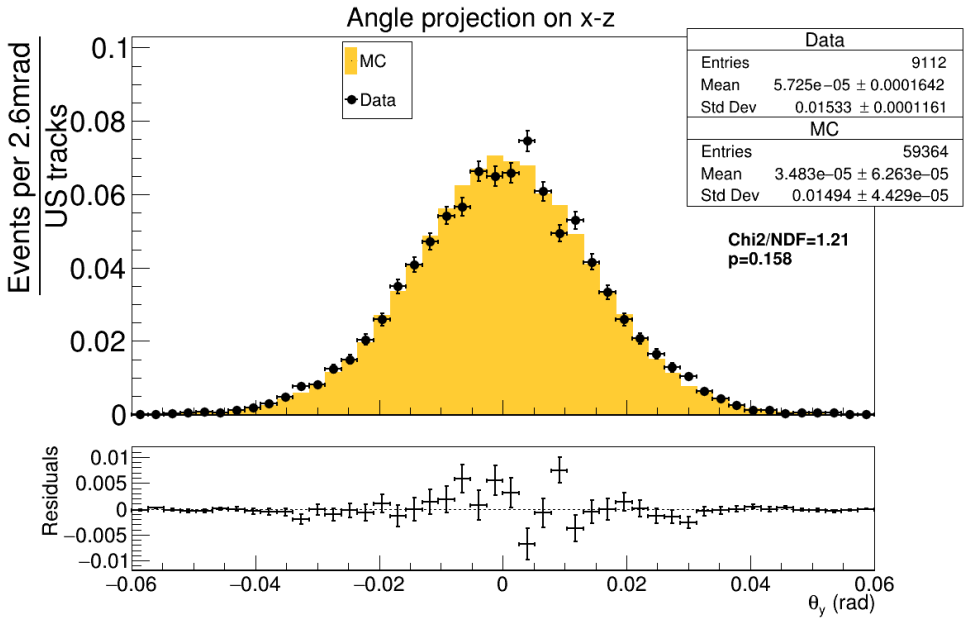

Figure 5.14: θ_y scattering distribution of the high-p muon beam through liquid-H_2 for experimental data and MC simulation.

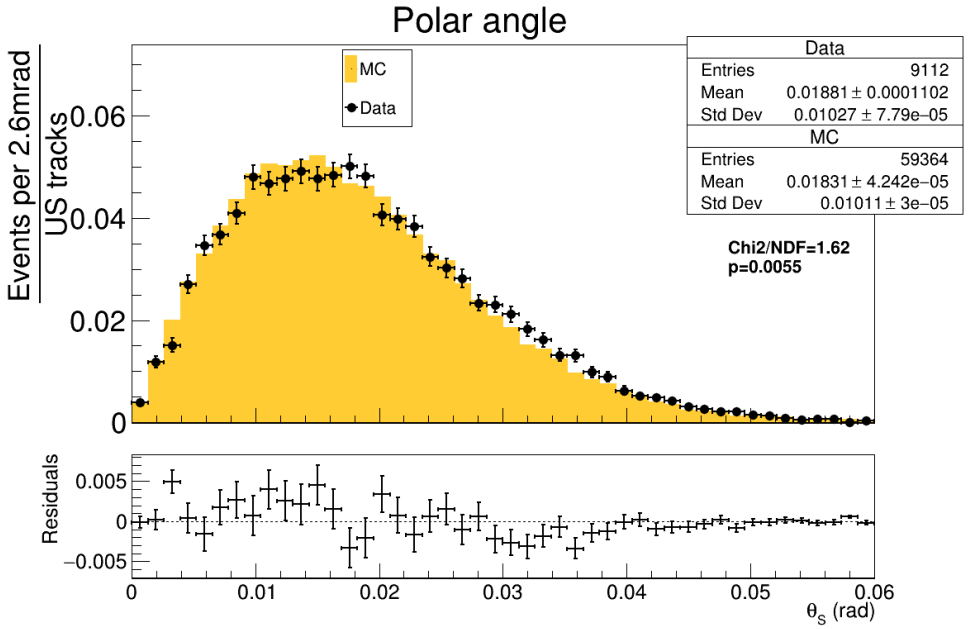

Figure 5.15: 3D scattering angle distribution of the high-p muon beam through liquid-H_2 for experimental data and MC simulation.

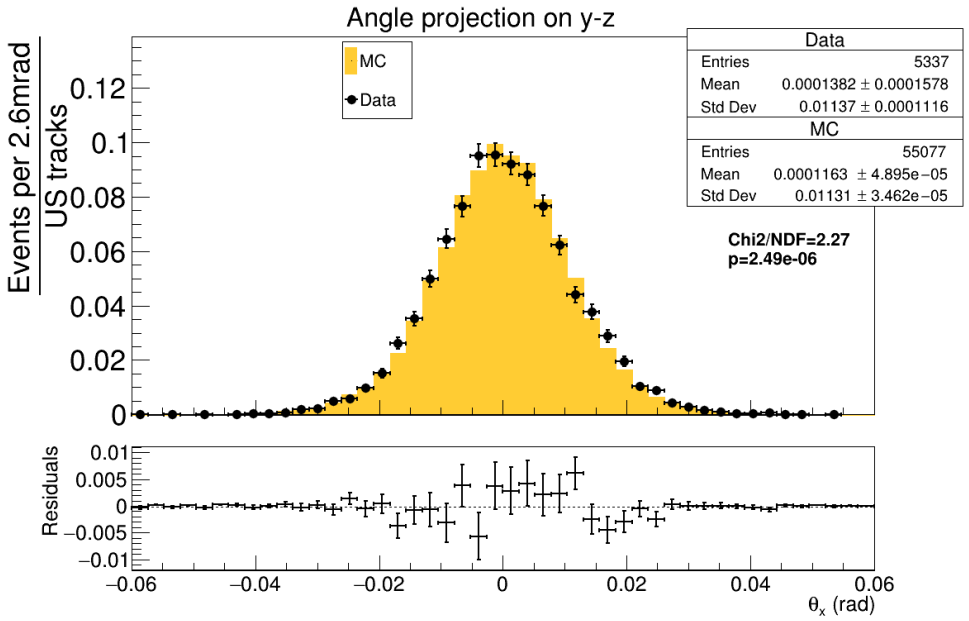

Figure 5.16: θ_x scattering distribution of the high-p muon beam through the empty vessel for experimental data and MC simulation.

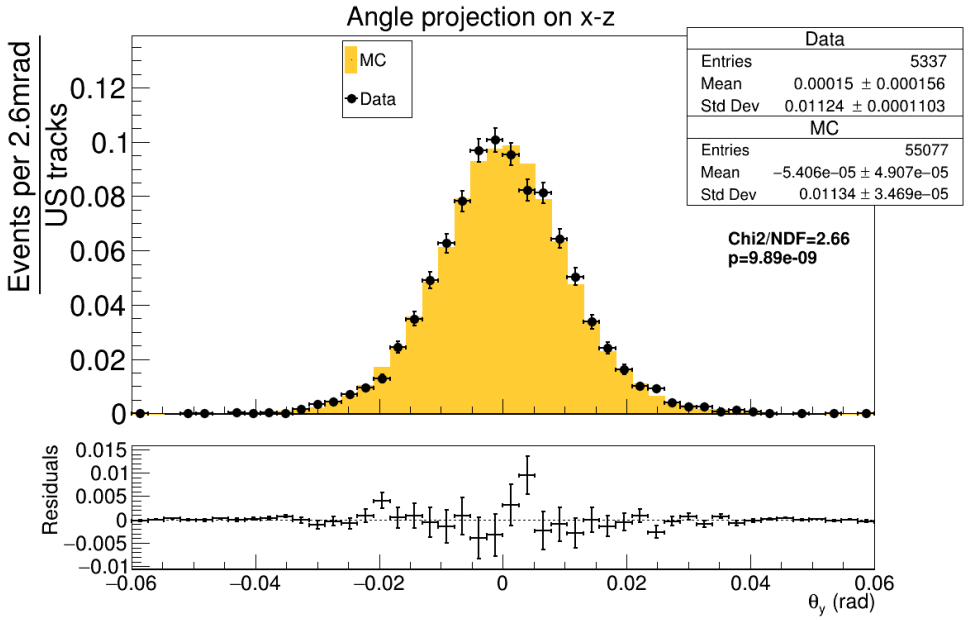

Figure 5.17: θ_y scattering distribution of the high-p muon beam through the empty vessel for experimental data and MC simulation.

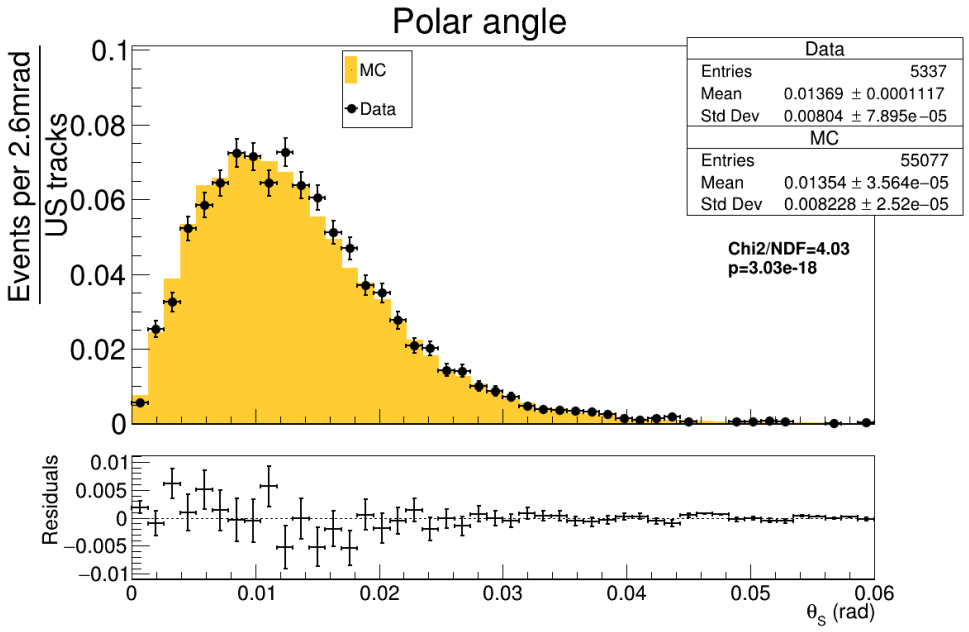

Figure 5.18: 3D scattering angle distribution of the high-p muon beam through the empty vessel for experimental data and MC simulation.

P (MeV/c), Absorber	θ_x		θ_y		θ_S	
	χ^2/NDF	p-value	χ^2/NDF	p-value	χ^2/NDF	p-value
158.3, Empty	0.625	0.977	0.592	0.987	1.2	0.167
164.9, liquid-H_2	0.526	0.996	0.641	0.971	0.435	1
191.8, Empty	0.692	0.942	0.956	0.555	1.56	0.00908
199.0, liquid-H_2	0.893	0.676	1.02	0.443	1.27	0.106
231.3, Empty	0.864	0.728	0.854	0.745	2.43	<0.001
237.1, liquid-H_2	0.919	0.627	0.698	0.938	1.1	0.298

Table 5.1: Comparison between data and MC simulation of the projected and 3D scattering angles across all beam and absorber configurations. The central muon momenta of the experimental data at the absorber are quoted corresponding to the three momentum-settings. The degrees of freedom is 45 for all distributions.

Tables 5.2 and 5.3 show the one-standard-deviation widths of the scattering angle distributions. The data are reported as σ_θ ± statistical ± systematic uncertainties and the MC as σ_θ± statistical uncertainties. As discussed in section 4.5, the width-calculation for θ_x and θ_y differ from that of θ_s. For the two plane projected-angles (θ_x and θ_y) defined respectively by equations 3.33 and 3.32, the reported widths are the σ parameters of Gaussian fits, while for θ_s the reported width is the standard deviation of the binned distribution.

Data/MC	θ_x (mrad)	θ_y (mrad)	θ_s (mrad)
164.9±7.58 MeV/c muon momentum			
Data	16.56±0.11±0.17	16.44±0.11±0.19	11.19±0.07±0.08
MC	16.15±0.04	16.21±0.04	11.15±0.03
199±8.35 MeV/c muon momentum			
Data	13.49±0.1±0.2	13.21±0.1±0.19	9.53±0.06±0.1
MC	13.16±0.03	13.19±0.03	9.66±0.02
237.1±10.1 MeV/c muon momentum			
Data	10.95±0.13±0.28	10.67±0.13±0.25	8.04±0.08±0.14
MC	10.69±0.04	10.69±0.04	8.22±0.03

Table 5.2: Scattering widths of θ_x, θ_y and θ_s for the empty-vessel experimental data and MC.

Data/MC	θ_x (mrad)	θ_y (mrad)	θ_s (mrad)
156.7±7.91 MeV/c muon momentum			
Data	22.19±0.16±0.2	22.14±0.16±0.15	13.19±0.08±0.06
MC	21.98±0.06	22.02±0.06	13.14±0.03
191.8±8.52 MeV/c muon momentum			
Data	17.89±0.12±0.16	18.14±0.12±0.13	11.63±0.07±0.05
MC	18.05±0.04	18.04±0.04	11.75±0.03
231.3±10.4 MeV/c muon momentum			
Data	15.11±0.12±0.18	15.11±0.13±0.29	10.27±0.08±0.12
MC	14.7±0.05	14.75±0.05	10.1±0.03

Table 5.3: Scattering widths of θ_x, θ_y and θ_s for the experimental and simulated full absorber configuration.

5.2 Fit to Gaussian approximation of MCS

Figures 5.19 and 5.20 show the scattering widths of θ_x and θ_y as a function of momentum. The values are fitted to expression

$$\sigma_\theta = \frac{13.6\,\mathrm{MeV/c}}{\beta p} a, \tag{5.1}$$

motivated by equation 3.28 with a free parameter a. The aim is to compare the resulting values of a between experimental data and MC simulation, for each of the two absorber configurations. There is no stylistic distinction of the absorber empty and full data-points and fitted expressions due to the clear vertical separation, as a result of the different radiation lengths in each case.

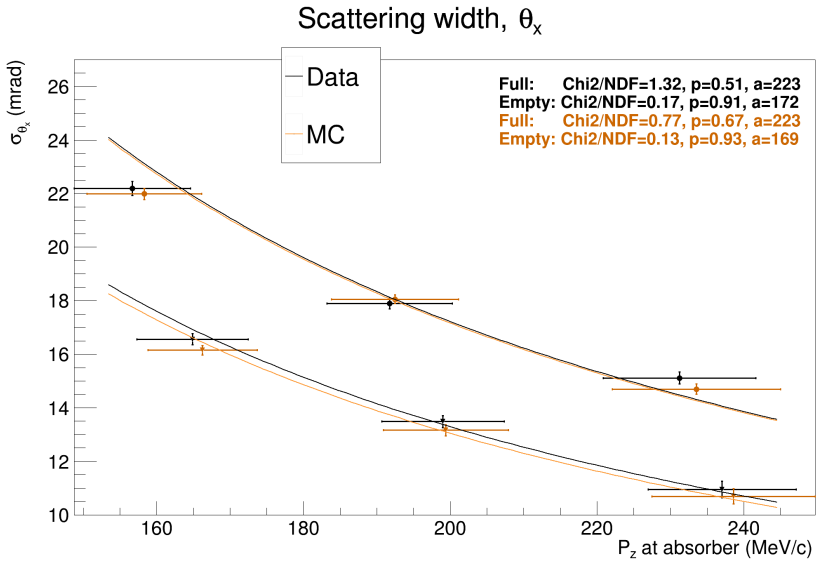

Figure 5.19: σ-width of projected angle θ_x fitted to expression 5.1.

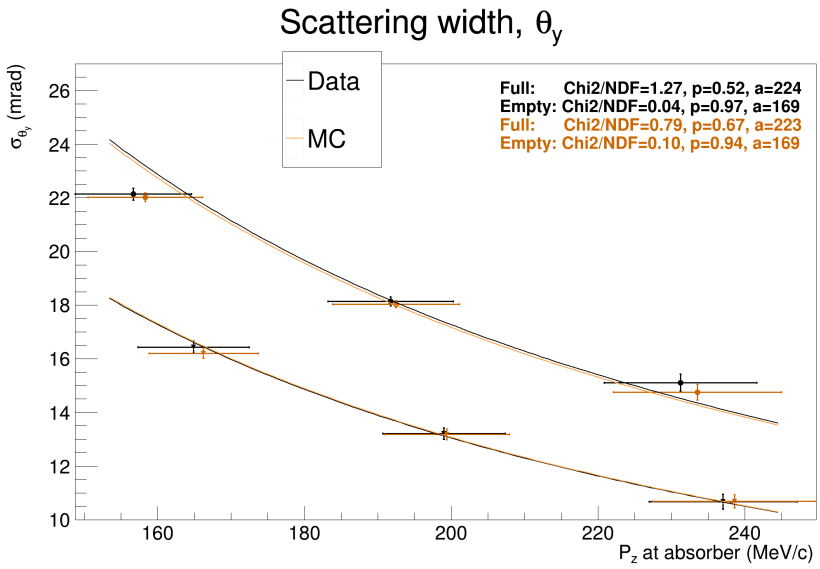

Figure 5.20: σ-width of projected angle θ_y fitted to expression 5.1.

5.3 Discussion

The measured projected angle distributions all have a mean that is within a bin-width (2.6 mrad) of zero, which is a result of the relative tracker-alignment correction described in section 4.3. The mean of the MC distributions are statistically consistent with zero without requiring this process. Additionally, the distributions of θ_x and θ_y do not show any meaningful differences with each other, hence the isotropy of MCS is observed.

The effect of liquid-H_2 is the most evident difference between the empty and full-absorber configurations when comparing same-momenta beam-settings. The observed width increase is more prominent in the shoulders of the distributions, rather than at the tails, due to the low atomic number of liquid-H_2 that contributes few large-angle deflections (nuclear scattering).

Visually, the distributions of scattering angles (figures 5.1-5.18) show a varying degree of compatibility between simulation and experiment. While the number of bins that disagree by more than a standard deviation are generally few compared

to what is expected from a finite-sampled random process, there are bin residuals that are over one standard-deviation. This can be clearly seen in the normalised residuals below each histogram. However, there is no evident trend similar to the one observed in figure 1.5, where the tails diverge progressively. The diverging bins of this analysis are fluctuations. The probability that the compared distributions are sub-samples of the same underlying probability density function is reflected by the embedded p-values. In the low momentum case (figures 5.1-5.5) and high momentum, full-absorber configuration (figure 5.14) the p-values are >0.05 while for the remaining distributions the statistic is quite low, likely due to these large fluctuations. It is important to note that these observations are made prior to including the systematic uncertainties.

The MC and experimental distributions compare well when the systematic uncertainties are included with the exception of the solid angle distributions (θ_S) for the mid and high momentum empty-absorber cases. These observations are reflected in the χ^2/NDF and p-value statistics of table 5.1. These are likely due to two reasons: limited data for the high-momentum beam and due to the definition of the solid angle. The solid angle measurement does not take place within a projected plane, therefore the measurement is affected by the uncertainties negated with the projected angle method discussed in section 3.7. The uncertainty due to the arbitrary plane-projection ($\widehat{y}$-rotation discussed in section 4.5) is accounted for in the χ^2/NDF and p-value of table 5.1 for the θ_x and θ_y distributions while it is naturally ignored in the case of θ_s since it is simply the dot product of the upstream and downstream momentum vectors. This is evident in tables 4.7 and 4.8 where the effect of the $\widehat{y}$-rotation leaves the scattering width unaffected.

The angle distribution's one-standard-deviation widths of the empty and full-absorber configurations are compared in tables 5.2 and 5.3 respectively where no meaningful difference is observed in terms of the data/simulation compatibility between the two configurations. Most values are within the 68%-uncertainty; the

remainder show random differences, without a systematic over or under-estimation.

The muon scattering experiment of the MuScat collaboration covered a solid angle twice as large as that of the present analysis, with mean muon momentum (172 ± 2 MeV/c) that although is not directly available for comparison, it is within the present analysis' range. In figure 1.5, the Geant4 (v7.0p1) simulation and the unfolded-data are evidently divergent at solid angles that are sufficiently covered in this analysis hence a comparison with the MICE results (section 5.1), using Geant4 (v9.6), can be made. The MICE simulation shows good agreement with the scattering data on liquid-H_2, without sings of divergence, therefore validating the MCS models that have been included in this more recent version of Geant4.

The width of the distributions are observed to decrease with increasing momentum in both absorber configurations in the scattering angle distributions of section 5.1. This relationship is compared between the experimental data and MC simulation using an expression motivated by 3.28 in the figures of section 5.2, where the fitted expressions for the MC and experimental data show close proximity in both projection planes. The free parameter a differs by 1.7% between data and MC simulation in the absorber-empty configuration of θ_x while it is identical for the full-absorber configuration. Considering θ_y, the fitted expressions to the data and simulation for the empty-absorber configuration have identical free parameters and a 0.4% difference in the full-absorber case. Overall, the scattering-width appears to scale with momentum in a compatible manner between the MCS algorithm of Geant4 and the experimental data in the analysed momentum range.

MICE has recently published the MCS measurement results of muons through a 65 mm LiH disk [88] in a compatible momentum range and projected angle definitions that are consistent with the present analysis. An assessment of the cooling performance of LiH is also included in the cooling demonstration, discussed in section 2.3. Although LiH has a 26% shorter radiation length than liquid-H_2, it does not require a high-Z container. This results in similar scattering widths

across the liquid-H_2 inside the aluminium vessel compared to the LiH disk. This is evident when comparing the projected angle widths of Table-V of [88] for three beam-settings that deliver muon momenta at the absorber within 10% of those in the present analysis and with the values of table 5.3. The highest momentum-setting used in [88] delivers 239.7 MeV/c mean muon momentum at the centre of the LiH disk; in this analysis that is 231.3 MeV/c while the resulting scattering widths of θ_x are 15.03 mrad (LiH) and 15.11 mrad (liquid-H_2). In terms of cooling performance, the difference of the two absorbers are minimal, as can be seen when comparing the second row of amplitude distributions in figure 2.11 (liquid-H_2) and the final row (LiH).

Chapter 6

Conclusion

Data from tens of millions of muons have been gathered by the MICE collaboration specifically to measure MCS through candidate IC absorber materials. In this thesis, reconstructed straight-track data (without operational cooling channel magnets) have been used to assess the performance of the Geant4 "WentzelVI" MCS algorithm through 22 l of liquid-H_2, maintained at a temperature of 20 K and 1.0013 bar pressure. The material is theoretically the most promising absorber candidate for IC. Approximately half the MCS data were gathered with identical beamline-settings but with an evacuated absorber vessel, to be used as a control sample. The analysis covers a momentum range in which IC is expected to be most efficient; between 140 and 250 MeV/c with three separate data-sets that delivered 157.6±7.9, 191.8±8.5 and 233.5±11.4 MeV/c at the centre of the full absorber and 164.9±7.5, 199±8.3 and 237.1± MeV/c at the evacuated absorber. Geant4 (v9.6) coupled with MAUS (v3.3.2) was used to simulate the passage of particles through a geometry defined by the MICE collaboration to closely match the MICE lattice.

The study measured the plane-projected scattering angle distributions with combined uncertainty to the one-standard-deviation width in the order of 1%. The compatibility between the Geant4 simulation and the experimental measurements

was assessed at three levels; all pertaining to the scattering angle distributions. After selection, a bin-by-bin comparison of the θ_x, θ_y and θ_s scattering angle distributions was made in terms of the residuals between normalised MC and experimental data bin contents below each distribution. The randomness of the normalised bin residuals was assessed using the p-value and χ^2/NDF metrics. Secondly, the one-standard-deviation widths of these distributions were assessed for divergences between MC/Data appearing when 33 cm of liquid-H_2 was present in the beam path. Additionally, the momentum dependence of the width of these distributions to the muon momentum was assessed with a Gaussian approximation of MCS.

The motivation behind this study is due to the role of MCS in IC and the motivation behind IC is the evident intent of the research community to further use muon beams in accelerator facilities such as a muon collider and a neutrino factory; all requiring high-brightness muon beams, which cannot be achieved with conventional beam cooling techniques. For these reasons, coupled with experimental evidence by the MuScat collaboration that older versions of Geant4 and models such as that of Molière overestimated the effect for low-Z materials made it important to ensure that the currently used Geant4 "WentzelVI" MCS algorithm can be used with confidence in the design of muon accelerator facilities.

The principal conclusion of this analysis of the MICE data is that Geant4 (v9.6) using the "QGSP_BERT" physics list, shows no discernable incompatibility with the experimental measurements (in terms of MCS) when simulating the passage of muons with 143–250 MeV/c momenta through liquid-H_2.

The overestimation of muon scattering through liquid hydrogen at large angles by Geant4 (v7.0p1), discussed in section 1.3, is not evident in this analysis that used Geant4 (v9.6). There are multiple possible reasons for this, for which a deterministic investigation was outside the scope of this analysis. The divergence was likely due to differences in the simulation models used by the two versions.

Older versions of Geant4, possibly including v7.0p1, used the Urban model [90] to simulate MCS while recent versions employ the most up-to-date Wentzel-VI model.

Regarding the MICE experiment, a secondary observation can be made in regards to the material candidates of IC. Although liquid-H_2 itself can result in low equilibrium emittance with IC, its nature makes it challenging to avoid negating this advantage with the use of high-Z containers. Liquid-H_2 requires energy-consuming cooling, and a multitude of safety measures since, the combination with oxygen is explosive (the basis of rocket-fuel). The MICE vessel has in total four intricately-designed aluminium windows that put approximately 0.78 mm of the material in the beam path. The purpose of the design was to minimise this length. The implication is that, unless a different containment solution is engineered, LiH might be a more efficient choice of material.

The MICE MCS data could be further used to assess mathematical models of MCS in methods that have already been demonstrated in the LiH study [88]. The distribution of angles seen in the figures of section 5.1 contain the effects of scattering from the scintillating-fibres, aluminium and helium of the trackers, the vessel and the atmospheric air-mixture. Additionally, the measured distributions are further inflated by the tracker's resolution. For this reason, a direct comparison of the experimental measurements of MCS through liquid-H_2 with theoretical predictions other than that of Geant4 is not attempted in this thesis. Mathematical models, such as that of Molière are used to calculate the p.d.f of the angular deflection of a beam, without analytic propagations of individual particle tracks through a material. The convolution of the resultant function with the empty-vessel data-set can be used to assess the accuracy of such models, by examining if the full-absorber angle distribution is accurately recovered. Conversely, the empty-absorber distribution can be deconvolved from the full-absorber, which would lead to an experimentally measured distribution of angles that is solely a

result of scattering through the absorber material.

In appendix A, the experimentally measured trace-space coordinates of the selected particles at the last station of the upstream tracker (left column) for the empty vessel configurations (figure-block A.1) and full vessel (figure-block A.3) are shown next to the same parameters at the upstream-most station of the downstream tracker (right column). The same parameters are plotted in appendix B for the simulation.

Appendix A

Data, trace-space distributions

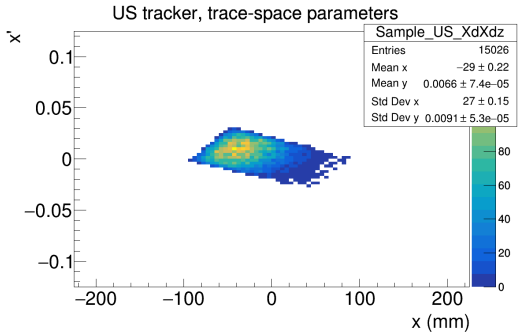

(a) Upstream - Absorber Empty, low-p beam

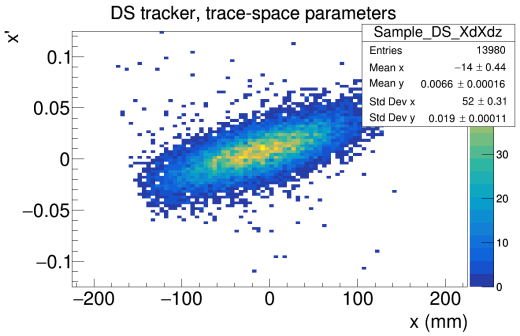

(b) Downstream - Absorber Empty, low-p beam

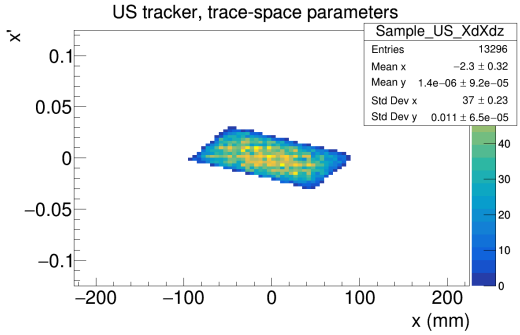

(c) Upstream - Absorber Empty, mid-p beam

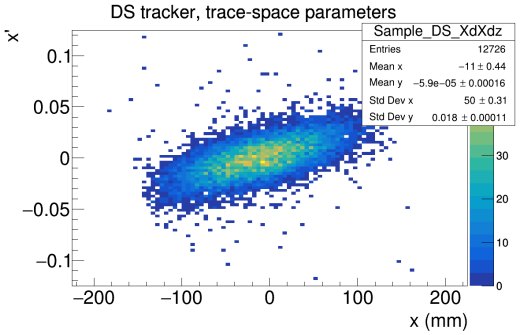

(d) Downstream - Absorber Empty, mid-p beam

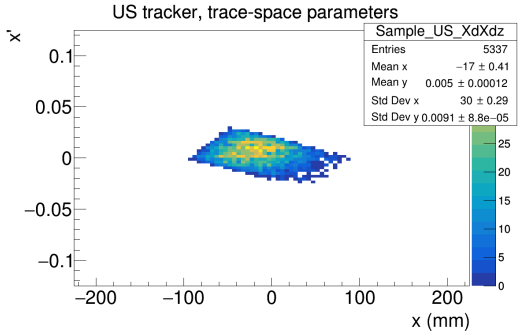

(e) Upstream - Absorber Empty, high-p beam

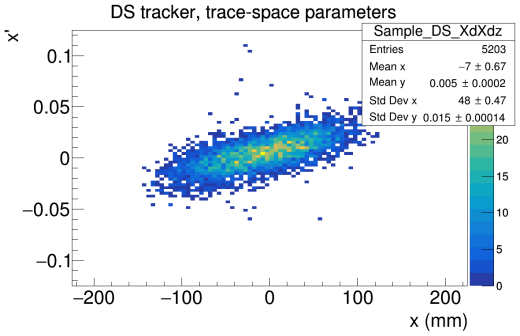

(f) Downstream - Absorber Empty, high-p beam

Figure A.1: x-x' trace-space distributions from the scintillating-fibre trackers from the experimental measurement with the empty vessel. The left column illustrates data from the upstream tracker and the right column for the downstream tracker.

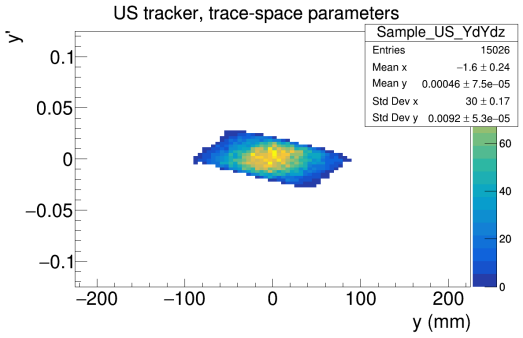

(a) Upstream - Absorber Empty, low-p beam

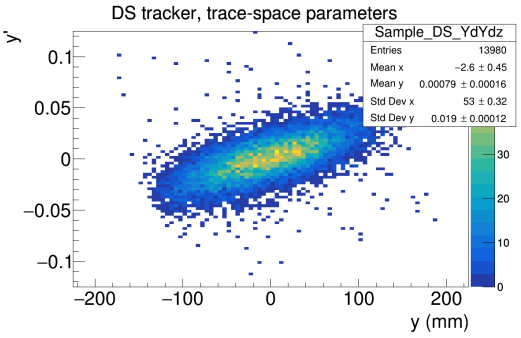

(b) Downstream - Absorber Empty, low-p beam

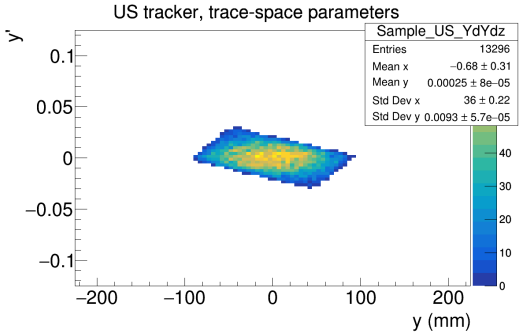

(c) Upstream - Absorber Empty, mid-p beam

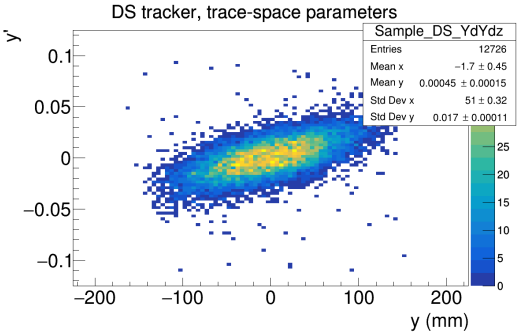

(d) Downstream - Absorber Empty, mid-p beam

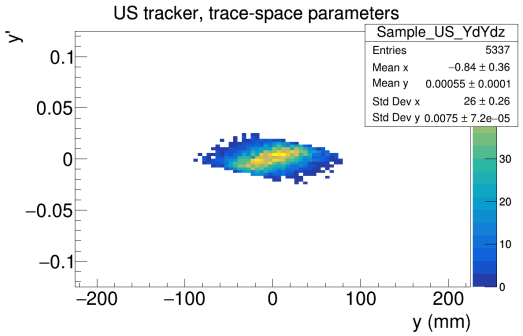

(e) Upstream - Absorber Empty, high-p beam

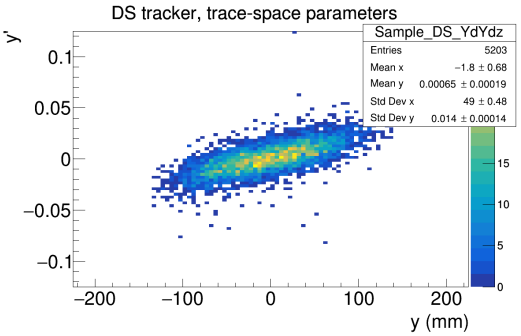

(f) Downstream - Absorber Empty, high-p beam

Figure A.2: y-y' trace-space distributions from the scintillating-fibre trackers from the experimental measurement with the empty vessel. The left column illustrates data from the upstream tracker and the right column for the downstream tracker.

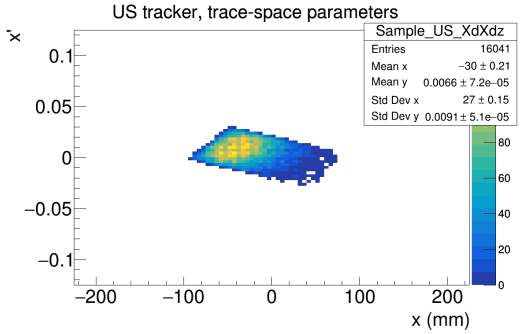

(a) Upstream - liquid-H_2, low-p beam

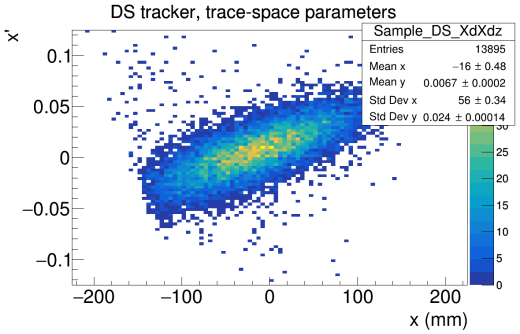

(b) Downstream - liquid-H_2, low-p beam

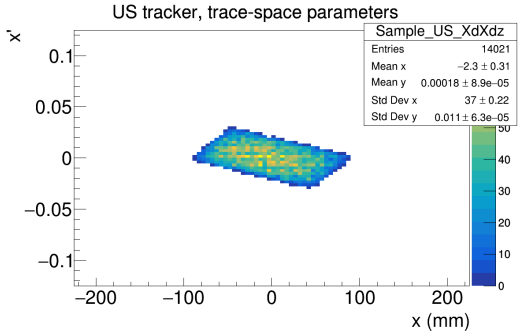

(c) Upstream - liquid-H_2, mid-p beam

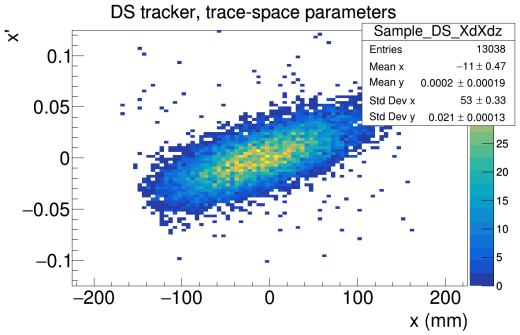

(d) Downstream - liquid-H_2, mid-p beam

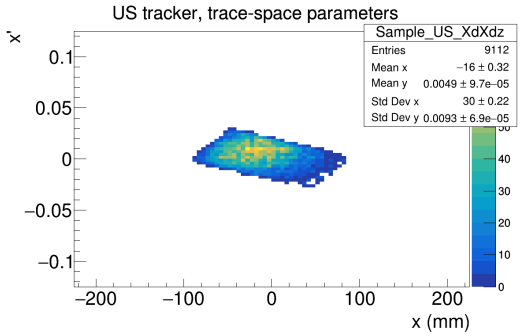

(e) Upstream - liquid-H_2, high-p beam

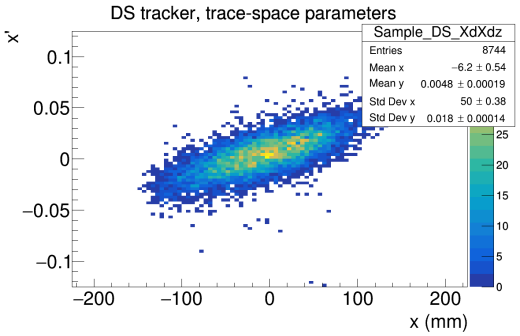

(f) Downstream - liquid-H_2, high-p beam

Figure A.3: x-x' trace-space distributions from the scintillating-fibre trackers from the experimental measurement with liquid-H_2. The left column illustrates data from the upstream tracker and the right column for the downstream tracker.

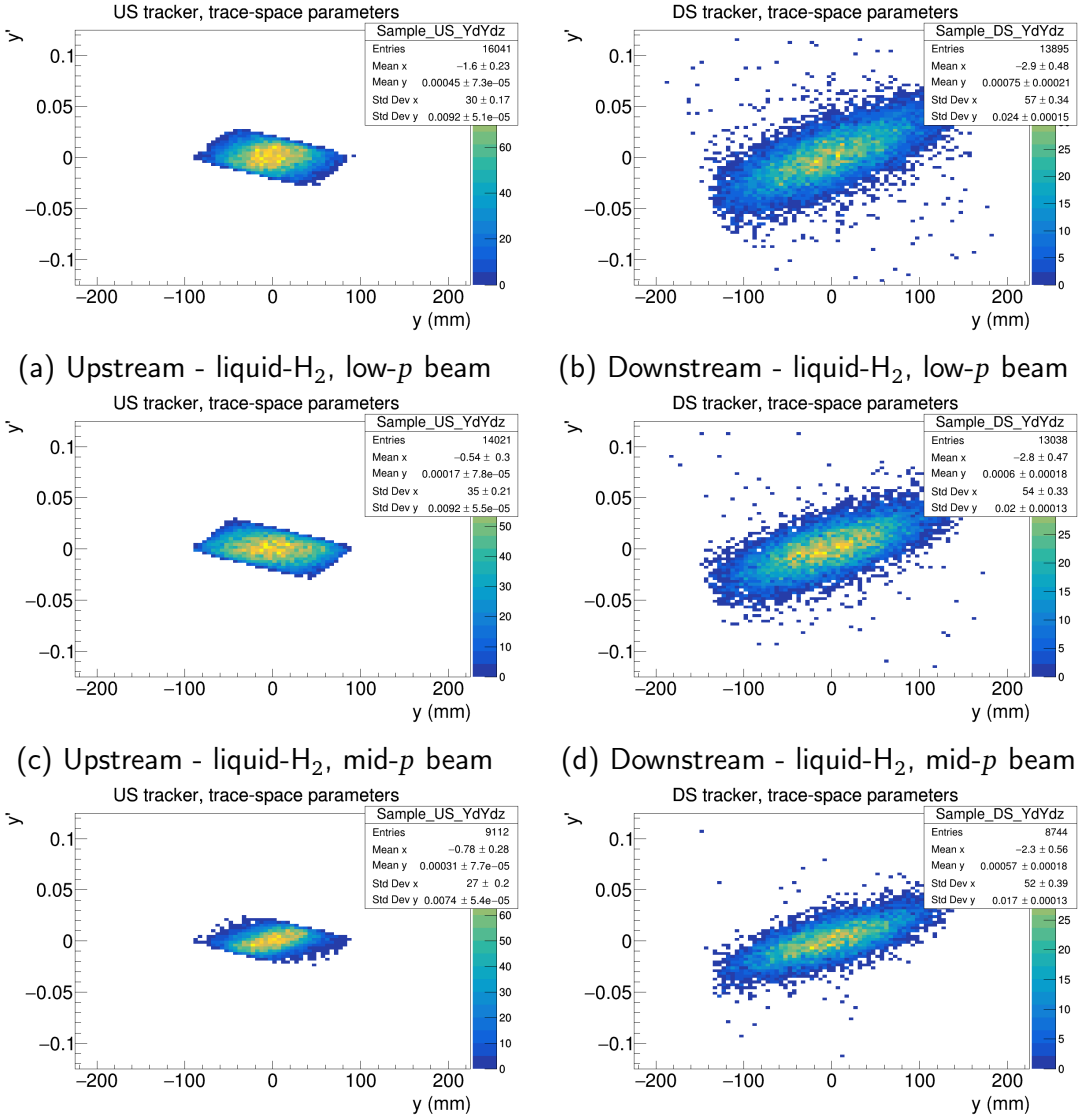

(a) Upstream - liquid-H_2, low-p beam

(b) Downstream - liquid-H_2, low-p beam

(c) Upstream - liquid-H_2, mid-p beam

(d) Downstream - liquid-H_2, mid-p beam

(e) Upstream - liquid-H_2, high-p beam

(f) Downstream - liquid-H_2, high-p beam

Figure A.4: y-y' trace-space distributions from the scintillating-fibre trackers from the experimental measurement with liquid-H_2. The left column illustrates data from the upstream tracker and the right column for the downstream tracker.

Appendix B

MC, trace-space distributions

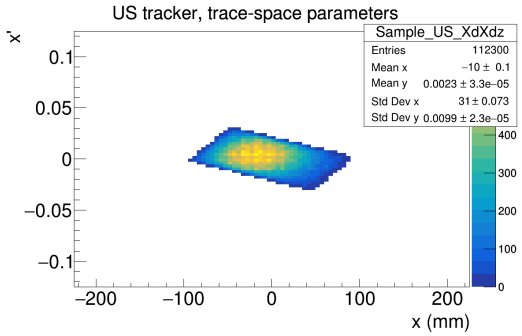

(a) Upstream - Absorber Empty, low-p beam

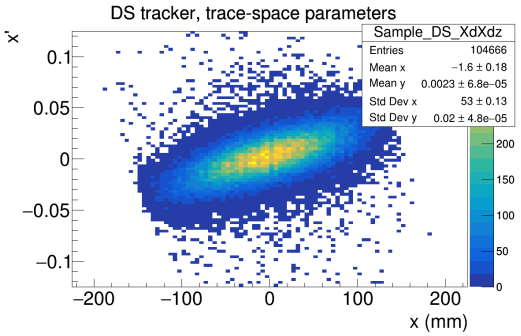

(b) Downstream - Absorber Empty, low-p beam

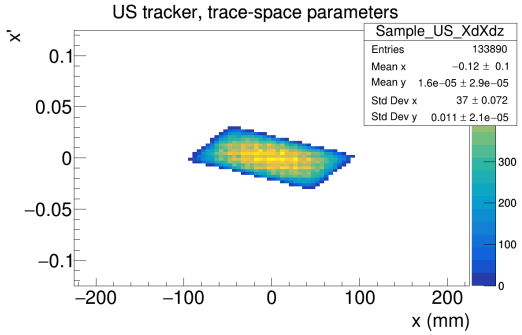

(c) Upstream - Absorber Empty, mid-p beam

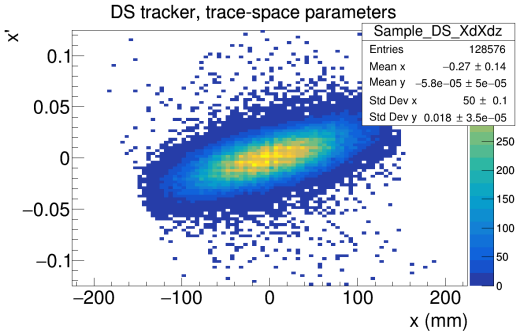

(d) Downstream - Absorber Empty, mid-p beam

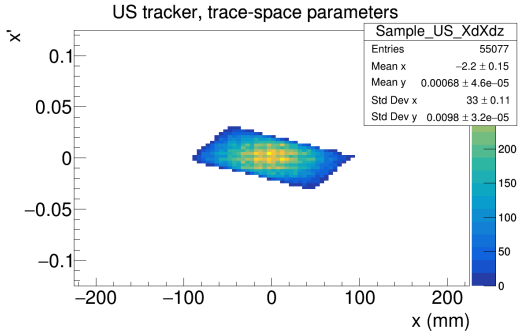

(e) Upstream - Absorber Empty, high-p beam

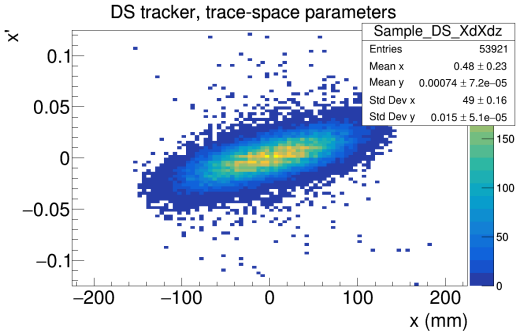

(f) Downstream - Absorber Empty, high-p beam

Figure B.1: x-x' trace-space distributions from the scintillating-fibre trackers from the Geant4 MC simulation with the empty vessel. The left column illustrates data from the upstream tracker and the right column for the downstream tracker.

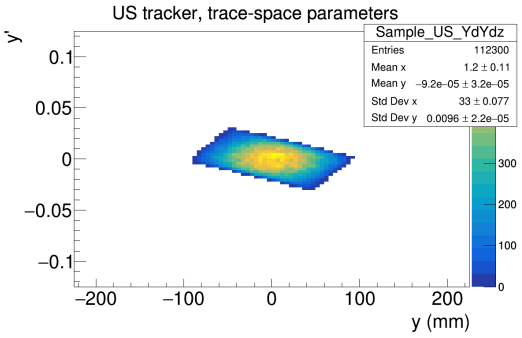

(a) Upstream - Absorber Empty, low-p beam

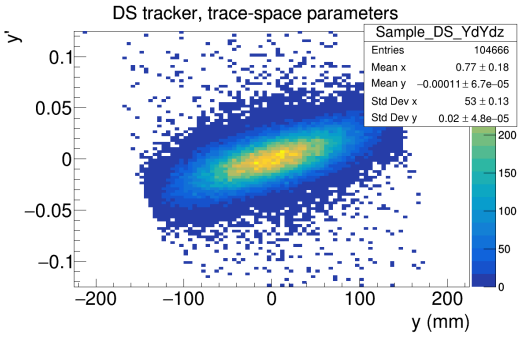

(b) Downstream - Absorber Empty, low-p beam

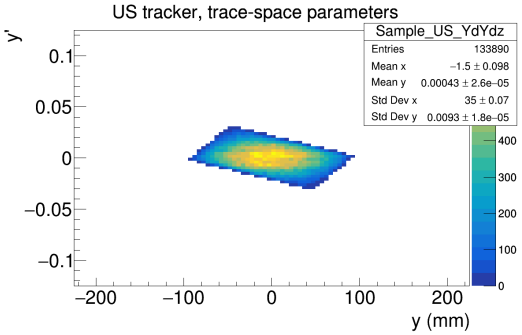

(c) Upstream - Absorber Empty, mid-p beam

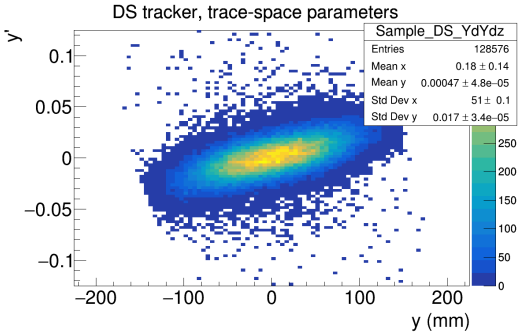

(d) Downstream - Absorber Empty, mid-p beam

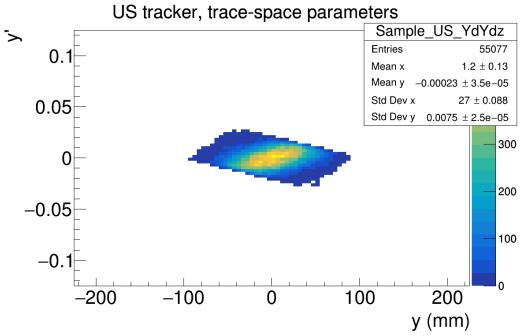

(e) Upstream - Absorber Empty, high-p beam

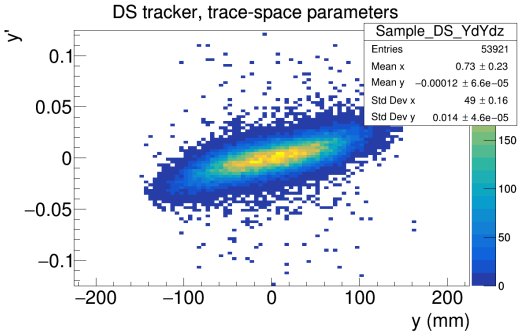

(f) Downstream - Absorber Empty, high-p beam

Figure B.2: y-y' trace-space distributions from the scintillating-fibre trackers from the Geant4 MC simulation with the empty vessel. The left column illustrates data from the upstream tracker and the right column for the downstream tracker.

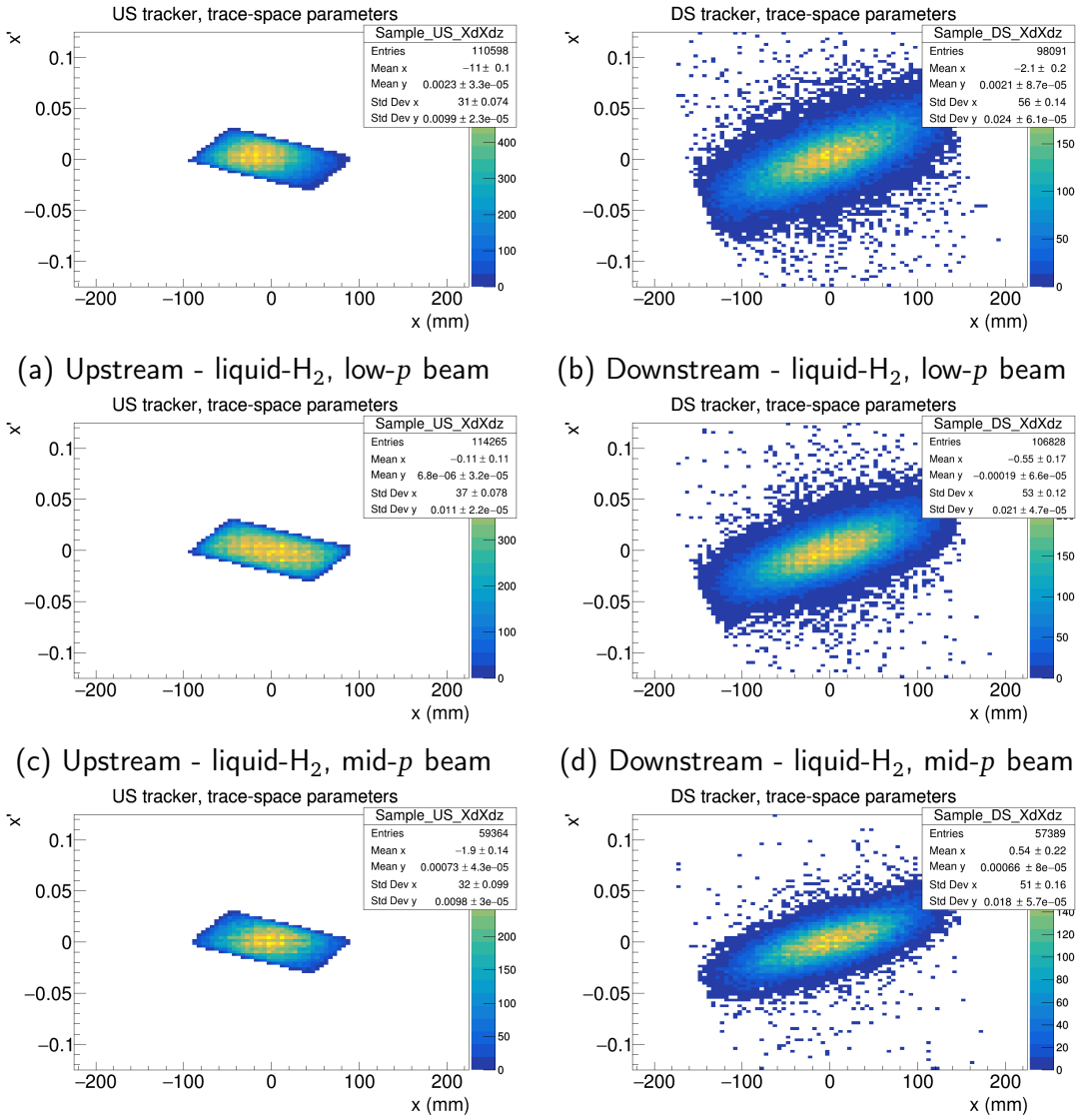

(a) Upstream - liquid-H_2, low-p beam

(b) Downstream - liquid-H_2, low-p beam

(c) Upstream - liquid-H_2, mid-p beam

(d) Downstream - liquid-H_2, mid-p beam

(e) Upstream - liquid-H_2, high-p beam

(f) Downstream - liquid-H_2, high-p beam

Figure B.3: x-x' trace-space distributions from the scintillating-fibre trackers from the Geant4 MC simulation with liquid-H_2. The left column illustrates data from the upstream tracker and the right column for the downstream tracker.

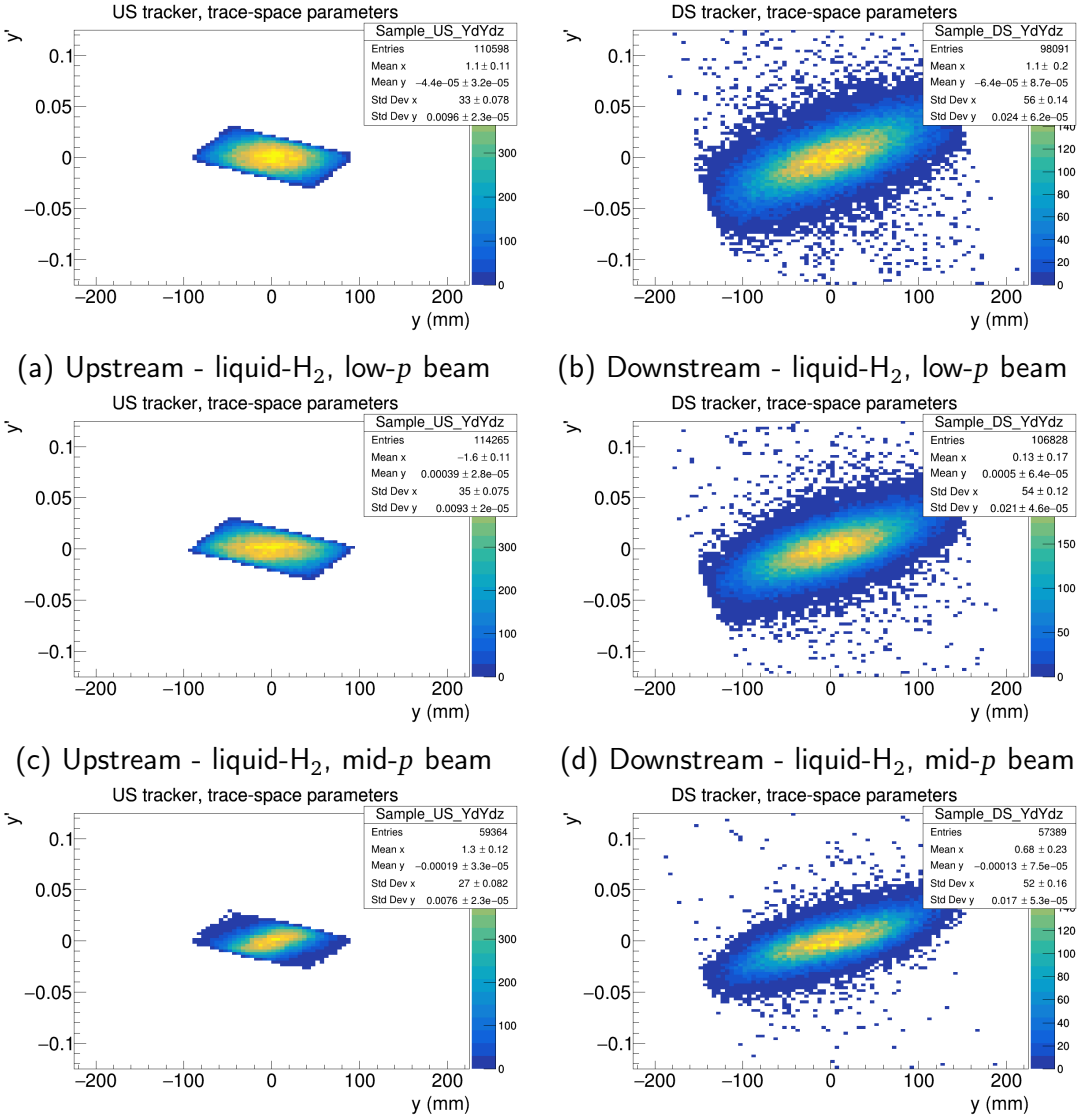

(a) Upstream - liquid-H_2, low-p beam

(b) Downstream - liquid-H_2, low-p beam

(c) Upstream - liquid-H_2, mid-p beam

(d) Downstream - liquid-H_2, mid-p beam

(e) Upstream - liquid-H_2, high-p beam

(f) Downstream - liquid-H_2, high-p beam

Figure B.4: y-y' trace-space distributions from the scintillating-fibre trackers from the Geant4 MC simulation with liquid-H_2. The left column illustrates data from the upstream tracker and the right column for the downstream tracker.

Bibliography

[1] M. K. Gaillard *et al.*, "The standard model of particle physics", *Rev. Mod. Phys.*, vol. 71, pp. S96–S111, Mar. 1999. doi:10.1103/RevModPhys.71.S96.

[2] P. Peebles, "Large-scale background temperature and mass fluctuations due to scale-invariant primeval perturbations", *APJL*, vol. 263, pp. L1–L5, Dec. 1982. doi:10.1086/183911.

[3] L. Bergström, "Dark matter candidates", *New J. Phys.*, vol. 11, p. 105006, Oct. 2009. doi:10.1088/1367-2630/11/10/105006.

[4] H. Nunokawa *et al.*, "CP–violation and neutrino oscillations", *Prog. Part. Nucl. Phys.*, vol. 60, pp. 338–402, Apr. 2008. doi:10.1016/j.ppnp.2007.10.001.

[5] J. H. Christenson *et al.*, "Evidence for the 2π Decay of the K20 Meson", *PRL*, vol. 13, pp. 138–140, July 1964. 10.1103/PhysRevLett.13.138.

[6] R. Aaij *et al.*, "First observation of CP–violation in the decays of B_s^0 mesons", *Phys. Rev. Let.*, vol. 110, May. 2013. doi:10.1103/physrevlett.110.221601.

[7] A. Höcker and Z. Ligeti, "CP-violation and the CKM matrix", *Annu. Rev. Nucl. Part. Sci.*, vol. 56, pp. 501–567, 2006.

[8] K. Abe *et al.*, "Constraint on the matter–antimatter symmetry–violating phase in neutrino oscillations", *Nature*, vol. 580, pp. 339–344, Apr. 2020. doi:10.1038/s41586-020-2177-0.

[9] W. Rodejohann and X.-J. Xu, "Origin of symmetric PMNS and CKM matrices", *Phys. Rev. D*, vol. 91, p. 056004, Mar. 2015. doi:10.1103/PhysRevD.91.056004.

[10] A. De Rujula *et al.*, "Neutrino oscillation physics with a neutrino factory", *Nucl. Phys. B*, vol. 547, pp. 21 – 38, 1999. doi:10.48550/arXiv.hep-ph/9811390.

[11] G. Hesketh *et al.*, "The Mu3e Experiment", Apr. 2022. arXiv:2204.00001.

[12] L. Bartoszek *et al.*, "Mu2e technical design report", Mar. 2015. arxiv:1501.05241.

[13] Abramishvili, R. et al., COMET Collaboration, "COMET Phase-I Technical Design Report", *PTEP*, no. 3, p. 033C01, 2020. doi:10.1093/ptep/ptz125.

[14] Abi, B. et al., Muon g-2 Collaboration, "Measurement of the Positive Muon Anomalous Magnetic Moment to 0.46 ppm", *Phys. Rev. Lett.*, vol. 126, p. 141801, Apr. 2021. doi:10.1103/PhysRevLett.126.141801.

[15] M. Bogomilov *et al.*, "Neutrino Factory", *Phys. Rev. ST Accel. Beams*, vol. 17, p. 121002, May 2014. 10.1103/PhysRevSTAB.17.121002.

[16] K. Long *et al.*, "Muon colliders to expand frontiers of particle physics", *Nature Phys.*, vol. 17, no. 3, pp. 289–292, 2021. doi:10.1038/s41567-020-01130-x.

[17] J. D. Lawson *et al.*, "Emittance, entropy and information", *Part. Accel.*, vol. 5, pp. 61–65, 1973.

[18] E. B. Levichev *et al.*, "Low emittance electron storage rings", *Phys. Usp.*, vol. 61, no. 1, pp. 29–51, 2018. doi:10.3367/UFNe.2016.12.038014.

[19] E. Wilson, *An Introduction to Particle Accelerators*. Oxford University Press, 2001. ISBN:9780198508298.

[20] M. Bieler *et al.*, "Status of the Petra–III upgrade", in *IPAC'12*, pp. 1620–1622, Jan. 2012. TUPPP009.

[21] M. Tischer *et al.*, "Damping Wigglers for the Petra–III Light Source", in *PAC'05*, pp. 2446 – 2448, June 2005. doi:10.1109/PAC.2005.1591140.

[22] G. Tranquille, "40 Years of Electron Cooling at CERN", in *IPAC'18*, pp. 69–72, June 2018. doi:10.18429/JACoW-IPAC2018-MOZGBF3.

[23] S. van der Meer, "Stochastic damping of betatron oscillations in the ISR", pp. 261–269, Aug. 1972. CERN-ISR-PO-72-31.

[24] G. Budker, "An effective method of damping particle oscillations in proton and antiproton storage rings", *Sov. At. Energy*, vol. 22, pp. 438–440, Dec. 1967.

[25] V. V. Parkhomchuk and N. A. Skrinski, "Electron cooling: 35 years of development", *Physics-Uspekhi*, vol. 43, pp. 433–452, May 2000. doi:10.1070/pu2000v043n05abeh000741.

[26] S. van der Meer, "Stochastic cooling and the accumulation of antiprotons". https://www.nobelprize.org/uploads/2018/06/meer-lecture.pdf.

[27] D. Mohl, "Stochastic Cooling for Beginners", *Conf. Proc. C*, vol. 831011, pp. 97–161, 1983.

[28] Y. M. Ado and V. I. Balbekov, "Use of ionization friction in the storage of heavy particles", *Sov. Atom. Energ.*, vol. 31, pp. 731–736, 1971. doi:10.1007/BF01123390.

[29] D. Neuffer, "Principles and Applications of Muon Cooling", *Part. Accel.*, vol. 14, pp. 75–90, 1983.

[30] S. Eidelman *et al.*, "Review of Particle Physics", *Physics Letters B*, vol. 592, no. 1, pp. 1–5, 2004. doi:10.1016/j.physletb.2004.06.001.

[31] MICE Collaboration, "MICE Data". `http://gfe02.grid.hep.ph.ic.ac.uk:8301/RECO/MAUS-v3.3.2/1/Step4/`.

[32] Tanabashi, M. et al., Particle Data Group, "Review of Particle Physics", *Phys. Rev. D*, vol. 98, pp. 030001–31899, 2018. doi:10.1103/PhysRevD.98.030001.

[33] D. Kaplan, "MANX: A 6D ionization-cooling experiment", vol. 981, Dec. 2007. doi:10.1063/1.2898966.

[34] Brown, C., MICE Collaboration, "Monte Carlo simulation of reverse emittance exchange in MICE", *PoS*, p. 707, 2021. doi:10.22323/1.390.0707.

[35] D. Attwood et al., MuScat Collaboration, "The scattering of muons in low Z materials", *Nucl. Instrum. Meth. Sec. A*, vol. 83, pp. 492–504, 2005. doi:10.1016/j.nimb.2006.05.006.

[36] H. A. Bethe, "Molière's Theory of Multiple Scattering", *Phys. Rev.*, vol. 89, pp. 1256–1266, Mar. 1953. doi:10.1103/PhysRev.89.1256.

[37] W. Allison, "Calculations of energy loss and multiple scattering (ELMS) in molecular hydrogen", *J. Phys. G: Nucl. Part.*, vol. 29, pp. 1701–1703, July 2003. 10.1088/0954-3899/29/8/334.

[38] M. Bonesini, "Progress of the MICE experiment at RAL", *Nucl. Phys. B*, vol. 237-238, pp. 203–205, 2013. doi:10.1016/j.nuclphysbps.2013.04.091.

[39] M. Bogomilov, Y. Karadzhov, *et al.*, "The MICE Muon Beam on ISIS and the beam-line instrumentation of the Muon Ionization Cooling Experiment", *J. Inst.*, vol. 7, p. 5009–5009, 2012. doi:10.1088/1748-0221/7/05/P05009.

[40] D. Adams *et al.*, "Characterisation of the muon beams for the Muon Ionisation Cooling Experiment", *EPJ C*, vol. 73, p. 2582, Oct. 2013. doi:10.1140/epjc/s10052-013-2582-8.

[41] Bogomilov, M et al., MICE Collaboration, "Demonstration of cooling by the Muon Ionization Cooling Experiment", *Nature*, vol. 578, pp. 53–59, 2020. doi:10.1038/s41586-020-1958-9.

[42] MICE Collaboration, "MICE web-page". `http://mice.iit.edu/`.

[43] R. Bertoni *et al.*, "The design and commissioning of the MICE upstream time-of-flight system", *Nucl. Instrum.*, vol. 615, no. 1, pp. 14–26, 2010. doi:10.1016/j.nima.2009.12.065.

[44] R. Bertoni *et al.*, "The construction of the MICE TOF2 detector", 2010. https://cds.cern.ch/record/1307101.

[45] Rayner, M., *"The development of a novel technique for characterizing the MICE muon beam and demonstrating its suitability for a muon cooling measurement"*. PhD thesis, 2011. University of Oxford.

[46] M. Ellis *et al.*, "The design, construction and performance of the MICE scintillating fibre trackers", *Nucl. Instrum. Meth. Sec. A*, vol. 659, p. 136–153, 2011. doi:10.1016/j.nima.2011.04.041.

[47] V. Bayliss *et al.*, "The liquid-hydrogen absorber for MICE", *J. Inst.*, vol. 13, p. 9008–9008, 2018. doi:10.1088/1748-0221/13/09/T09008.

[48] L. Cremaldi *et al.*, "A Cherenkov Radiation Detector with High Density Aerogels", *IEEE Trans. Nucl. Sci.*, vol. 56, pp. 1475–1478, 2009. doi:http://dx.doi.org/10.1109/TNS.2009.2021266.

[49] F. Ambrosino *et al.*, "Calibration and performances of the KLOE calorimeter", *Nucl. Instrum. Meth. Sec. A*, vol. 598, pp. 239–243, 2009. doi:10.1016/j.nima.2008.08.097.

[50] M. Zobov, "Status Report on DAΦNE Performance", in *Proc. Europ. Part. Acc. Conf., Wien*, p. 43, 2000. `https://cds.cern.ch/record/504752`.

[51] D. Adams *et al.*, "Electron-muon ranger: performance in the MICE muon beam", *J. Inst.*, vol. 10, pp. 12012–12012, 2015. doi:10.1088/1748-0221/10/12/P12012.

[52] MICE Collaboration, "MAUS User Guide". `http://micewww.pp.rl.ac.uk/maus/MAUS_latest_version/maus_user_guide/index.html`.

[53] A. Dobbs et al., "The reconstruction software for the mice scintillating fibre trackers", *JINST*, vol. 11, no. 12, p. T12001, 2016. doi:10.1088/1748-0221/11/12/T12001.

[54] R. E. Kalman, "A New Approach to Linear Filtering and Prediction Problems", *J. Basic Eng.*, vol. 82, pp. 35–45, 1960.

[55] R. Asfandiyarov *et al.*, "MAUS: the MICE analysis user software", *J. Inst.*, vol. 14, no. 04, p. T04005, 2019. doi:10.1088/1748-0221/14/04/T04005.

[56] S. Agostinelli *et al.*, "Geant4—a simulation toolkit", *Nucl. Instrum. Methods Phys. Res. A*, vol. 506, no. 3, pp. 250–303, 2003. doi:10.1016/S0168-9002(03)01368-8.

[57] D. Jeffrey and S. G., "MapReduce: Simplified Data Processing on Large Clusters", pp. 137–150, 2004. `https://static.googleusercontent.com/media/research.google.com/en//archive/mapreduce-osdi04.pdf`.

[58] C. N. Booth *et al.*, "The design, construction and performance of the MICE target", *J. Inst.*, vol. 8, p. P03006, 2013. doi:10.1088/1748-0221/8/03/P03006.

[59] F. Pezoa *et al.*, "Foundations of JSON schema", in *ICIWWW'16*, pp. 263–273. doi:10.1016/S0168-9002(97)00048-X.

[60] R. Brun and F. Rademakers, "ROOT: An object oriented data analysis framework", *Nucl. Instrum. Meth. Sec. A*, vol. 389, pp. 81–86, 1997.

[61] T. Roberts *et al.*, "G4beamline Particle Tracking in Matter Dominated Beam Lines", in *IPAC'11*. `https://www.osti.gov/biblio/1020748`.

[62] R. Chytracek *et al.*, "Geometry Description Markup Language for Physics Simulation and Analysis Applications", *IEEE Trans. Nucl. Sci.*, vol. 53, no. 5, pp. 2892–2896, 2006. doi:10.1109/TNS.2006.881062.

[63] P. Jurj, "Normalized Transverse Emittance Reduction via Ionization Cooling in MICE 'Flip Mode'", in *IPAC'21*, p. MOPAB134. doi:10.18429/JACoW-IPAC2021-MOPAB134.

[64] M. Apollonio *et al.*, "The MICE Diffuser System", in *EPAC'08*, pp. 2761–2763.

[65] G. Ambrosio and G. Bellomo, "Magnetic field, multipole expansion and peak field in 2D for superconducting accelerator magnets", tech. rep., INFN/TC-96/15, 1996.

[66] M. Martini, "An introduction to transverse beam dynamics in accelerators", tech. rep., CERN, Geneva, 1996.

[67] W. Hillert, "Transverse Linear Beam Dynamics", 2021. arxiv:2107.02614.

[68] Choi, J. et al., "Dipole Fringe Field Analysis of the NSLS-II Storage Ring", in *9th International Particle Accelerator Conference*, 2018. doi:10.18429/JACoW-IPAC2018-TUPMK014.

[69] Adrian Cross, University of Strathclyde, "Lecture notes - PH452: Topics in Physics".

[70] J. Pitters *et al.*, "Pepperpot emittance measurements of ion beams from an electron beam ion source", *Nucl. Instrum. Meth. A*, vol. 922, pp. 28–35, 2019. doi:10.1016/j.nima.2018.12.072.

[71] R. Bodenstein, *"A Procedure for Beamline Characterization and Tuning in Open-Ended Beamlines"*. PhD thesis, 2012. University of Virginia.

[72] Particle Data Group, "Atomic and nuclear properties". `https://pdg.lbl.gov/2022/AtomicNuclearProperties/`.

[73] R. M. Sternheimer, "The Density Effect for the Ionization Loss in Various Materials", *Phys. Rev.*, vol. 88, pp. 851–859, Nov. 1952. doi:10.1103/PhysRev.88.851.

[74] K. S. Sharada, "A Note on the Density Effect Correction for the Stopping Power Values of Electrons in Sulfur and Calcium", *Radiation Research*, vol. 97, no. 2, pp. 424–433, 1984.

[75] E. Rutherford, "The scattering of α and β particles by matter and the structure of the atom", *Lond. Edinb. Dublin philos. mag*, vol. 21, no. 125, pp. 669–688, 1911. doi:10.1080/14786440508637080.

[76] H. Geiger and E. Marsden, "On a Diffuse Reflection of the α -Particles", *Proc. R. Soc. Lond.*, vol. 82, pp. 495–500, July 1909. doi:10.1098/rspa.1909.0054.

[77] G. Wentzel, "Zwei Bemerkungen über die Zerstreuung korpuskularer Strahlen als Beugungserscheinung", *Z. Physik*, vol. 40, p. 590–593, 1926. doi:10.1007/BF01390457.

[78] J. Fernández-Varea and R. M. et al., "On the theory and simulation of multiple elastic scattering of electrons", *Nucl. Instrum. Methods Phys. Res. B*, vol. 73, no. 4, pp. 447–473, 1993.

[79] B. Rossi and K. Greisen, "Cosmic-Ray Theory", *Rev. Mod. Phys.*, vol. 13, pp. 240–309, Oct. 1941. doi:10.1103/RevModPhys.13.240.

[80] V. L. Highland, "Some practical remarks on multiple scattering", *Nuclear Instruments and Methods*, vol. 129, no. 2, pp. 497–499, 1975. doi:10.1016/0029-554X(75)90743-0.

[81] E. J. Williams, "Multiple Scattering of Fast Electrons and Alpha-Particles, and "Curvature" of Cloud Tracks Due to Scattering", *Phys. Rev.*, vol. 58, pp. 292–306, 1940. doi:10.1103/PhysRev.58.292.

[82] S. Goudsmit and J. L. Saunderson, "Multiple Scattering of Electrons", *Phys. Rev.*, vol. 57, pp. 24–29, Jan. 1940. doi:10.1103/PhysRev.57.24.

[83] H. W. Lewis, "Multiple Scattering in an Infinite Medium", *Phys. Rev.*, vol. 78, pp. 526–529, 1950. doi:10.1103/PhysRev.78.526.

[84] T. Carlisle, *Step IV of the Muon Ionization Cooling Experiment (MICE) and the multiple scattering of muons*. PhD thesis, 2013. University of Oxford.

[85] Geant4 Collaboration, "Geant4 Physics Reference Manual". `https://geant4.web.cern.ch/support/user_documentation`.

[86] "Reference Physics Lists for Geant4". `https://geant4-userdoc.web.cern.ch/UsersGuides/PhysicsReferenceManual/html/index.html`.

[87] V. N. Ivanchenko *et al.*, "Geant4 models for simulation of multiple scattering", *J. Phys. Conf. Ser.*, vol. 219, p. 032045, Apr. 2010. doi:10.1088/1742-6596/219/3/032045.

[88] M. Bogomilov *et al.*, "Multiple Coulomb Scattering of muons in Lithium Hydride", 2022. arxiv:2209.10251.

[89] N. D. Gagunashvili, "Comparison of weighted and unweighted histograms", 2006. arXiv:physics/0605123.

[90] L. Urban, "A model for multiple scattering in GEANT4", *Monte Carlo 2005 Topical Meeting*, 2005.